Inês de Jesus Martins Pombo

Licenciatura em Biologia Celular e Molecular

Modulation of Tumour Microenvironment towards Cancer Therapy

Dissertação para obtenção do Grau de Mestre em Genética Molecular e Biomedicina

Orientador: Professora Doutora Maria Alexandra Núncio de Carvalho Ramos Fernandes, Professora Auxiliar, Universidade Nova de Lisboa
Co-orientador: Professor Doutor Pedro Miguel Ribeiro Viana Baptista, Professor Catedrático, Universidade Nova de Lisboa

Júri:

Presidente: Prof. Doutor José Paulo Nunes de Sousa Sampaio
Arguente: Prof. Doutora Luísa Corvo
Vogal: Prof. Doutora Maria Alexandra Núncio de Carvalho Ramos Fernandes

FACULDADE DE CIÊNCIAS E TECNOLOGIA
UNIVERSIDADE NOVA DE LISBOA

Setembro, 2019

UNIVERSIDADE NOVA DE LISBOA
FACULDADE DE CIÊNCIAS E TECNOLOGIA
DEPARTAMENTO DE CIÊNCIAS DA VIDA

Inês de Jesus Martins Pombo

Modulation of Tumour Microenvironment towards Cancer Therapy

Dissertação para obtenção do Grau de Mestre em Genética Molecular e Biomedicina pela Universidade Nova de Lisboa, Faculdade de Ciências e Tecnologia

Orientador: Professora Doutora Maria Alexandra Núncio de Carvalho Ramos Fernandes, Professora Auxiliar, FCT/UNL
Co-orientador: Professor Doutor Pedro Miguel Ribeiro Viana Baptista, Professor Catedrático, FCT/UNL

Júri:

Presidente: Prof. Doutor José Paulo Nunes de Sousa Sampaio
Arguente(s): Prof. Doutora Luísa Corvo
Vogal(ais): Prof. Doutora Maria Alexandra Núncio de Carvalho Ramos Fernandes

Setembro, 2019

This master's thesis is associated with the following article

C. Roma-rodrigues, I. Pombo, L. Raposo, P. Pedrosa, A. R. Fernandes, and P. V Baptista, “Nanotheranostics Targeting the Tumor Microenvironment,” *Front. Bioeng. Biotechnol.*, 2019.

Modulation of Tumour Microenvironment towards Cancer Therapy

Acknowledgements

The present work was not been possible without the help and understanding of the people who accompanied me in many ways. I would like to thank to:
Prof. Alexandra Fernandes for the opportunity to develop this project and for the guidance given during the same.
Prof. Pedro Viana Baptista for also accepting me and accompanying me throughout the development of this project.
Dr. Catarina Roma-Rodrigues, Dr. Luís Raposo, Pedro Pedrosa, Daniela Ferreira and remaining members of Human Genetics and Cancer Therapeutics and Nanomedicine labs for all the availability and teachings.
Diogo Sequeira and Ana Filipa Amendoeira for the support and help that you have given me throughout this year.
Beatriz Matos, Beatriz Mariz, Diogo Sequeira, Gonçalo Santos and João Paquete for the support and post-work moments.
Claudia Fernandes and Catarina Filipe for the presence and support.
Ana Sofia Saraiva for the help, patience and motivation that you gave me even being far away.
My parents for the opportunities and support they always gave me.
My brother and, especially, my sister that help me, gave me support and listen.
Lastly to all my family.

Resumo

O cancro é, segundo a Organização Mundial de Saúde, a segunda causa de morte em todo o mundo. As terapias atuais são muitas vezes ineficazes e associadas à aquisição de resistências e ao aparecimento de efeitos secundários. Todos os dias surgem novos conhecimentos na área do cancro, tal como o facto de o microambiente tumoral (TME) ter um papel importante no desenvolvimento dos tumores, que permitem entender melhor a resposta terapêutica. A importância do TME levou, então, ao desenvolvimento de novas abordagens para estudar o cancro e de novas terapias. A Nanomedicina tem contribuído não só com novos agentes terapêuticos (exemplo as nanopartículas de ouro, AuNPs) mas também com novas abordagens que permitem diminuir o surgimento de efeitos secundários e aumentar a eficácia terapêutica.

Neste trabalho foi estudada a difusão de doxorrubicina (Dox) em monoculturas 2D (células HCT116 e HCT116 resistentes à Dox), co-culturas 2D (células tumorais e fibroblastos) e em modelos 3D de esferóides. Foi igualmente estudado o efeito de AuNPs na difusão de Dox e na viabilidade celular de HCT116 sensíveis ou resistentes a Dox em modelos 3D. Por fim foi estudado o efeito combinado das AuNPs e irradiação na difusão de Dox e na viabilidade celular dos mesmos modelos celulares 3D.

Os resultados em culturas 2D mostram que a internalização de Dox em células HCT116 é distinta da de células HCT116 resistentes à Dox, como esperado, e que a co-cultura na presença de fibroblastos influencia positivamente a internalização de Dox em células HCT116.

Verificou-se que a presença de AuNP@PEG influencia positivamente a internalização de Dox e a viabilidade celular em modelos 3D de esferóides, podendo ser utilizados como abordagem combinada. A combinação de irradiação com AuNP@PEG (como agentes fototérmicos) mostrou ser a estratégia mais promissora quer em células HCT116 bem como HCT116 resistentes à Dox, no entanto serão necessários mais estudos para comprovar estes resultados.

Palavras-Chave: Cancro; Microambiente Tumoral; Doxorrubicina; Nanopartículas de ouro; Terapia fototermal

Abstract

Cancer is, according to the World Health Organization, the second leading cause of death in the world. Current therapeutic approaches are in most of the cases ineffective and associated with the acquisition of resistance and the development of side effects. Our knowledge in cancer area emerges every day, namely by the growing importance of tumour microenvironment (TME) in cancer progression enabling to better understand tumours response to therapy. The importance of TME led to the development of new strategies to study cancer and new therapeutic approaches. Nanomedicine has been contributing not only with the development of new therapeutic agents (such as gold nanoparticles, AuNPs) but also with new therapeutic strategies that allow to reduce side effects and increase the therapeutic efficacy.

In this work we have studied the diffusion of doxorubicin (Dox) in 2D monocultures (HCT116 and HCT116 Dox resistant cells), co-cultures (tumor cells and fibroblasts) and in 3D models of spheroids. We have also studied the effect of AuNPs in Dox diffusion and in HCT116 and HCT116 Dox resistant cells viability in 3D models. The combinatorial effect of AuNPs and irradiation was also studied in the same 3D models.

2D results show that Dox internalization in HCT116 cells is different compared to HCT116 Dox resistant cells, as expected, and the co-culture in the presence of fibroblasts positively influenced Dox internalization in HCT116 cells.

AuNP@PEG positively influenced Dox diffusion and cell viability in the 3D spheroids, which may be used as combined therapy. The combination of irradiation and AuNP@PEG (as photothermal agents) showed to be the most promising strategy in HCT116 and in HCT116 Dox resistant cells, but more studies are needed to fully validate these conclusions.

Keywords: Cancer; Tumour Microenvironment; Doxorubicin; Gold Nanoparticles; Photothermal therapy

Index

Figure Index

Table Index

List of abbreviations, acronyms and symbols

ATCC	American Type Culture Collection
AuNPs	Gold Nanoparticles
AuNP@PEG	Gold Nanoparticles functionalized with PEG
CAFs	Cancer Associated fibroblasts
CME	Clatherin mediated endocytosis
CO_2	Carbon Dioxide
CTCF	Corrected total cell fluorescence
CvME	Caveolin-mediated endocytosis
DC	Dendritic cells
DMEM	Dulbecco's Modified Eagle Medium
DMSO	Dimethyl Sulfoxide
DNA	Deoxyribonucleic Acid
Dox	Doxorubicin
ECM	Extracellular Matrix
EGF	Epidermal growth factor
EPR	Enhanced permeability and retention
FBS	Fetal Bovine Serum
HCT116	Cell line derived from colorectal carcinoma
HCT116 DoxR	Cell line derived from colorectal carcinoma with resistance to Doxorubicin
Hoechst 33258	Phenol, 4-[5-(4-methyl-1-piperazinyl)[2,5'-bi-1H-benzimidazol]-2'-yl]-, trihydrochloride 23491-45-4
HTS	High Throughput screening
IC50	Half-maximal inhibitory concentration
IFN-γ	Interferon gamma
IFP	Interstitial Fluid Pressure
IL-4	Interleukin-4
IL-8	Interleukin-8
IL-10	Interleukin-10
IL-13	Interleukin-13
LDL	Low-density Lipoprotein
LDI	Laser Diode Intensity
MCP-1	Monocyte Chemoattractant Protein 1
MDSC	Myeloid-derived suppressor cells
miRNA	Micro RNA
MMP	Metalloproteinase
MMP-2	Metalloproteinase 2
MMP-9	Metalloproteinase 9

NAD+	Nicotinamide Adenine
NIR	Near-infrared
NK	Natural Killer
PBS	Phosphate Buffered Saline
PEG	Polyethylene Glycol
Pen/Strep	Penincillin/Streptomycin
PDECGF/TP	Platelet-derived Endothelial Cell Growth Factor
PDT	Photodynamic Therapy
PLL	Polylysine
PSS	Polystyrene Sulfonate
PTT	Photothermal Therapy
PVP	Polyvinylpyrrolidone
RNA	Ribonucleic Acid
RPMI	Roswell Park Memorial Institute Medium
18S	Ribosomal Protein 18S
SDF-1	Stromal-derived Factor 1
SPR	Surface Plasmon Resonance
TAM	Tumour-associated Macrophages
TANKs	Tumour-associated Natural Killer
TGF-β	Transforming Growth Factor beta
Thp-1	Cell line derived from acute monocytic leukemia
TINKs	Tumour-infiltrating Natural Killer
TNF-α	Tumour Necrosis Factor alpha
Tregs	T regulatory cells
TME	Tumour Microenvironment
UV	Ultraviolet
WHO	World Health Organization
VEGF	Vascular Endothelial Growth Factor

1. Introduction

1.1. Cancer: an overview

Cancer is a heterogeneous disease resulting from the accumulation of mutations in specific genes, namely oncogenes, tumour-suppressor genes and micro RNA (miRNA) genes. These genes are important for cellular regulation, growth and differentiation. Several type of mutations in genetic material might occur, such as base substitutions, insertions, deletions, indels, DNA rearrangements, copy number variations and epigenetic changes (1).

According to the World Health Organization (WHO), cancer is the second leading cause of death in the worldwide, with an estimated 9.6 million deaths in 2018. At the global level about 1 in 6 deaths is due to cancer. The most common cancers are lung, breast, colorectal, prostate, skin cancer (non-melanoma) and stomach and the type of cancers with high mortality are lung, colorectal, stomach, liver and breast (figure 1.1.) (World Health Organization, 2019).

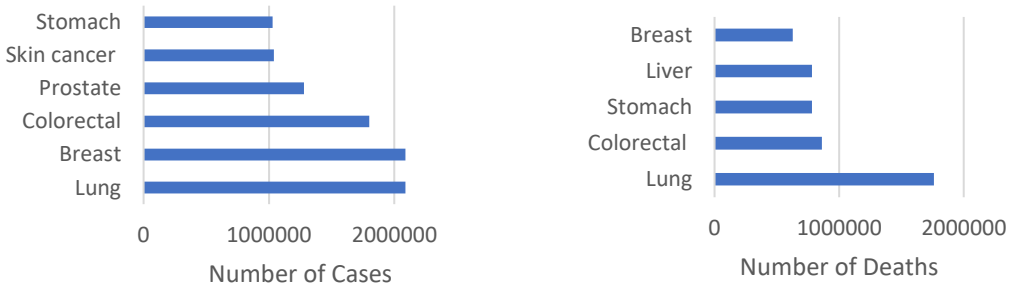

Figure 1.1 Incidence (A) and mortality (B) of the most common cancers worldwide (data from World Health Organization, 2019)

Early diagnostic is an important factor in treatment outputs and screening is a preventive measure that allows a faster therapeutic intervention at an early stage of the disease.

Current therapeutic approaches against cancer are surgery, chemotherapy and radiotherapy (2,3). Surgery is not always an option and the others, especially chemotherapy, are associated with several secondary effects (2,3). Chemotherapeutic drugs are also associated with the development of resistance to treatment due to the selective pressure in cancer cells (4), leading to survival and proliferation of certain clones of cancer cells.

New therapeutic approaches are needed for the fight against cancer. The heterogeneity of cancer requires new specific and personalized therapies. Increased knowledge about this heterogeneity provides a better understanding of cancer and for the development of new approaches with new agents or/and new targets. The specificity of therapeutic agents for cancer cells is important for achieving better results and for the decreasing of side effects. In the tumour microenvironment malignant cells work with other type of cells, such as cancer associated fibroblasts (CAFs), immune cells, endothelial cells and with other constituents like the extracellular matrix (ECM). These constituents of the tumour microenvironment are possible and appealing

new therapeutic targets. Combination of targets, agents and therapeutic approaches is the right way to increase the chances of eradicating tumour cells.

Theranostic is a new concept that consists in simultaneous use of an agent that allows diagnostic, therapy and monitoring of the therapeutic response. The implementation of this multi-approach helps to personalize of cancer therapy improving prognosis (5).

Cancer biology is a complex issue and further understanding is still needed.

1.2. Colorectal cancer

"Colorectal cancer" is a term used to reference the most common group of malignancies in the gastrointestinal tract between cecum and anus with origin in precursor cells (6,7). According to the WHO, in 2018 colorectal cancer was the third most common cancer with 1.80 million of cases in the whole world and the second deadliest cancer with 862 000 deaths (World Health Organization, 2019). The different colorectal cancer types can differ in localization (e.g. proximal or distal), pathology/histology (e.g. adenocarcinoma/serrated adenocarcinoma) and invasiveness/metastatic behaviour (e.g. locoregional or distant organ site) (6).

Manny lifestyle factors are associated to the risk of colorectal cancer development such as obesity, sedentarism, bad nutrition, smoking, most of them very common in our actual society (7). Some evidences report that the consumption of red and processed meet and the abdominal fatness, related to the lack of physical exercise, are related to the increase risk for the development of colorectal cancer (8). Hereditary factors, like hereditary diseases (e.g. familial adenomatous polyposis, Lynch syndrome), also can explain colorectal cancer development. Family history of some medical conditions, like ulcerous colitis and Chron's disease, or personal history of polyposis, colon, rectal, ovarian, endometrium, breast cancer, and diabetes mellitus are associated with the increasing of the colorectal cancer development risk (7).

The important relation between dietary and colorectal cancer development also is patent in the fact that high fiber ingestion is a prevention factor for this and other cancers (7).

1.3. Tumour Microenvironment

As explained above, neoplasic cells on the tumour are surrounded by an unique microenvironment that retains an important role in tumour initiation, progression and metastasis (9,10). Cellular processes like proliferation, apoptosis, metabolism and differentiation are, also, influenced by the tumour microenvironment (TME) and affect the tumour aggressivity (11). This microenvironment is constituted for extracellular matrix (ECM), secreted extracellular molecules and stromal cells (figure 1.2) (9).

Cancer cells recruit and reprogram stromal cells via the secretion of growth factors, chemokines and cytokines, and stromal cells, in turn, provide growth signals and intermediate metabolites to cancer cells (12). Comparing the two type of cells, stromal cells are more stable at

genetic level which leads to a decrease of susceptibility to the acquisition of resistance (12,9) and, consequently, the use of these cells as a therapeutic target can be an advantage. Stromal cells include several types of cells, such as fibroblasts, immune and vascular endothelial cells (9).

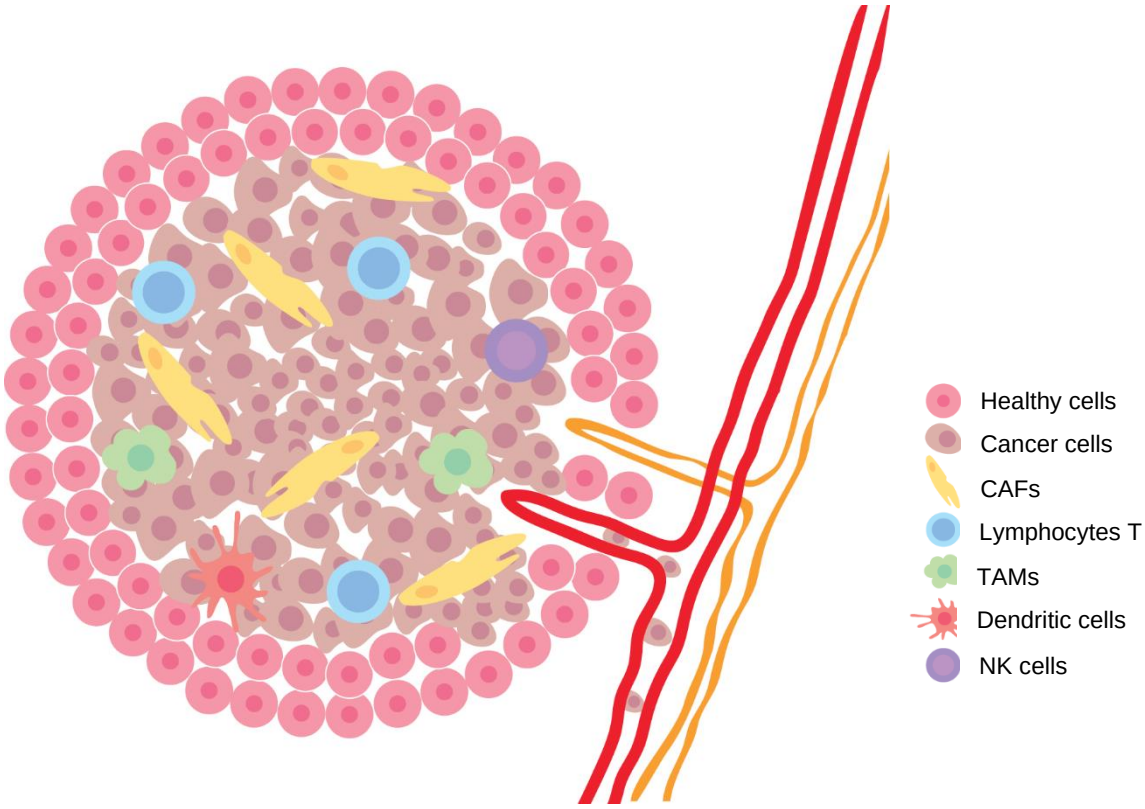

Figure 1.2 Representation of the tumour microenvironment. CAFs – Cancer-associated fibroblasts; TAMs – Tumour-associated Macrophages; NK cells – Natural Killer cells

1.3.1. Fibroblasts

Fibroblasts are the most common stromal cells (12,9) in several types of cancers and are reprogrammed by cancer cells in order to become cancer-associated fibroblasts (CAFs). These CAFs promote inflammation process (13) and play a role in several important mechanisms in tumour development, cell proliferation, invasion, metastasis, ECM remodelling and angiogenesis (12,9), through the secretion/production of molecules such as growth factors, chemokines, matrix-modifying enzymes like metalloproteinase 2 (MMP-2) and metalloproteinase 9 (MMP-9) (9). CAFs also play an important role in mediating therapeutic resistance (13).

1.3.2. Immune cells

Immune cells, mostly macrophages and lymphocytes T, infiltrate the tumour tissue but the antitumor activity is suppressed via cytokines secreted by cancer cells (9). Tumour-associated Macrophages (TAMs), regulatory T cells, Dendritic cells (DC), Natural Killer (NK) cells and

myeloid-derived suppressor cells contribute to the development of a pro-tumorigenic microenvironment (13).

The cytokines produced by TAMs leads to an adaptive immune system suppression and the specific secretion of vascular endothelial growth factor (VEGF) and interleukin (IL) -8 stimulated the endothelial cells proliferation that is necessary for angiogenesis. TAMs also play a role in tumour cell migration and invasion (13).

Lymphocytes T can differentiate into two type of cells: regulatory or cytotoxic cells. Cancer cells and stromal cells, more specifically CAFs and TAMs, produce monocyte chemoattractant protein (MCP-1), a cytokine also known as CCL2. In the presence of this cytokine the infiltrate T cells differentiated into CD4+ CD25+ T regulatory cells (Tregs) that possess an immunosuppressive behaviour. These Tregs produce transforming growth factor beta (TGF-β) and interleukin (IL)-10 that leads to the cytotoxic T-cells and natural killer cells inhibition (9).

Dendritic cells (DC) have, frequently, an unregulated activity in cancer tissues. In this way it is common the presence of a reduced number of mature DC and an increased number of immature DC with tolerogenic and immunosuppressive activity (13).

Natural Killer (NK) cells in tumour can be part of two subpopulations: tumour-infiltrating natural Killer cells (TINKs) or tumour-associated natural Killer cells (TANKs) (14). These NK cells produce high levels of pro-angiogenic factors such as VEGF and stromal-derived factor-1 (SDF-1) which promote angiogenesis and tumoral progression (15).

Myeloid-derived suppressor cells (MDSC) have an important role in the immune system evasion by tumour cells through to the immune surveillance block and T cells suppression (16). In tumours, MDSC rapidly differentiate into TAMs and, consequently, are a source of these macrophages (17).

1.3.3. Endothelial Cells and Angiogenesis

Endothelial cells are essential for angiogenesis. In solid tumours this process is required due to the need of nutrients and oxygen (9) and consequently, a massive blood vessel development occur to allow tumour growth, progression and metastization process (10,18). Endothelial cells proliferation and migration in tumour microenvironment occurs uncontrollably and leads to the formation of poorly organized blood vessels, impaired blood flow, increased hypoxic environment and increased interstitial pressure (10). The tumoral vasculature formed is, generally, disorganized (10) and presents fenestrations, pericytes deficiency and an abnormal basement membrane formation (18). This leaky vasculature and the insufficient lymphatic drainage, characteristic of the most tumours, are responsible for enhanced permeability and retention (EPR) effect (18) and might impair the entrance of the anticancer drugs in the solid tumour core (10).

1.3.4. Extracellular Matrix

The ECM is made of nanofibrous mesh proteins (for example: elastin, collagen, fibronectin , hyaluronan and laminin) which holds cells together (10,11) and ECM-associated enzymes and growth factors that influence cell proliferation and differentiation (10). ECM and secreted extracellular molecules are involved in autocrine and/or paracrine signalling pathways in order to support the tumour development (9). In fact, ECM is involved in intracellular signalling pathways of genetic expression regulation (19). ECM constituents, as enzymes and growth factors, play an important role in certain tumour processes (9). In addition to the chemical signals also mechanical signals associated with ECM influences the tumour progression, particularly on cellular proliferation (10,19).

1.3.5. Hypoxia, low pH and Necrose

The hypoxic environment is a key characteristic in solid tumours (20) and results from the imbalance between the supply of oxygen and the consumption (21,22). The creation of poorly organized blood vessels leads to the impairment of blood supply (21,23) and, consequently, to the creation of environments with low levels of oxygen. This characteristic of tumours promotes the expression of angiogenic factors such as VEGF (22,24) and platelet-derived endothelial cell growth factor (PDECGF/TP) (21) and influences gene expression (21). VEGF promotes angiogenesis through the induction of endothelial cells proliferation (21). Hypoxia also is responsible for radiotherapy resistance (20) and some chemotherapeutics resistances (22).

Tumour tissue also is characterized by low pH (18,22,25) that varies within the tumour area (18). The pH in solid tumours varies between the 6.5 and 6.8 whereas the pH of normal cells is about 7.4 (25). Proliferating tumour cells have an abnormal glucose metabolism once that these cells change from oxidative phosphorylation to glycolysis (22). This change leads to the increase of glycolysis rate and, consequently, to the increase of lactate levels (18,22). In glycolysis, the pyruvate is transformed into lactate in order to generate nicotinamide adenine NAD+. Lactate, in its turn, is transported to the extracellular environment due to the need to promote metabolic flow and to avoid reaching cytotoxic levels of lactate and, in this way, the environment gets more acidic (18).

The impairment of blood supply results in the lack of oxygen (hypoxia) and nutrients, which, in its turn, leads to necrotic cell death in tumour's core (26). Necrotic cells release pro-inflammatory factors that promote inflammation and, consequently, angiogenesis (26,27) and tumour cells surveillance (26). Necrosis is a morphologic marker of cancer (27) and stimulated tumoral growth (26,27). Necrotic cell death also is correlated with reduced vascular maturation and presence of vascular invasion which is associated to metastasization (27).

The result of these characteristics of tumour microenvironment makes tumours composed, essentially, by tree zones. The outermost zone, the proliferative zone, is the region with more cell proliferation, less interstitial pressure and more oxygen supply. The middle zone, named

quiescent zone, is characterized by higher interstitial pressure and a middle level of cell proliferation and oxygen supply (28), cells in this region are in senescence (29). And the necrotic zone, the tumour's core, that is the region without cell proliferation, low oxygen supply and high interstitial pressure (28). The existence of these regions in tumours is pointed out as responsible for the lack of therapeutic efficiency of drugs and drugs nanocarriers (29).

1.4. 3D Culture

In vitro cancer research is mainly performed using two-dimensional (2D) cell models. In these 2D models, adherent cells growth attached to the coated microplate surface as a monolayer (11). Although these 2D models are well accepted and used, they do not properly mimic the behaviour of cells *in vivo* and this is one of the reasons associated with the failure of preclinical trials for several molecules (28). In particular, 2D models of single tumour cells or co-cultures of different cell types do not mimic the tumour 3D complex microenvironment and, consequently, do not present important characteristics for cancer progression such as hypoxia, variable cell proliferation regions, EMC stimuli and gradients of soluble factors, nutrients, metabolic waste, and oxygen (28,30). Anticancer drug gradients common in 3D tumours are absent in 2D monolayers and are crucial for the tumour response to drugs (31). Interactions cell-matrix and cell-cell also are lost or reduced in the 2D model, and both are important for cell function, differentiation and proliferation *in vivo* (11,28). In 2D monolayer, signalling pathways might be differentially activated resulting in increased sensitivity to drugs and false positives results in *in vitro* tests (28,31). On the other side, in 2D culture, drug targets may not be expressed and lead to false negatives occurrence in *in vitro* tests (28).

In order to circumvent these bottlenecks, in the last years 3D cultures techniques have emerged. The cell behaviour in a 3D culture are closer to the *in vivo* behaviour, in terms of the existence creation of oxygen, nutrients and drugs gradients, variable cell proliferation regions and more interactions cell-matrix and cell-cell (28). In 3D environments, hypoxia and necrotic areas can development and the gene expression profile can be closer to the *in vivo* profile than in a 2D monolayer (31). Cancer's research has been improved by the development of novel techniques for generation of 3D models (30,32).

Despite the many advantages of 3D culture there are also some disadvantages. At the laboratorial level the development of 3D models needs optimization and standardization to reduce the variation and, at the biological level, the lack of vascularization leads to the impairment of oxygenation and removal of metabolic products (32). However, the existence of hypoxia core and the different tumour regions are better mimicked (32).

A variety of 3D technologies exist and can be divided in scaffold based and non scaffold-based technologies. The first type includes polymeric hard scaffolds, biologic scaffolds and micropatterned surface microplates (28), and cells grow in 3D platforms that mimic the ECM (29). The second type of technology incorporates hanging drop microplates, spheroid microplates

containing ultra-low attachment coating and microfluidic 3D cell cultures (28) and cells grow in ECM produced by themselves (29).

1.4.1. Spheroids

Spheroids are cellular aggregates in which the cells grow and secrete the ECM components (29,33) and mimic several important aspects of *in vivo* solid tumours. These structures reproduce tumour characteristics such as growth kinetics, cell-cell interactions and signaling, internal structure, ECM deposition, ECM-cell interactions, gene expression and drug resistance (29). Cells are cultured in conditions that leads to the increased adhesive forces between cells versus forces between cells and artificial substrate (30). Adding to the proximity of spheroids to *in vivo* tumours, several techniques have been optimized for high throughput screening (HTS) (29,33) and spheroid culture has been well-characterized (11).

3D spheroids can be created with cancer cells, originating homotypic spheroids, or cancer cells and other cells, like stromal cells, originating heterotypic spheroids which allows the recreation of cellular heterogeneity (34). Many cells naturally create aggregates and, in this way, create specific microenvironments and apical and basolateral polarities like those *in vivo* (32).

The layers formed in real tumours are visible in spheroids (>200 µm) which presents peripherical proliferative cells, internal senescent cells and the necrotic core (29,35). The oxygen and nutrients gradients and the growth profile are responsible for this formation (29). The growth profile is characterized by two stages: initially there is an exponential increased in the volume growth and, subsequently, a decrease in the rate of volume growth contributing to the maintenance of a constant volume (29).

The drug resistance, a major problem in cancer therapy, can be due to the impairment of drug penetration that also occurs in spheroids. The ECM deposition, interstitial fluid pressure (IFP) and ECM-cell and cell-cell interactions limits the penetration of drugs (29).

1.5. Chemotherapeutic Drugs - Doxorubicin

Doxorubicin (Dox) is one of the most commonly used anti-tumour agents. This therapeutic agent is an anthracycline (35,36) that causes cell death through two main mechanisms: DNA intercalation that leads to impairment of DNA transcription and replication and the binding and inactivation of topoisomerase II. By coupling these actions, Dox have an antiproliferative effect and induce DNA damage (36,37) that leads to apoptosis (37). Dox also induces DNA damage and lipid peroxidation through the generation of free radicals due to its quinone group involved in redox process (36). Despite the induction of apoptosis several descriptions also show that necrosis is also induced (38).

Despite the common use of Dox, this chemotherapeutic drug is associated to several side effects and drug resistance (35). Among the side effects, the heart damages stand out, specifically, cardiomyopathy and congestive heart failure (39). Side effects are one of the reasons

why new therapeutic strategies need to be developed, including new agents and combinations of existing therapies in order to reduce the amount of drug used.

1.6. Gold Nanoparticles

The use of nanomedicine in cancer therapy has paved the way for improving detection, delivery of active molecules (drugs, silencing agents, targeting agents, etc) providing new therapeutic approaches and theranostic. Gold nanoparticles (AuNPs) are a potential tool for cancer therapy and diagnostics due to its optical and physics properties, surface plasmon resonance (SPR), large surface area to volume ratio, and to the possibility to control size and shape. Beyond all this AuNPs can function as carriers via surface functionalization (2).

AuNPs can be synthesized through physical, chemical and biological processes. The biological synthesis is new and environmentally friendly (2,40). Physical synthesis is based in microwave and ultraviolet (UV) irradiation, laser ablation, sonochemical method, photochemical and radical induced methods (2,40). Chemical synthesis is associated with impacts on the environment and human health and extreme conditions (e.g. pH, temperature) of synthesis are required (2). Gold Nanoparticles were synthesized for the first time by Faraday in 1857, the method used is based on the use of phosphorous to reduce the gold chloride and carbon disulphide to stabilize (41). A very common method of AuNP synthesis is based on the reduction of hydrogen tetrachloroaurate by sodium borohydride, trisodium citrate or phosphorous. Citrate can be use as reducing agent and stabilizer through the capping of AuNPs surface (40).

Nowadays, a variety of gold nanoparticles which differs in shape and size exist such as gold nanospheres (2 and 100 nm), gold nanorods (10 and 100 nm), gold nanoshells (approximately 100 nm; consists in one dielectric core (i.e., silica) coated with a gold layer), and gold nanocages (40 and 50 nm) (5). These nanoparticles can be used in tumour imaging, photothermal therapy (PTT), photodynamic therapy (PDT) and as carriers (5). Different methods of production allow the synthesis of these different types of AuNPs (42).

1.6.1. Optical Properties of AuNPs

The oscillating electromagnetic field of light lead to collective oscillation of free electrons of gold. The surface plasmon resonance (SPR) is the amplitude of maximum oscillation at a specific frequency (5). The alteration of size, shape and structure of AuNPs changes the SPR wavelength which can be tuned from the visible to the near-infrared (NIR). Near infra-red (NIR) light is used in therapy approaches because in these wavelengths the tissue has minimal absorption (5). The absorption and scattering of light are two important phenomena in AuNPs utilization for imaging and detection of cancer. Scattering of light also is influenced by size and shape of nanoparticles (5).

1.6.2. Cytotoxicity and Biodistribution of AuNPs

Gold nanoparticles cytotoxicity is associated with several characteristics of these nanoparticles, such as the size, shape, environmental scenario, synthesis process, surface chemistry and targeting ligand (2,5), but the gold core is usually inert, non-toxic and biocompatible (5). Regarding the existence or not of cytotoxic effects of gold nanoparticles, studies are still necessary because there are data that point to both hypotheses. Despite the possibility of toxicological studies using animals, it is difficult to predict the influence of nanoparticle size on their toxicity since the size of endothelial cells' fenestrae is highly variable and affects the clearance of nanoparticles (43).

As well as cytotoxicity also biodistribution and pharmacokinetics are influenced by the physicochemical properties of nanoparticles including size, shape, charge and surface coating. The stabilizing capacity of some ligands may be compromised due to the physiological environment. This environment presents high content of salt that causes the annulment of the repulsive electrostatic forces and consequently the AuNPs aggregation (44).

Immune response is one important issue when introducing foreign objects into the body. Immune cells removed of circulation these objects and reduce their half-life (5). Blood proteins in circulation can bind AuNPs and form large complexes which trapped in the capillary endothelium of lung or trigger an immune response (5). Gold nanoparticles can be masked and, in this way, not recognized by the immune system. Cellular membrane of blood cells can be used to mask nanoparticles, the “self-markers” presents in membrane are responsible for evasion to the immune system (5).

The renal clearance is an important factor and the size of AuNPs is responsible for the occurrence or non-occurrence of glomerular filtration (3). Nanoparticles with a size > 8 nm can avoid renal clearance (5) while those with a size < 6 nm undergo renal clearance (3,5). The route of clearance and the biodistribution of nanoparticles are influenced by the size (3). In order to extravasate the vasculature and avoid renal filtration and liver capture, nanoparticles must be 10-100 nm and a neutral or anionic charge (18).

1.6.3. Surface Functionalization

Thiol shows a high affinity for gold and is used to stabilize gold nanoparticles (5), so AuNPs can be functionalized by thiol linkers (45). Ligands with amine or phosphine groups may also function as stabilizing agents since they have affinity to the gold surface (5). The use of stabilizing agents leads to increased stability of AuNPs and allows the functionalization with different agents, such as drugs, targeting ligands, protein or peptides, nucleic acids, imaging agents, photosensitisers, moieties bioactive/bioresponsive among others (figure 1.3). The functionalization of surface influences cellular uptake and cytotoxicity of AuNPs (5).

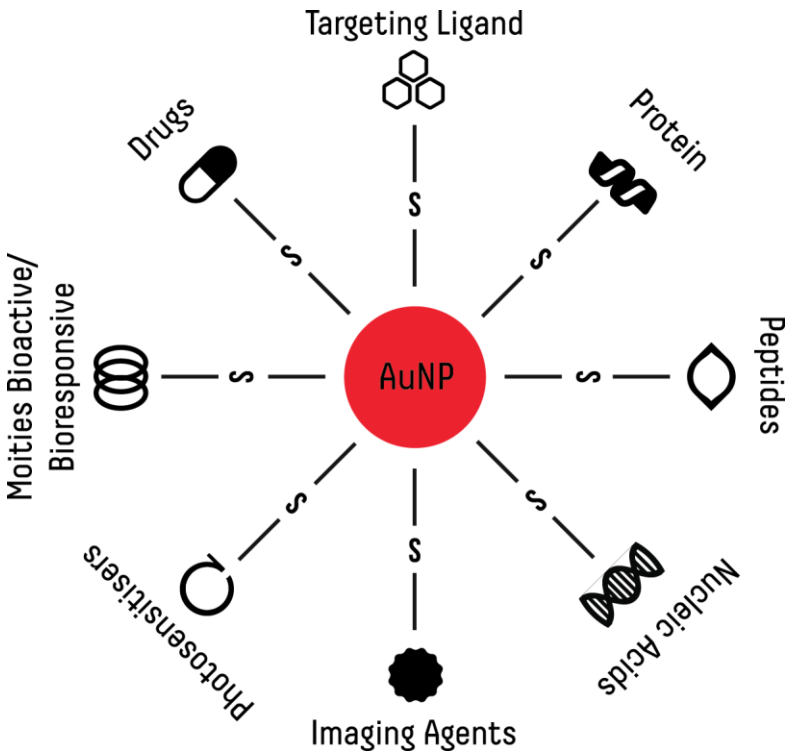

Figure 1.3 AuNPs functionalization with different molecules for therapeutic approaches.

Targeting ligands allows the directing of nanoparticles to a cancer tissue (5). The possibility of targeting cancer cells is an important goal in therapy because it leads to the reduction of side effects. Without this type of ligands passive targeting occurs based on two aspects presented in cancer cells: the high endocytic uptake and the weak vasculature around the tumour that is in the basis of the enhanced permeability and retention effect (EPR) (3). Passive targeting via EPR effect is common but presented some disadvantages. Tumours are heterogeneous and EPR effect also is variable (46) depending on the vascularization and angiogenesis degree (18), besides that some tumours, like prostate and pancreatic tumours, not presented this effect (18). The size of nanoparticles also is an important feature and smaller particles diffuse and do not stay accumulated in tumour tissue (18). Considering the disadvantages of passive targeting it became necessary the use of active targeting and several mechanisms can be used for this end. Nanoparticles can be functionalized with molecules, antibodies or peptides, that can bind to receptors or other molecules overexpressed in tumour cells (18,46,47). There are several targeting ligands like antibodies, peptides/proteins [e.g. transferrin, epidermal growth factor (EGF)], folic acid, folates aptamers, hormones, glucose molecules and DNA/RNA (3).

The new discoveries in the tumour microenvironment area allowed the use of some characteristics as targets or activation buttons. Moieties bioactive/bioresponsive can be sensitive to tumoral microenvironment and respond to stimuli in this environment. These moieties can be pH-sensitive linkers, matrix metalloproteinase [MMP]-sensitive linkers, temperature-sensitive linkers, fusogenic/synthetic peptides, and endosomal membrane-disruptive materials (5).

Chemotherapeutics drugs can be attached to the surface of nanoparticles or be loaded (2,48) and in this way the gold nanoparticles functioned as carriers. This in conjunction with active targeting is an asset to the use of some current therapies(48).

Strategies of multifunctionalization can be applied, with the simultaneous functionalization with targeting ligand (47) and imaging agents (49) or photosensitizers, or the binding of moieties bioactive/bioresponsive and a chemotherapeutic drug (48).

The stabilization of AuNPs in physiological medium can still be achieved by the binding to their surface of hydrophilic polymers, such as polyethylene glycol (PEG) (44,47,49), polylysine (PLL), polystyrene sulfonate (PSS), starches and polyvinylpyrrolidone (PVP) (44). An evaluation, that contemplated several parameters such as DNA damage, stress related enzymes and proteome profiling approach, of PEGylated AuNPs showed no significant cytotoxicity and no upregulation of proteins involved in oxidative damage (50).

1.6.4. Internalization of AuNPs

The cells have a vesicular transport mechanism called endocytosis that presents different pathways known as phagocytosis and pinocytosis and are responsible for the internalization of nanomaterials and macromolecules (51). There are different mechanisms such as Clatherin mediated endocytosis (CME) that allows the internalization of several ligands as low-density lipoprotein (LDL), transferrin, growth factors and insulin; Caveolin-mediated endocytosis (CvME) that is independent of clatherin and is associated with uptake of small molecules. Both pathways, CME and CvME, are involved in the cellular uptake of AuNPs (51). The route and degree of internalization will depend on several factors: size (52), form (52), surface charge (53), surface functionalization (54), temperature (55) and cell type (54).

1.6.5. Photothermal Therapy

Photothermal therapy (PTT) consists in local induction of temperature mediated by a photon. AuNPs are capable to, due to SPR, convert light in heat (2), this conversion occurs through the electron excitation and relaxation (42,56). The heat generated by AuNPs pass to the medium via photon-photon relaxation (5). Tissues and cells also have components capable to convert light in heat (i.e. haemoglobin, cytochromes), but them require a lot of energy due to their low absorption efficiency (56). PTT is a non-invasive treatment and allows the local destruction of tumour cells due to the heat produced by internalized AuNPs (figure 1.4) (45). The temperature rises above the tolerable limit of cancer cells, which is lower them normal cells, and tumour thermal ablation occurs (45,56). Cancer cells are more photosensitive due to their microenvironment that is hypoxic, acidic and nutrient deficient (56). Near infra-red (NIR) lasers are commonly used in PTT because in these wavelengths, the tissue (2) (i.e. haemoglobin, melanin) and water (56) have minimal absorption. Visible light has been used in several medical applications, like photo cauterization of blood vessel, and has reduced penetration in tissues, which allows a larger

precision (56). In the treatment of several ocular disorders, green lasers (495-570) has been used with success. In the oncologic area, these lasers are less common but, recently, Mendes et al and Pedrosa et al demonstrated the efficiency of using a green laser (532 nm) in cancer cells irradiation and, consequently, ablation (56,57).

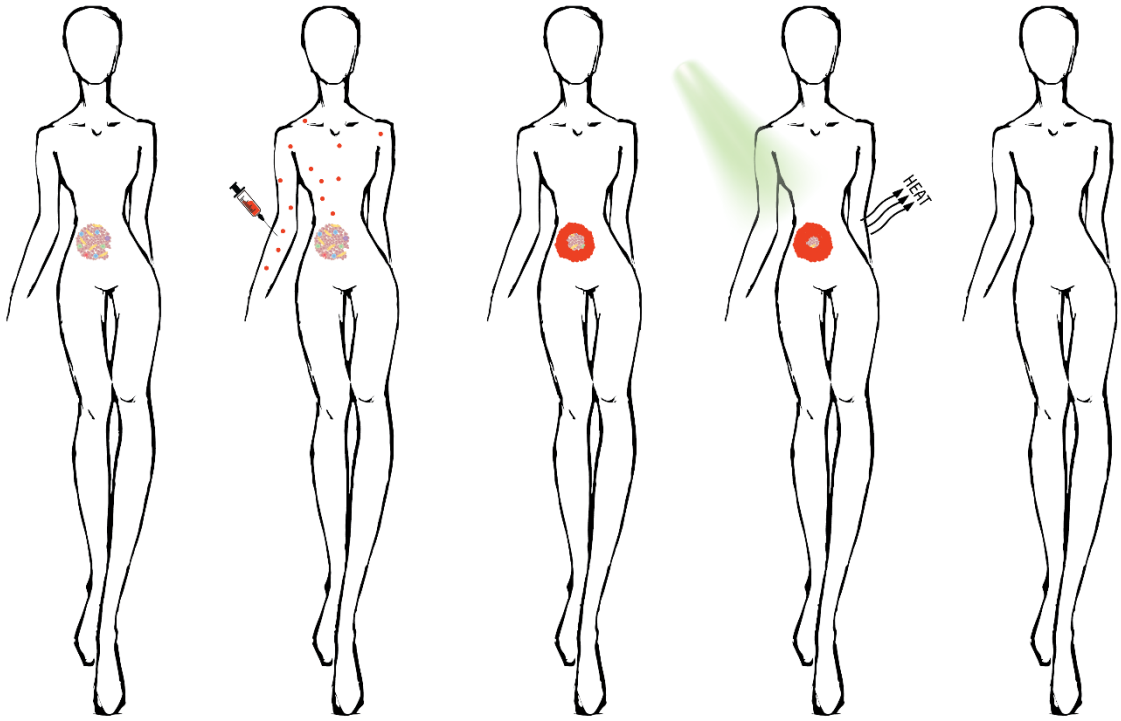

Figure 1.4 Photothermal Therapy scheme using AuNPs.

1.7. New Therapeutic targets and Combined therapy

Combined therapy may increase the chances of eradicating tumour cells and consist in multimodal treatment strategy. Several approaches can be applied together: chemotherapy, immunotherapy, hormonal therapy and gene therapy.

Multifunctional AuNPs are great tools for theranostic where a given agent allows the diagnosis, therapy and monitoring of the therapeutic response. Implementation of this concept can help in personalizing medicine and improve the prognosis (5).

One therapeutic direction may be the combination of several therapeutic targets in a single nanomaterial (e.g. various components of the tumour microenvironment) that may lead to inhibition of tumour growth (43) as well as to improve the effect of conventional therapy. Using nanoparticles as a drug delivery systems, can improve the active targeting, stability, drug controlled release with decreased toxicity (9).

The tumour ECM shows different characteristics compared to normal one. Among them, it has a high abnormally dense collagen content, which difficult drug penetration (10); additionally the interactions between cancer cells and ECM components are an obstacle to drug penetration

(10). Considering this, the matrix remodulation can be a therapeutic target to improve drug accessibility to cancer cells (10).

Stroma cells can have a therapeutic advantage since these cells are more stable at genetic level when compared with cancer cells meaning that are less susceptible to the acquisition of resistance (9).

At the therapeutic level tumour vasculature shows a determinant role. Such vasculature is weak and irregular. Therefore, leads to increase of interstitial pressure which may be a barrier to the efficient transport of drugs (10). The active targeting to abnormal vasculature and angiogenesis through nanoparticles use can improve and/or normalize vasculature allowing an easier drug dissemination (10).

The components of the immune system in the tumour microenvironment do not show an anti-tumour action and their modulation can lead to the activation of mechanisms against tumour cells. The targeting of nanoparticles to specific cells may allow the administration of cytokines and other therapeutics agents that stimulate cytotoxic T lymphocytes or inhibit immunosuppressive regulatory T lymphocytes. Additionally NK cells and dendritic cells can be also interesting therapeutic targets by improving its maturation and antigenic presentation (10). Repolarization of macrophages is another therapeutic possibility in the immune area and consists in the M2 macrophages phenotype reversal to the M1 phenotype, which have cytotoxic activity unlike M2 macrophages (9).

Besides the combination of targets belonging to the tumour microenvironment, cancer cells are the most important target in a combined therapy using nanoparticles via targeting oncogenes and pathways that are specifically activated in these cells. PTT and photodynamic therapy (PDT) also can be combinated in therapy (2) with each other or with other strategies using gold nanoparticles.

1.8. Contextualization and Motivation

The TME is responsible for tumour progression, as described above. The 2D culture is commonly used in drug discovery and tumour investigation. Since the TME is so important, the 3D cultures have gained prominence. The present thesis has as objectives the study of doxorubicin internalization in cancer cells in 2D cultures and co-cultures, the development of 3D models and the study of the impact of doxorubicin and/or AuNPs in 3D cancer models. In order to achieve these objectives, specific aims were achieved, such as the co-culture of cancer cells with fibroblasts and the development of spheroids with cancer cells.

Doxorubicin is a therapeutic agent commonly used in cancer treatment and is responsible for several side effects and resistance acquisition. Gold Nanoparticles are a potential therapeutic tool due to their intrinsic properties and have been study in this work as photothermal agent in combination with Dox or just as photothermal agent.

In the present work we have studied the internalization of doxorubicin in cancer cells (HCT116 and HCT116 DoxR) and in fibroblasts in 2D monocultures or co-cultures and 3D models

to understand the selectivity and influence of different organization/microenvironment of cells in the internalization of the drug and in the cell viability. Additionally, combinatory treatment strategies using AuNPs with and without irradiation were also assess and the cellular effect evaluated in order to understand their potential future application in colorectal cancer therapy.

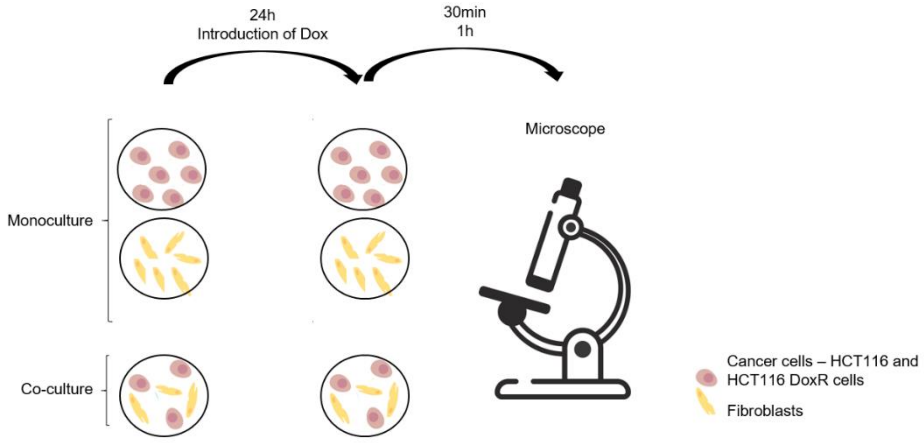

Figure 1.5 Scheme of doxorubicin internalization in 2D cultures and 2D co-cultures assays.

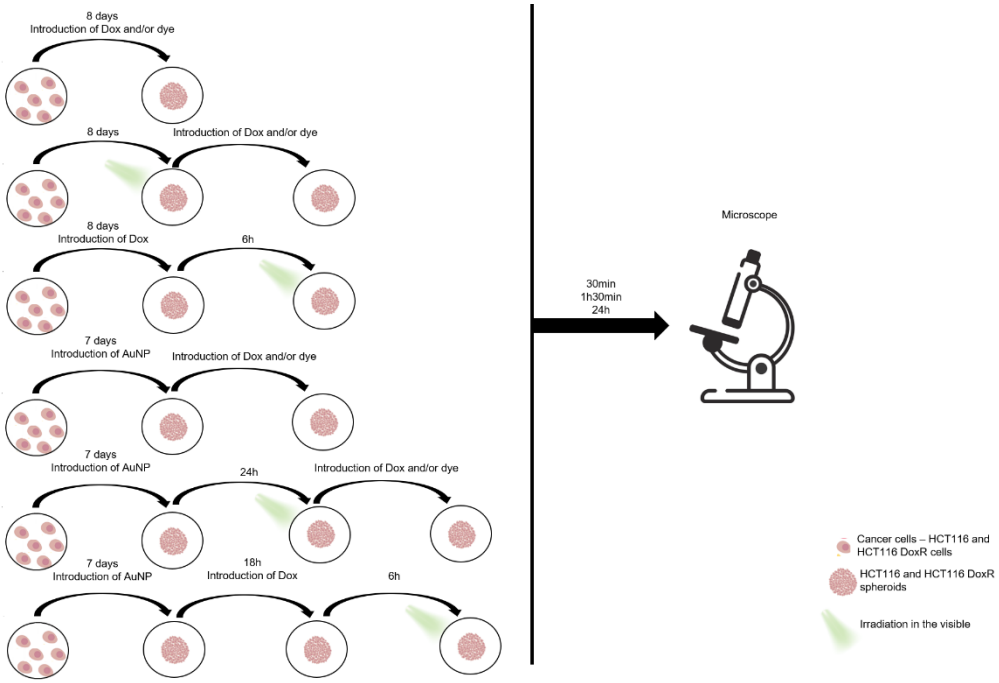

Figure 1.6 Scheme of doxorubicin internalization and viability assays performing in spheroids experiencing different treatments.

2. Materials and Methods

2.1. Human Cell Lines

The following cell lines were used in the present work: HCT116 cell line (American Type Culture Collection (ATCC) CCL-247), derived from colorectal carcinoma, HCT116 Doxorubicin-Resistant cells (HCT116 DoxR) (57), derived from HCT116 cell line, Thp-1 cell line (ATCC TIB-202) derived from acute monocytic leukemia, and primary dermal fibroblasts (ATCC PCS-201-010), derived from dermis. HCT116 and HCT116 DoxR cell lines have epithelial morphology while the primary neonatal fibroblasts have a mesenchymal morphology with spindle-shape and are bipolar and refractile. These cells are adherent unlike Thp 1 cells, monocytes isolated from peripherical blood, which are in suspension. The cells presented, except HCT116 DoxR cell line, are from American Type Culture Collection (ATCC®, Manassas, Virginia, USA). HCT116 DoxR cell line was derived from sensitive HCT116 cells that are cultured with increasing concentrations of doxorubicin (Dox) (57). The final concentration of Dox (for maintenance) of HCT116 DoxR is 3.6 μM.

Table 2.1 Characteristics of human cell lines used in the present work (disease of origin, tissue of origin, cell morphology, grow properties, age and culture medium). DMEM - Dulbecco's Modified Eagle Medium (Gibco™ by Life Technologies, Invitrogen, Carlsbad, California, USA); FBS - Fetal bovine serum (Gibco™ by Life Technologies, Invitrogen, Carlsbad, California, USA), Pen/Strep - Penicillin/Streptomycin solution (Gibco™ by Life Technologies, Invitrogen, Carlsbad, California, USA)

Cell line	Disease	Tissue	Morphology	Growth properties	Age	Culture Medium (see section 2.4)
HCT116	Colorectal carcinoma	Colon	Epithelial	Adherent	Adult	DMEM; FBS 10%; Pen/Strep 1%
HCT116 DoxR	Colorectal carcinoma	Colon	Epithelial	Adherent	Adult	DMEM; FBS 10%; Pen/Strep 1%
Thp-1	Acute monocyte leukemia	Peripherical Blood	Monocyte	Suspension	1 year infant	RPMI; FBS 10%; Pen/Strep 1%
Primary Fibroblasts	-	Dermis, skin	Spindle-shaped Bipolar, Refractile	Adherent	Neonatal	DMEM; FBS 10%; Pen/Strep 1%

2.2. Materials

Dulbecco's Modified Eagle Medium (DMEM) (Gibco™ by Life Technologies, Invitrogen, Carlsbad, California, USA)

Dulbecco's Modified Eagle Medium without fenol red (DMEM) (Gibco™ by Life Technologies, Invitrogen, Carlsbad, California, USA)

Roswell Park Memorial Institue (RPMI) (Gibco™ by Life Technologies, Invitrogen, Carlsbad, California, USA)

Fetal bovine serum (FBS) (Gibco™ by Life Technologies, Invitrogen, Carlsbad, California, USA)

Penicillin/Streptomycin solution (Gibco™ by Life Technologies, Invitrogen, Carlsbad, California, USA)

TrypLE™ Express (Gibco™ by Life Technologies, Invitrogen, Carlsbad, California, USA)

Trypan blue (Gibco™ by Life Technologies, Invitrogen, Carlsbad, California, USA)

Hoechst 33258 dye (Phenol, 4-[5-(4-methyl-1-piperazinyl)[2,5'-bi-1H-benzimidazol]-2'-yl]-, trihydrochloride 23491-45-4) (Molecular Probes® by Life Technologies, Invitrogen, Carlsbad, California, USA)

CellTox™ Green dye (Promega Corporation, Madison, Wisconsin, USA)

nzyol (nzytech, Lisbon, Portugal)

NZY M-MulV First-Strand cDNA Synthesis Kit (nzytech, Lisbon, Portugal)

TaqMan® Fast Advanced Master Mix (Applied Biosystems™ by Thermo Fisher Scientific, Waltham, Massachusetts, USA)

TaqMan® Gene Expression Assays Mix (Applied Biosystems™ by Thermo Fisher Scientific, Waltham, Massachusetts, USA) for TNF-α and 18S expression

24 well plates (SPL Life Sciences, South Korea)

Super low Attachment 96-well culture plate (Nunclon™ Sphera™ Microplate, Thermo Fisher Scientific, Waltham, Massachusetts, USA)

T flask (75 cm^2 and 25 cm^2) (SPL Life Sciences, South Korea)

Falcon tube (15 mL and 50 mL) (SPL Life Sciences, South Korea)

Doxorubicin (Dox) (Sigma Aldrich, St. Louis, Missouri, USA)

Dimethyl Sulfoxide (DMSO) (Sigma Aldrich, St. Louis, Missouri, USA)

2.3 Equipment

Laminar flow chamber

Inverted optical microscope (Nikon TMS, Nikon Instruments, Tokyo, Japan)

Inverted fluorescent microscope - Ti-U Eclipse inverted microscope – (Nikon, Tokyo, Japan)

CO_2 Incubator (Sanyo, Osaka, Japan).

Sigma 3-16K (Sigma, Osterode am Harz, Germany)

Sigma 1-14K (Sigma, Osterode am Harz, Germany)

Centrifuge 5415c (Eppendorf, Hamburg, Germany)

Nanodrop (Nanodrop ® ND 1000 Spectrophotometer)

Thermal Cycler (Bio-Rad, Hercules, California, USA)

Rotor-gene (Corbett Research)

Hemocytometer

2.4. Cell Culture

HCT116 cells and fibroblasts were cultured in Dulbecco's Modified Eagle Medium (DMEM) (Gibco™ by Life Technologies, Invitrogen, Carlsbad, California, USA) supplemented with 10 % (v/v) fetal bovine serum (FBS) (Gibco™ by Life Technologies, Invitrogen, Carlsbad, California, USA), 1 % (v/v) Pen/Strep solution (solution with penicillin 10000 U/mL, streptomycin 10000 µg/mL) (Gibco™ by Life Technologies, Invitrogen, Carlsbad, California, USA). Thp-1 cells were cultured in Roswell Park Memorial Institue (RPMI) (Gibco™ by Life Technologies, Invitrogen, Carlsbad, California, USA) supplemented with 10 % (v/v) fetal bovine serum (FBS) (Gibco™ by Life Technologies, Invitrogen, Carlsbad, California, USA), 1 % (v/v) Pen/Strep solution (solution with penicillin 10000 U/mL, streptomycin 10000 µg/mL) (Gibco™ by Life Technologies, Invitrogen, Carlsbad, California, USA).

All cells were subcultured when 80% of confluence was reached to avoid contact inhibition and lack of nutrients. Every day, cultures were observed under an inverted optical microscope (Nikon TMS, Nikon Instruments, Tokyo, Japan) for the presence of possible contaminants and cell growth and morphology analysed.

Screening for mycoplam contamination was performed weekly via PCR of total genomic DNA extracted from the cultures (work performed by laboratory colleagues).

Following analysis of confluence state, medium was removed, and cells washed with Phosphate Buffered Saline (PBS) 1x. Then TrypLE™ Express (Gibco™ by Life Technologies, Invitrogen, Carlsbad, California, USA) was added to dissociate adherent cells by cleavage of the peptide bonds on the C-terminal sides of lysine and arginine. When the cells were in suspension, the enzyme was inhibited through the addition of fresh culture medium. Cell suspension was transferred to a new 15 mL Falcon tube (SPL Life Sciences, South Korea) and centrifuged for 5 minutes at 300 g, 15 °C (Sigma 3-16K, Sigma, Osterode am Harz, Germany). The supernatant was removed, and the cell pellet resuspended in the respective medium. Cells were then counted using a hemocytometer and the trypan blue (Gibco™ by Life Technologies, Invitrogen, Carlsbad, California, USA) exclusion method (see section 2.4.1.). After counting, cells were inoculated at the density required in a new T flask of 75 cm^2 (SPL Life Sciences, South Korea) with 10 mL of fresh supplemented medium for cancer cells or with 15 mL of fresh supplemented medium for primary fibroblasts (in the case of using a new T flask of 25 cm^2 (SPL Life Sciences, South Korea) the volume of fresh supplemented medium was 5 mL). Followed inoculation cells were incubated at 37 °C in a 99% humidity and 5% (v/v) CO_2 (Sanyo CO_2 Incubator, Sanyo, Osaka, Japan). The remaining volume of suspended cells was used as needed.

2.4.1. Cell Counting via Trypan Blue method

For trypan blue method a 10x dilution of cells was prepared in supplemented medium and mixed with a 5x dilution of trypan blue 0,4% (v/v) solution (Gibco™ by Life Technologies, Invitrogen, Carlsbad, California, USA). Cells counting was performed in an inverted optical microscope (Nikon TMS, Nikon Instruments, Tokyo, Japan). Trypan blue is an impermeable dye

for viable cells but permeable for death cells providing a simpler way of measuring cell viability. Cell concentration (cells/mL) was calculated through the multiplication of the number of cells counted by the dilution factor, in this case 10, and the hemocytometer volume (10^4 mL^{-1}) divided by the number of quadrants counted (equation 1).

Equation 1.

$$Cell\ Concentration\ (cell/mL) = \frac{number\ of\ cells\ counted\ \times dilution\ factor \times 10^4}{number\ of\ quadrants\ counted}$$

2.5. Internalization of Doxorubicin

In order to analyse doxorubicin (Dox) internalization in 2D co-culture and in 2D culture, both HCT116 cells/HCT116 DoxR cells and the human primary fibroblasts were seeded in 24 well plates (SPL Life Sciences, South Korea) at a cell density of 1.5 cells/well (ratio 1:1, according to Fernandes et al (48)) or at a cell density of 0.75 cells/well, respectively, and incubated for 24h at 37 °C in a 99% humidity of 5% (v/v) CO_2 (Sanyo CO_2 Incubator, Sanyo, Osaka, Japan). Then, cells were incubated with Dox (Sigma Aldrich, St. Louis, Missouri, USA) (see table 2.2) for further 30min to 1h. Two controls, DMSO (Sigma Aldrich, St. Louis, Missouri, USA) (in the same % as used with Dox) and untreated controls, were performed following the same conditions as before. After these periods of time, Hoechst 33258 labelling was performed (see section 2.6. Nuclei labelling). Finally, cells were observed under Ti-U Eclipse inverted microscope (Nikon, Tokyo, Japan) and 5 images acquired per well through the software for image acquisition. Images of the nucleus were obtained using an excitation in UV region (DAPI filter – excitation at 375/28 nm and emission at 469/60 nm) and images of doxorubicin in the green region (G2A filter – excitation at 535/50 nm and emission > 580 nm). The images were treated and analysed with ImageJ software that allows the obtention of data for Corrected total cell fluorescence (CTCF) calculation (equation 2). CTCF was calculated for 3 cells of each cell typology per image.

Equation 2.

$$CTCF = Integrated\ Density\ of\ selected\ cell - (Area\ of\ selected\ cell\ \times Mean\ of\ background)$$

2.6. Nuclei labelling

To staining the nucleus the medium was removed and cells incubated with Hoechst 33258 dye (Molecular Probes® by Life Technologies, Invitrogen, Carlsbad, California, USA) at 0.0075 mg/mL for 15 minutes and washed with PBS 1x. Hoechst 33258 dye (Phenol, 4-[5-(4-methyl-1-piperazinyl)[2,5'-bi-1H-benzimidazol]-2'-yl]-, trihydrochloride 23491-45-4) is a nuclear dye that binds to dsDNA and emits blue fluorescence (excitation at 352 nm and emission at 461 nm).

2.7. Spheroids formation

Spheroid formation was performed, with some changes, according *Baek et al* (35) and following the manufacturer's recommendations. Briefly, HCT116/ HCT116 DOXR cells were seeded at 5000 cells per well in super low Attachment 96-well culture plate (Nunclon™ Sphera™ Microplate, Thermo Fisher Scientific, Waltham, Massachusetts, USA), spin in an orbital shaker sense and incubated at 37 °C in a 99% humidity and 5% (v/v) CO_2 (Sanyo CO_2 Incubator, Osaka, Japan). Cells were cultured in the respective medium and observed regularly. The medium was replaced as demanded.

2.8. Spheroids Analysis

Spheroids were grown for 8 days, observed with Ti-U Eclipse inverted microscope (Nikon, Tokyo, Japan) and photographed with the respective software for image acquisition regularly during the grow process. The medium was replaced as demanded.

2.8.1. Doxorubicin Diffusion

Eighth days after initiating growth, spheroids were incubated with Dox (Sigma Aldrich, St. Louis, Missouri, USA) (see table 2.2) for 30mins, 1h30mins and 24h. At each time point, spheroids were observed, and images acquired with Ti-U Eclipse inverted microscope (Nikon, Tokyo, Japan) and respective software for image acquisition with excitation in the green region (G2A filter – excitation at 535/50 nm and emission > 580 nm). Controls with DMSO (Sigma Aldrich, St. Louis, Missouri, USA) and untreated were performed following the same conditions.

2.8.2. Spheroids: Cell Viability

Eighth days after initiating growth, spheroids were incubated with CellTox™ Green dye 1x (Promega Corporation, Madison, Wisconsin, USA) following the manufacture's recommendations. Images of membrane impairment (CellTox™ Green dye) were obtained with Ti-U Eclipse inverted microscope (Nikon, Tokyo, Japan) and respective software for image acquisition with excitation in blue region (FITC filter – excitation at 480/30 nm and emission at 535/45 nm).

CellTox™ Green dye is an asymmetric cyanine dye that binds to DNA of cells with impaired membrane integrity. Once attached to DNA the fluorescent properties of the dye are enhanced and emits green fluorescence (excitation at 485-500 nm and emission at 520-530 nm). This dye allows the observation of cell death. Cells can die through three main mechanisms: apoptosis (type I cell death), autophagic cell death (type II), and necrosis (type III). Necrosis is characterized by the loss of membrane integrity (58).

2.8.3. Spheroids: Doxorubicin Diffusion and Cell Viability

As stated in section 2.8.1, at the eighth day after initiating growth, spheroids were incubated with Dox (Sigma Aldrich, St. Louis, Missouri, USA) (see table 2.2) and CellTox™ Green dye 1x (Promega Corporation, Madison, Wisconsin, USA) for 30mins, 1h30mins and 24h. In each time point, spheroids were observed, and images acquired with Ti-U Eclipse inverted microscope (Nikon, Tokyo, Japan) and respective software for image acquisition. Images of membrane impairment (CellTox™ Green dye) were obtained with excitation in the blue region (FITC filter – excitation at 480/30 nm and emission at 535/45 nm) and images of Dox diffusion with an excitation in the green region (G2A filter – excitation at 535/50 nm and emission > 580 nm). Controls with DMSO (Sigma Aldrich, St. Louis, Missouri, USA) and untreated were performed following the same conditions as before.

2.9. Spheroids after AuNP@PEG treatment

Spheroids were grown for 7 days and were observed with Ti-U Eclipse inverted microscope (Nikon, Tokyo, Japan) and photographed with the respective software for image acquisition regularly during the grow process. The medium was replaced as needed. On the seventh day of growing, spheroids were incubated with 8 nM of gold nanoparticles functionalized with PEG (AuNP@PEG). After 24 hours of incubation spheroids were washed with PBS 1x.

2.9.1. Doxorubicin Diffusion

After spheroids wash (section 2.9), cells were incubated with Dox (Sigma Aldrich, St. Louis, Missouri, USA) (see table 2.2) as described in section 2.8.1.

2.9.2. Cell Viability

After spheroids wash, cell viability assay was performed as described in section 2.8.2.

2.9.3. Diffusion of Doxorubicin and Cell Viability

After spheroids wash, the 3D structures were incubated with Dox (Sigma Aldrich, St. Louis, Missouri, USA) (see table 2.2) and CellTox™ Green dye 1x (Promega Corporation, Madison, Wisconsin, USA) as described in section 2.8.3.

2.10. Spheroid Irradiation

Spheroids grown as described in section 2.8. Eighth days after initiating grown, spheroids were irradiated with a visible light at 532nm wavelength for 1min with LDI equal to 3.78.

2.10.1. Doxorubicin Diffusion

After irradiation spheroids were incubated with Doxorubicin (Sigma Aldrich, St. Louis, Missouri, USA) (see table 2.2) as described in section 2.8.1.

2.10.2. Cell Viability

After irradiation cell viability assay was assessed as described in the section 2.8.2.

2.10.3. Doxorubicin Diffusion and Cell Viability

After irradiation cells were incubated with Dox (Sigma Aldrich, St. Louis, Missouri, USA) and CellTox™ (Promega Corporation, Madison, Wisconsin, USA) as described in section 2.8.3.

2.11. Spheroid Irradiation after AuNP@PEG treatment

Spheroids grown as previously described for 7 days (section 2.9) and were incubated with 8 nM of gold nanoparticles functionalized with PEG (AuNP@PEG). After 24 hours of incubation, spheroids were washed with PBS 1x and irradiated with a visible light at 532nm wavelength for 1 min with LDI equal to 3.78.

2.11.1. Doxorubicin Diffusion

After irradiation spheroids were treated as described in the section 2.8.1.

2.11.2. Cell Viability

After irradiation spheroids were treated as described in the section 2.8.2.

2.11.3. Diffusion of Doxorubicin and Cell Viability

After irradiation spheroids were treated as described in the section 2.8.3.

2.12. Spheroids Irradiation after Doxorubicin treatment

Spheroids grown for 8 days as described in section 2.8, were incubated for 6 hours with Dox (Sigma Aldrich, St. Louis, Missouri, USA) (see table 2.2) and irradiated with a visible light at 532nm wavelength for 1 min with LDI equal to 3.78. After, they were observed and photographed with Ti-U Eclipse inverted microscope (Nikon, Tokyo, Japan) and respective software for image acquisition with excitation in the green region (G2A filter – excitation at 535/50 nm and emission > 580 nm), 30mins,1h30mins and 24h after irradiation.

2.13. Spheroids Irradiation after AuNP@PEG and Doxorubicin treatment

Spheroids grown for 7 days as described in section 2.9 and incubated with 8 nM of AuNP@PEG during 24h and with Doxorubicin (Sigma Aldrich, St. Louis, Missouri, USA) (see table 2.2) for 6 hours. After both incubations, spheroids were irradiated with a visible light at 532nm wavelength for 1 min with LDI equal to 3.78 followed by observation with Ti-U Eclipse inverted microscope (Nikon, Tokyo, Japan) and photographed with respective software for image acquisition with excitation in the green region (G2A filter – excitation at 535/50 nm and emission > 580 nm), after 30min, 1h30mins and 24h of the end of the irradiation process.

2.14. Spheroids with Thp-1 cells after AuNP@PEG treatment

Spheroids grown for 7 days as described in section 2.9 and were incubated with 8 nM of AuNP@PEG. After 24 hours of incubation spheroids were washed with PBS 1x and incubated with $1x10^4$ Thp-1 cells. After 24h of incubation the cells are collected separately for RNA extraction (see section 2.17.1. RNA extraction). The untreated controls were performed.

2.15. Spheroid with Thp-1 cells after irradiation

Spheroids grown for 8 days as described in section 2.8 and were irradiated with a visible light at 532nm wavelength for 1min with LDI equal to 3.78. After irradiation spheroids were incubated with $1x10^4$ Thp-1 cells during 24h and the cells collected separately for RNA extraction (see section 2.17.1. RNA extraction). The untreated controls were performed.

2.16. Spheroid with Thp-1 cells after irradiation and AuNP@PEG treatment

Spheroids grown for 7 days as described in section 2.9 and were incubated with 8 nM of AuNP@PEG. After 24 hours of incubation, spheroids were washed with PBS 1x and irradiated with a visible light at 532nm wavelength for 1 min with LDI equal to 3.78. After irradiation spheroids were incubated with $1x10^4$ Thp-1. 24h after incubation, cells are collected separately for RNA extraction (see section 2.17.1. RNA extraction). The untreated controls were performed.

Table 2.2 Doxorubicin concentrations according to the cells of work.

Cells	Dox concentration
HCT116	8 µM
HCT116 Dox resistant	6 µM and 120 µM

2.17. TNF-α expression analysis

The Tumour Necrosis factor alpha (TNF-α) expression was analysed in order to evaluate the activation of inflammation. The TNF-α is a proinflammatory cytokine involved in several cell processes like cell proliferation, differentiation, apoptosis, lipid metabolism, coagulation (Gene ID: 7124, HGNC:HGNC:11892). The ribosomal protein 18S (18S) expression is a control used due to the fact of this protein is a component of 40S subunit, the small subunit of ribosomes (Gene ID: 6222, HGNC:HGNC:10401).

2.17.1. RNA extraction

Thp-1 cells were separated from HCT116/HCT116 DoxR spheroids. Each type of cells was centrifugated at 500 g, room temperature for 5mins (Sigma 1-14K (Sigma, Osterode am Harz, Germany)). The resulting pellet was resuspended in nzyol (nzytech, Lisbon, Portugal) and chloroform was added in the proportion nzyol:chloroform of 500µL:200µL. Then was centrifugated at room temperature for 5 min (Centrifuge 5415c (Eppendorf, Hamburg, Germany)) and the aqueous phase is separated. Two and a half volumes of isopropanol were added and incubated at -20°C overnight for RNA precipitation. In the next day, the solution was centrifugated at 13000g, 15°C for 15 mins (Sigma 3-16K (Sigma, Osterode am Harz, Germany)). The resulting pellet was resuspended with ethanol 75% and centrifugated at 10000g, 4°C for 5 mins (Sigma 3-16K (Sigma, Osterode am Harz, Germany)). The supernatant was discarded, and the pellet was air-dried and resuspended with 10 µL of DEPC water preheated at 70°C. Lastly, the solution was incubated at 70°C for 5 mins. RNA solution is quantified using Nanodrop (Nanodrop ® ND1000 Spectrophotometer) and stored at -80°C.

2.17.2. cDNA synthesis

After RNA extraction cDNA synthesis was performed using NZY M-MulV First-Strand cDNA Synthesis Kit (nzytech, Lisbon, Portugal) following the manufacture's recommendations in the thermal cycler (Bio-Rad, Hercules, California, USA).

2.17.3. Quantitative PCR (qPCR)

Real time qPCR was performed according to manufacturer´s specifications in the rotor-gene (Corbett Research). For this step we used the TaqMan® Fast Advanced Master Mix (Applied Biosystems™ by Thermo Fisher Scientific, Waltham, Massachusetts, USA) and TaqMan® Gene Expression Assays Mix (Applied Biosystems™ by Thermo Fisher Scientific, Waltham, Massachusetts, USA) for *TNF-α* and *18S* expression.

2.17.4. Analysis of Real-Time PCR data

Analysis of *TNF-α* relative gene expression was performed using the $2^{-\Delta\Delta C_T}$ method. In this method two samples are compared, and each sample is correlated to an internal control gene (in this study the *18S* gene). The method was performed according to equation 2 where A is the sample of interest and B the control sample. The result show the relative expression of A compared with B (59).

Equation 2.

$$2^{-\Delta\Delta C_T} = 2^{-[(C_T\ gene\ of\ interest - C_T\ internal\ control\ gene]_A - [(C_T\ gene\ of\ interest - C_T\ internal\ control\ gene]_B}$$

2.18. Statistical Analysis

Statistical analysis of data was performed using GraphPad Prism program (version 8.0). The one-way ANOVA test with multiple comparisons was performed to compare the different experimental groups of data.

3. Results and Discussion

3.1. Internalization of Doxorubicin

Stromal cells are part of the tumour microenvironment and play an important role in tumour growth and maintenance (12). These cells interact with cancer cells and influence the drug penetration (29). Fibroblasts, more specifically CAFs, are the most common stromal cells in TME and are associated to therapeutic resistance and ECM remodulation (13). The ECM also play an important role in TME and its elevated density is responsible for the impairment of drug penetration (29). In order to fully understand drug internalization in these complex 3D systems, we need first to understand how they internalize different type of cells in the TME, using Dox as a model of anti-tumour agent.

In a first approach the internalization of Dox, over time, in HCT116, HCT116 DoxR and fibroblasts 2D cultures and in HCT116-fibroblasts and HCT116 DoxR-fibroblasts 2D co-cultures was evaluated by fluorescence microscopy with simultaneous nuclei labelling with Hoechst 33258. This dye is cell permeable and bind specifically to adenine and thymine staining the DNA (60).

As expected, the results show the localization of Dox in the nucleus of HCT116 cells in 2D cultures (figures 3.1 and 3.2) and when co-cultured with fibroblasts (figure 3.3) at 30min and 1h. In 2D cultures of fibroblasts (Fib) (figures 3.3, 3.4 and 3.5) Dox is located mostly also in the nucleus, but the presence of Dox in the cytoplasm seams to increase over time (figures 3.4 and 3.5). The internalization of Dox, in 2D cultures and co-cultures, increased significantly for HCT116 cells, but for Fibroblasts no significant differences were observed (figure 3.6).

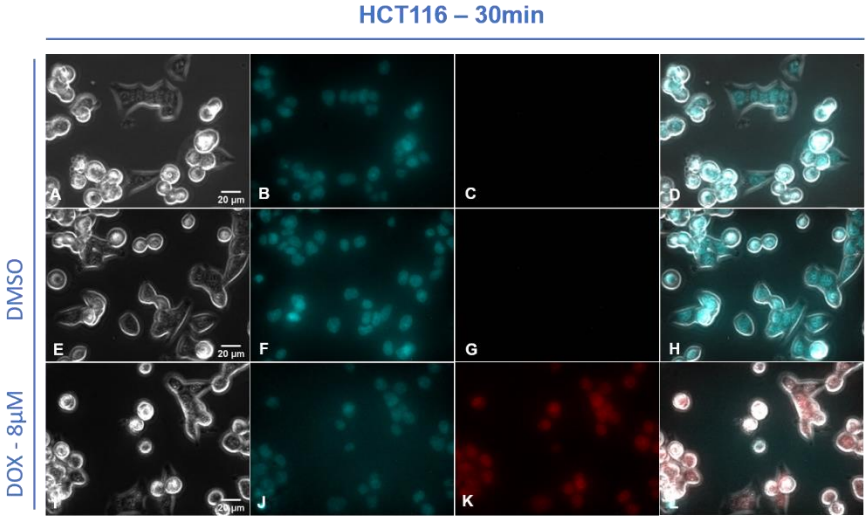

Figure 3.1 Fluorescence microscopy images of 2D culture of HCT116 cells after 30 min of incubation in the presence or absence of Dox. Nucleus are stained with Hoechst (blue). Cells were incubated with 8µM of Dox (red) or 0.1% of DMSO according to the referenced for 30min. (A) Bright field image of HCT116 cells (B) Image acquired with UV excitation of HCT116 cells – Nucleus (C) Image acquired with green excitation of HCT116 cells (D)Combined image of (A), (B) and (C) images (E) Bright field image of HCT116 cells (F) Image acquired with UV excitation of HCT116 cells – Nucleus (G) Image acquired with green excitation of HCT116 cells (H)Combined image of (E), (F) and (G) images (I) Bright field image of HCT116 cells (J) Image acquired with UV excitation of HCT116 cells – Nucleus (K) Image acquired with green excitation of HCT116

cells (L)Combined image of (I), (J) and (K) images. The presented images were treated with ImageJ software.

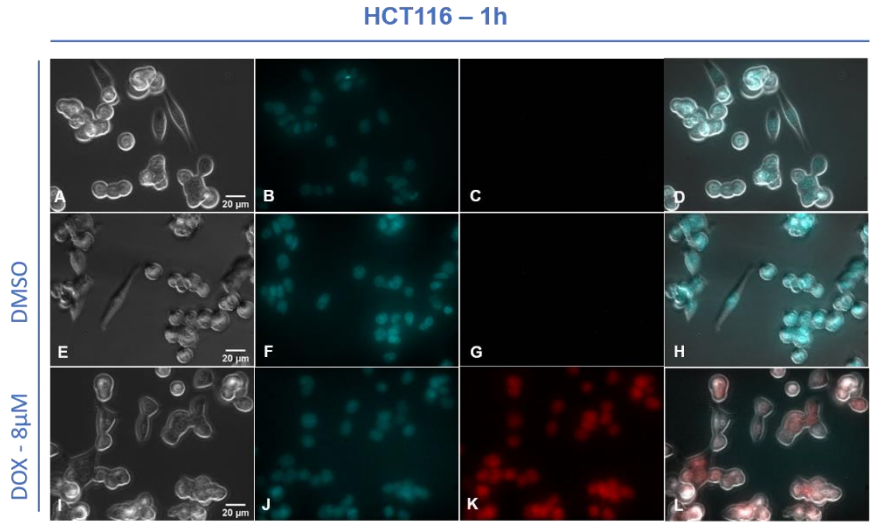

Figure 3.2 Fluorescence microscopy images of 2D cultures of HCT116 cells after 1h of incubation in the presence or absence of Dox. Nucleus are stained with Hoechst (blue). Cells were incubated with 8µM of Dox (red) or 0.1% of DMSO according to the referenced for 1h. (A) Bright field image of HCT116 cells (B) Image acquired with UV excitation of HCT116 cells – Nucleus (C) Image acquired with green excitation of HCT116 cells (D)Combined image of (A), (B) and (C) images (E) Bright field image of HCT116 cells (F) Image acquired with UV excitation of HCT116 cells – Nucleus (G) Image acquired with green excitation of HCT116 cells (H)Combined image of (E), (F) and (G) images (I) Bright field image of HCT116 cells (J) Image acquired with UV excitation of HCT116 cells – Nucleus (K) Image acquired with green excitation of HCT116 cells (L)Combined image of (I), (J) and (K) images. The presented images were treated with ImageJ software.

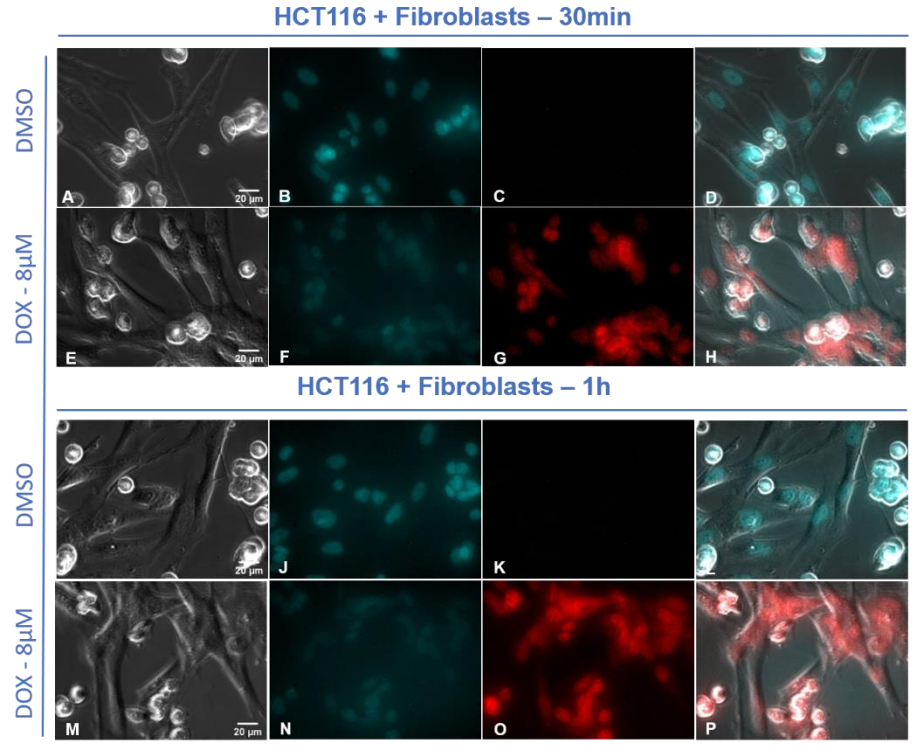

Figure 3.3 Fluorescence microscopy images of 2D co-culture of primary fibroblasts and HCT116 cells (ratio 1:1). Nucleus are stained with Hoechst (blue). Cells were incubated with 8µM of Dox (red) or 0.1% of DMSO according to the referenced for 30min to 1h. (A) Bright field image (B) Image acquired with UV excitation – Nucleus (C) Image acquired with green excitation (D)Combined image of (A), (B) and (C) images (E) Bright field image (F) Image acquired with UV excitation – Nucleus (G) Image acquired with green excitation (H)Combined image of (E), (F) and (G) images (I) Bright field image (J) Image acquired with UV excitation

– Nucleus (K) Image acquired with green excitation (L)Combined image of (I), (J) and (K) images (M) Bright field image (N) Image acquired with UV excitation – Nucleus (O) Image acquired with green excitation (P)Combined image of (M), (N) and (O) images. The presented images were treated with ImageJ software.

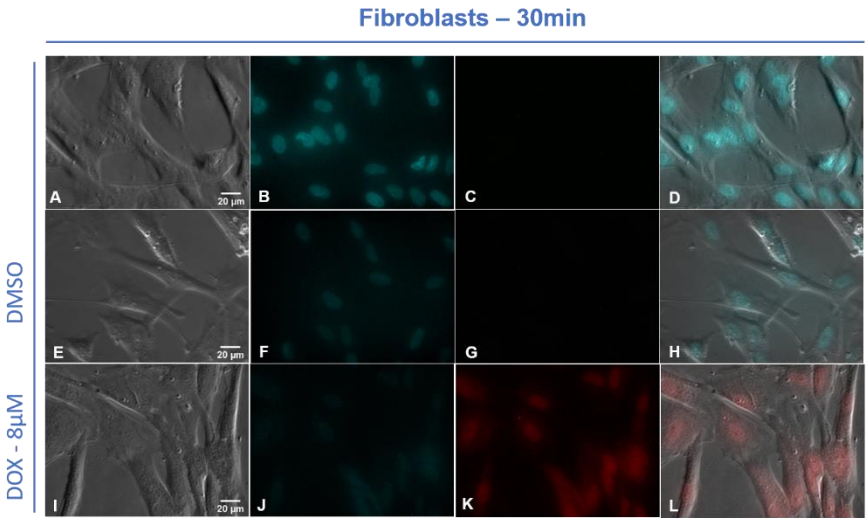

Figure 3.4 Fluorescence microscopy images of 2D cultures of primary fibroblasts after 30 min of incubation in the presence or absence of Dox. Nucleus are stained with Hoechst (blue). Cells were incubated with 8µM of Dox (red) or 0.1% of DMSO according to the referenced for 30min. (A) Bright field image of primary fibroblasts (B) Image acquired with UV excitation of primary fibroblasts – Nucleus (C) Image acquired with green excitation of primary fibroblasts (D)Combined image of (A), (B) and (C) images (E) Bright field image of primary fibroblasts (F) Image acquired with UV excitation of primary fibroblasts – Nucleus (G) Image acquired with green excitation of primary fibroblasts (H)Combined image of (E), (F) and (G) images (I) Bright field image of primary fibroblasts (J) Image acquired with UV excitation of primary fibroblasts – Nucleus (K) Image acquired with green excitation of primary fibroblasts (L)Combined image of (I), (J) and (K) images. The presented images were treated with ImageJ software.

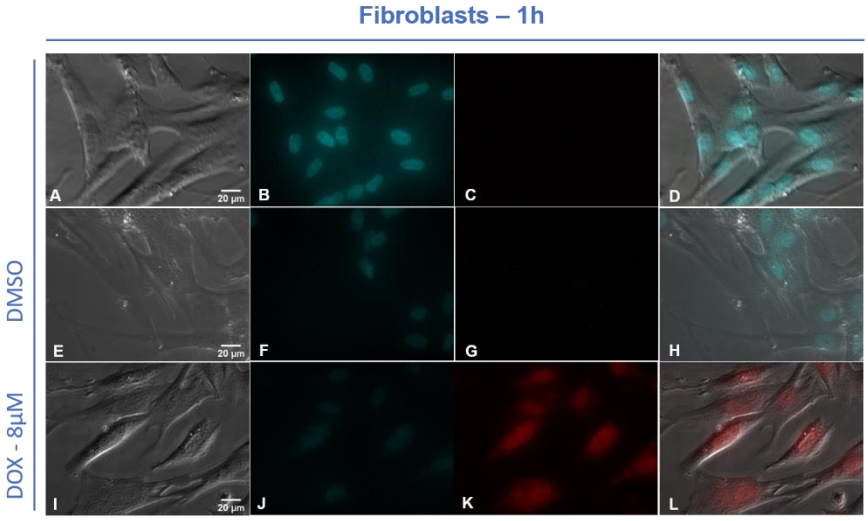

Figure 3.5 Fluorescence microscopy images of 2D cultures primary fibroblasts after 1H of incubation in the presence or absence of Dox. Nucleus are stained with Hoechst (blue). Cells were incubated with 8µM of Dox (red) or 0.1% of DMSO according to the referenced for 1h. (A) Bright field image of primary fibroblasts (B) Image acquired with UV excitation of primary fibroblasts – Nucleus (C) Image acquired with green excitation of primary fibroblasts (D) Combined image of (A), (B) and (C) images (E) Bright field image of primary fibroblasts (F) Image acquired with UV excitation of primary fibroblasts – Nucleus (G) Image acquired with green excitation of primary fibroblasts (H) Combined image of (E), (F) and (G) images (I) Bright field image of primary fibroblasts (J) Image acquired with UV excitation of primary fibroblasts – Nucleus (K) Image acquired with green excitation of primary fibroblasts (L)Combined image of (I), (J) and (K) images. The presented images were treated with ImageJ software.

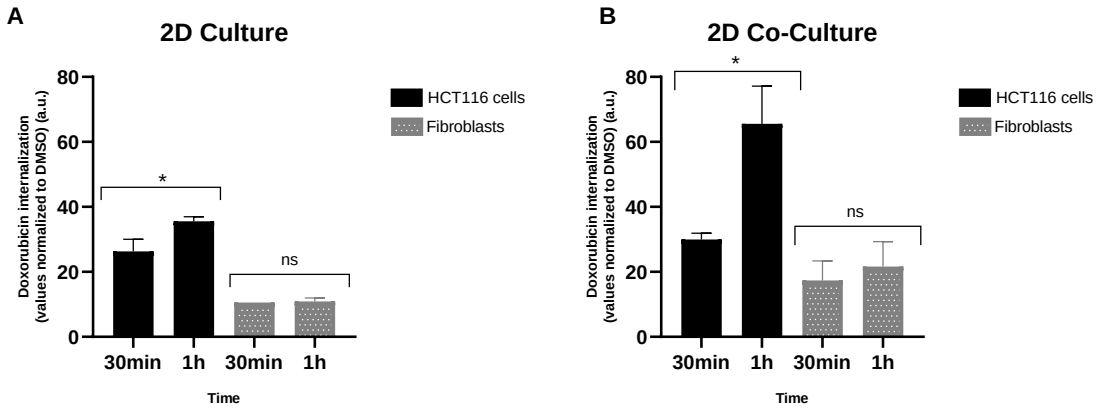

Figure 3.6 Internalization of Doxorubicin normalized to DMSO. (A) HCT116 cells and Fibroblasts in 2D cultures (B) HCT116 cells and Fibroblasts in 2D co-culture (ratio HCT116 cells:Fibroblasts – 1:1). Cells were exposed to 8 µM of Dox for 30min to 1h. * p<0.05; ** p<0.01; *** p<0.001; **** p<0.0001

After 30min and 1h of incubation in the presence of Dox in 2D cultures, HCT116 cells seams to internalize more Dox than fibroblasts (figure 3.7). In comparison, HCT116 cells in co-cultures present a significant increase of Dox internalization after 1h, when compared with fibroblasts (figure 3.7). Nevertheless, the high intensity of Dox signal (saturation of fluorescence) might lead to false results in terms of quantification of the signal.

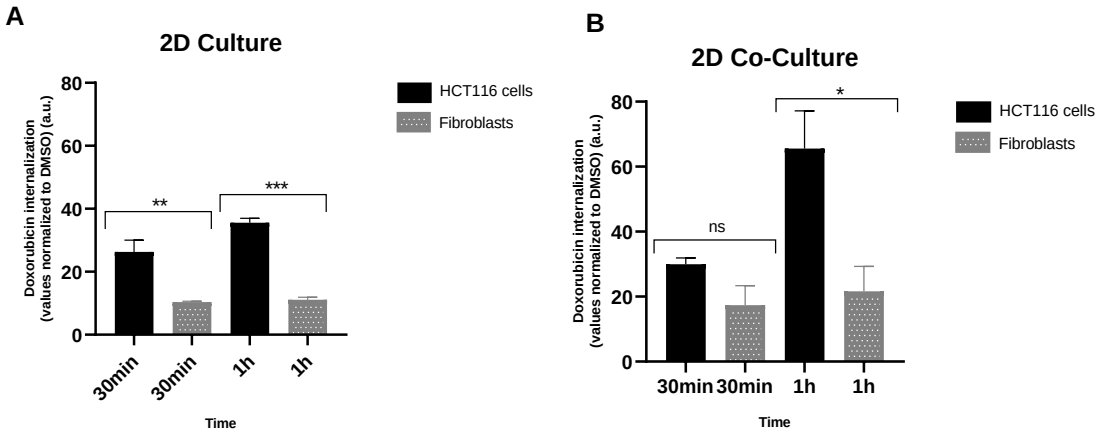

Figure 3.7 Internalization of Doxorubicin normalized to DMSO. (A) HCT116 cells and Fibroblasts in 2D culture (B) HCT116 cells and Fibroblasts in 2D co-culture (ratio HCT116 cells:Fibroblasts – 1:1). Cells were exposed to 8 µM of Dox for 30min to 1h. * p<0.05; ** p<0.01; *** p<0.001; **** p<0.0001

Since HCT116 DoxR cells grow in the presence of 6 µM of Dox (57) we performed the assays in HCT116 DoxR and also again in fibroblasts using this concentration of Dox. As we can observe only some cells show internalization of Dox in 2D cultures probably due to the activated Pgp protein that is responsible for the drug efflux (57) (figures 3.8 and 3.9).

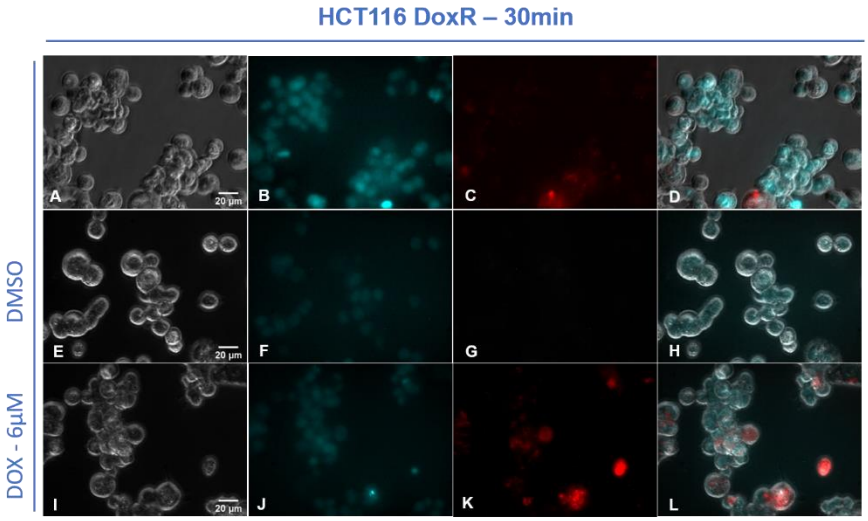

Figure 3.8 Fluorescence microscopy images of 2D cultures of HCT116 DoxR cells after incubation for 30min in the presence or absence of Dox Nucleus are stained with Hoechst (blue). Cells were incubated with 6µM of Dox (red) or 0.1% of DMSO according to the referenced for 30min. (A) Bright field image of HCT116 DoxR cells (B) Image acquired with UV excitation of HCT116 DoxR cells – Nucleus (C) Image acquired with green excitation of HCT116 DoxR cells (D)Combined image of (A), (B) and (C) images (E) Bright field image of HCT116 DoxR cells (F) Image acquired with UV excitation of HCT116 DoxR cells – Nucleus (G) Image acquired with green excitation of HCT116 DoxR cells (H)Combined image of (E), (F) and (G) images (I) Bright field image of HCT116 DoxR cells (J) Image acquired with UV excitation of HCT116 DoxR cells – Nucleus (K) Image acquired with green excitation of HCT116 DoxR cells (L)Combined image of (I), (J) and (K) images. The presented images were treated with ImageJ software.

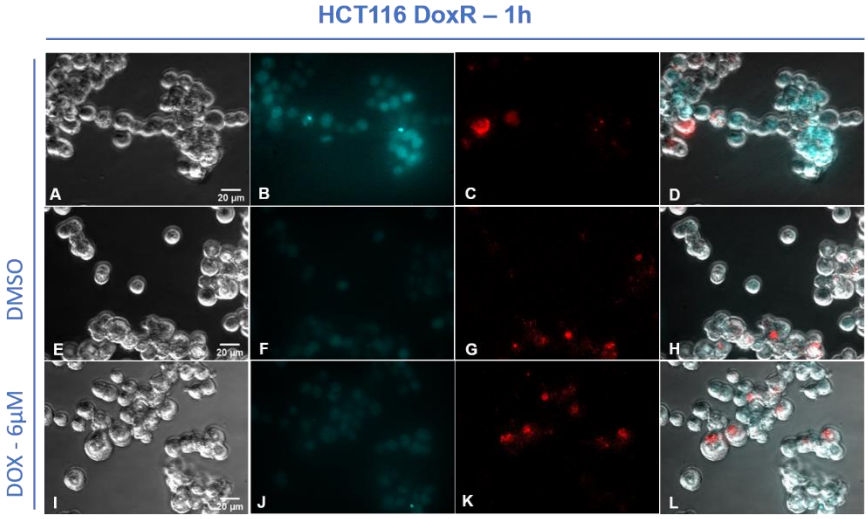

Figure 3.9 Fluorescence microscopy images of 2D cultures HCT116 DoxR cells after incubation for 1h in the presence or absence of Dox. Nucleus are stained with Hoechst (blue). Cells were incubated with 6µM of Dox (red) or 0.1% of DMSO according to the referenced for 1h. (A) Bright field image of HCT116 DoxR cells (B) Image acquired with UV excitation of HCT116 DoxR cells – Nucleus (C) Image acquired with green excitation of HCT116 DoxR cells (D)Combined image of (A), (B) and (C) images (E) Bright field image of HCT116 DoxR cells (F) Image acquired with UV excitation of HCT116 DoxR cells – Nucleus (G) Image acquired with green excitation of HCT116 DoxR cells (H)Combined image of (E), (F) and (G) images (I) Bright field image of HCT116 DoxR cells (J) Image acquired with UV excitation of HCT116 DoxR cells – Nucleus (K) Image acquired with green excitation of HCT116 DoxR cells (L)Combined image of (I), (J) and (K) images. The presented images were treated with ImageJ software.

In fibroblasts the nucleus and the cytoplasm contain Dox, but the presence of Dox increases over time (figures 3.10 and 3.11).

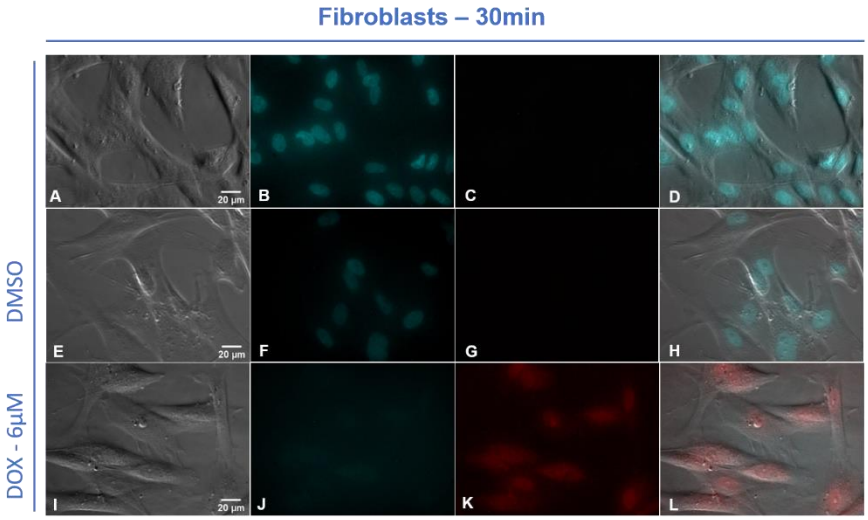

Figure 3.10 Fluorescence microscopy images of 2D culture of primary fibroblasts after incubation for 30min in the presence or absence of Dox. Nucleus are stained with Hoechst (blue). Cells were incubated with 6µM of Dox (red) or 0.1% of DMSO according to the referenced for 30min. (A) Bright field image of primary fibroblasts (B) Image acquired with UV excitation of primary fibroblasts – Nucleus (C) Image acquired with green excitation of primary fibroblasts (D) Combined image of (A), (B) and (C) images (E) Bright field image of primary fibroblasts (F) Image acquired with UV excitation of primary fibroblasts – Nucleus (G) Image acquired with green excitation of primary fibroblasts (H) Combined image of (E), (F) and (G) images (I) Bright field image of primary fibroblasts (J) Image acquired with UV excitation of primary fibroblasts – Nucleus (K) Image acquired with green excitation of primary fibroblasts (L)Combined image of (I), (J) and (K) images. The presented images were treated with ImageJ software.

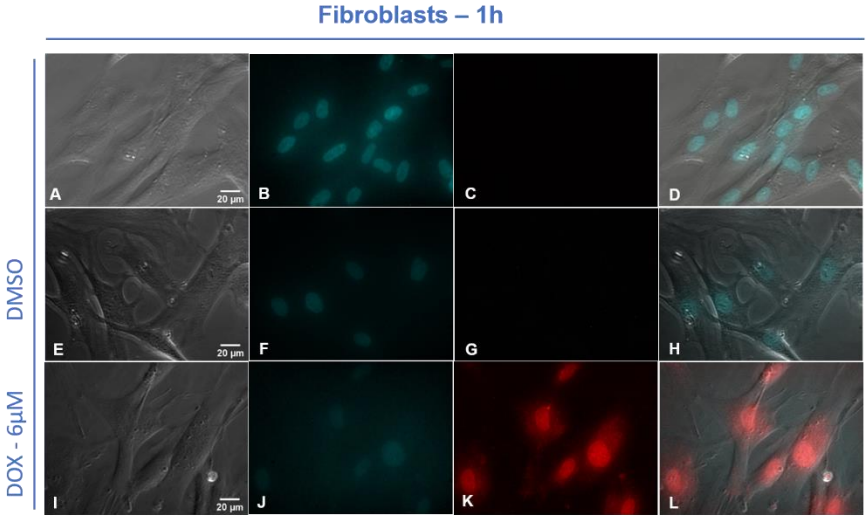

Figure 3.11 Fluorescence microscopy images of 2D cultures of primary fibroblasts after incubation for 1h in the presence or absence of Dox. Nucleus are stained with Hoechst (blue). Cells were incubated with 6µM of Dox (red) or 0.1% of DMSO according to the referenced for 1h. (A) Bright field image of primary fibroblasts (B) Image acquired with UV excitation of primary fibroblasts – Nucleus (C) Image acquired with green excitation of primary fibroblasts (D) Combined image of (A), (B) and (C) images (E) Bright field image of primary fibroblasts (F) Image acquired with UV excitation of primary fibroblasts – Nucleus (G) Image acquired with green excitation of primary fibroblasts (H) Combined image of (E), (F) and (G) images (I) Bright field image of primary fibroblasts (J) Image acquired with UV excitation of primary fibroblasts – Nucleus (K) Image acquired with green excitation of primary fibroblasts (L)Combined image of (I), (J) and (K) images. The presented images were treated with ImageJ software.

When co-cultures of Fibroblasts and HCT116 DoxR were used to access Dox internalization, no significant differences were observed for both time points for HCT116 DoxR cells but a

significant increase in Dox fluorescence was observed in fibroblasts by fluorescence microscopy (figure 3.12) and also by quantification of fluorescence (figure 3.13).

Indeed, quantification of the fluorescence allow to confirm the results describe above for 2D cultures. In 2D cultures, after 30min or 1h of Dox incubation, Fibroblasts internalize more Dox than HCT116 DoxR (figure 3.14). In 2D co-cultures the results are similar but, the difference in Dox internalization after 30min of incubation does not present statistical significance (figure 3.14).

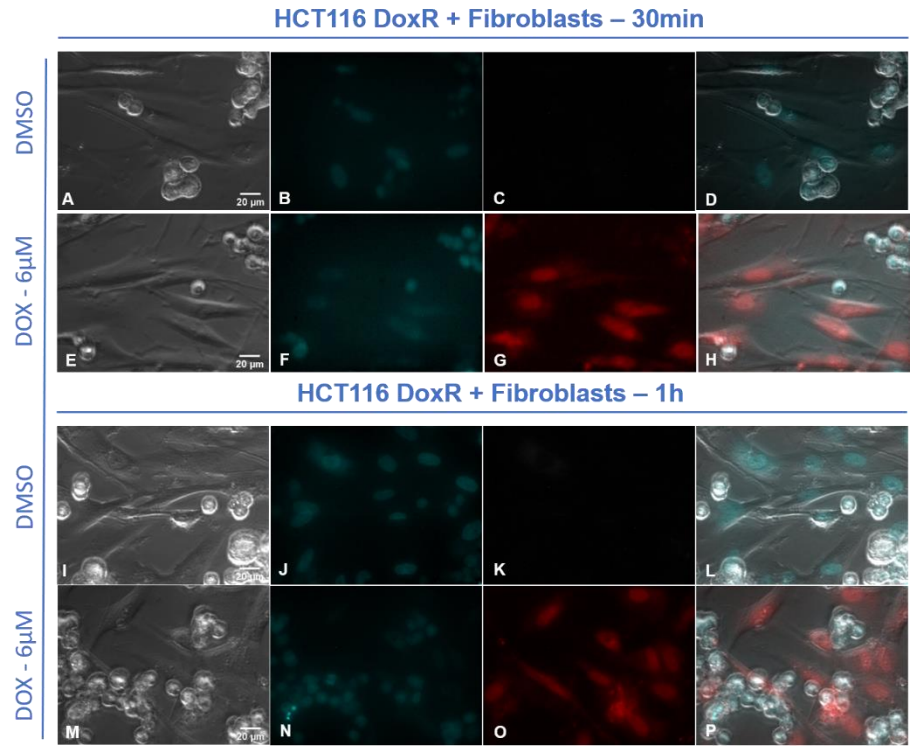

Figure 3.12 Fluorescence microscopy images of 2D co-culture of primary fibroblasts and HCT116 DoxR cells (ratio 1:1). Nucleus are stained with Hoechst (blue). Cells were incubated with 6µM of Dox (red) or 0.1% of DMSO according to the referenced for 30min to 1h. (A) Bright field image (B) Image acquired with UV excitation – Nucleus (C) Image acquired with green excitation (D)Combined image of (A), (B) and (C) images (E) Bright field image (F) Image acquired with UV excitation – Nucleus (G) Image acquired with green excitation (H)Combined image of (E), (F) and (G) images (I) Bright field image (J) Image acquired with UV excitation – Nucleus (K) Image acquired with green excitation (L)Combined image of (I), (J) and (K) images (M) Bright field image (N) Image acquired with UV excitation – Nucleus (O) Image acquired with green excitation (P)Combined image of (M), (N) and (O) images. The presented images were treated with ImageJ software.

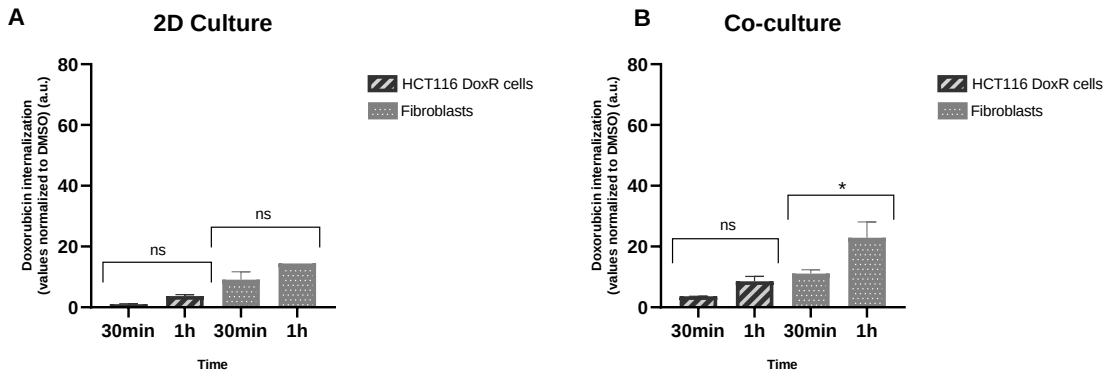

Figure 3.13 Internalization of Doxorubicin normalized to DMSO. (A) HCT116 DoxR cells and Fibroblasts in 2D culture (B) HCT116 DoxR cells and Fibroblasts in 2D co-culture (ratio HCT116 DoxR cells:Fibroblasts – 1:1). Cells were exposed to 6 µM of Dox for 30min to 1h. * p<0.05; ** p<0.01; *** p<0.001; **** p<0.0001

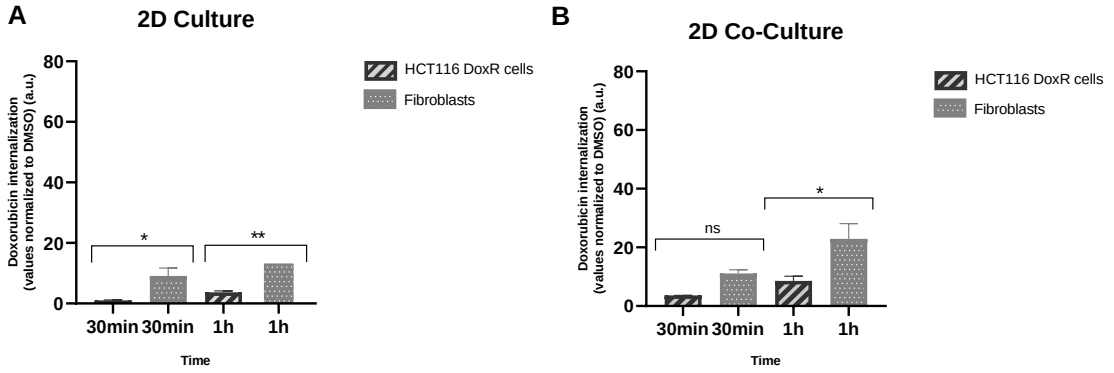

Figure 3.14 Internalization of Doxorubicin normalized to DMSO. (A) HCT116 DoxR cells and Fibroblasts in 2D culture (B) HCT116 DoxR cells and Fibroblasts in 2D co-culture (ratio HCT116 DoxR cells:Fibroblasts – 1:1). Cells were exposed to 6 µM of Dox for 30min to 1h. * p<0.05; ** p<0.01; *** p<0.001; **** p<0.0001

To sum up and considering all the data of fluorescence quantification we can conclude that there is an increase of HCT116 cells fluorescence (as a correlation with Dox internalization) when in 2D co-cultures (figure 3.15).

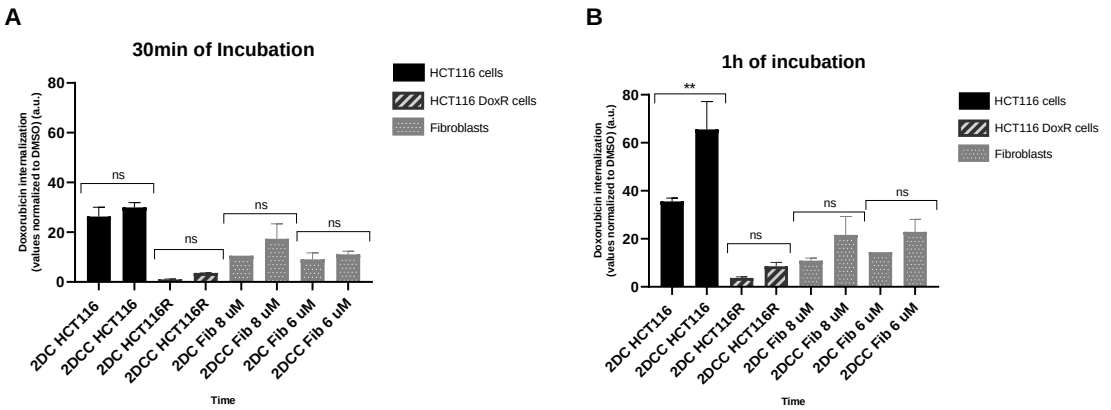

Figure 3.15 Internalization of Doxorubicin normalized to DMSO. (A) HCT116 cells, HCT116 DoxR cells and Fibroblasts in 2D culture (2D C) and 2D co-culture (2D CC) (ratio cancer cells:Fibroblasts – 1:1) exposed to 8 µM (HCT116 cells) or 6 µM (HCT116 DoxR cells) of Dox for 30min (B) HCT116 cells, HCT116 DoxR cells and Fibroblasts in 2D culture (2D C) and 2D co-culture (2D CC) (ratio cancer cells:Fibroblasts – 1:1) exposed

to 8 µM (HCT116 cells) or 6 µM (HCT116 DoxR cells) of Dox for 1h. * p<0.05; ** p<0.01; *** p<0.001; **** p<0.0001

The analyse of these results also suggests that the presence of other cells affects the internalization of Dox in HCT116 after 1h of incubation (figure 3.15). Also as expected, HCT116 cells internalize more Dox than HCT116 DoxR cells (figure 3.15) and this attest the Dox resistance of HCT116 DoxR cells (57).

HCT116 DoxR cells emit fluorescence in the Dox zone. This fluorescence may be due to Dox present in cells as they were cultured with Dox in the medium (figures 3.8, 3.9, 3.12).

Doxorubicin is a DNA intercalating agent (36,37) and Hoechst 33258 is a dye that binds to DNA (60), therefore both have the same target. For this reason, in the presence of Dox, the nucleus staining with Hoechst is not so strong. This lower staining allows to conclude the competing action of Dox and Hoechst for the same target and the presence of Dox in the nucleus.

3.2. Spheroids: Cell Viability

Generally, spheroids growth (figure 3.16 and 3.17) is characterized by a period of one/two days of cell aggregation followed by a period of compression, since the diameter of spheroids does not change significantly (given that the spheroids orientation changes and the diameter is not measured between the same two points). Considering this, we analysed and compared the growth of HCT116 and HCT116 DoxR 3D spheroids (figures 3.16 and 3.17). The results show that HCT116 DoxR spheroids are larger than the HCT116 spheroids (figures 3.16 and 3.17).

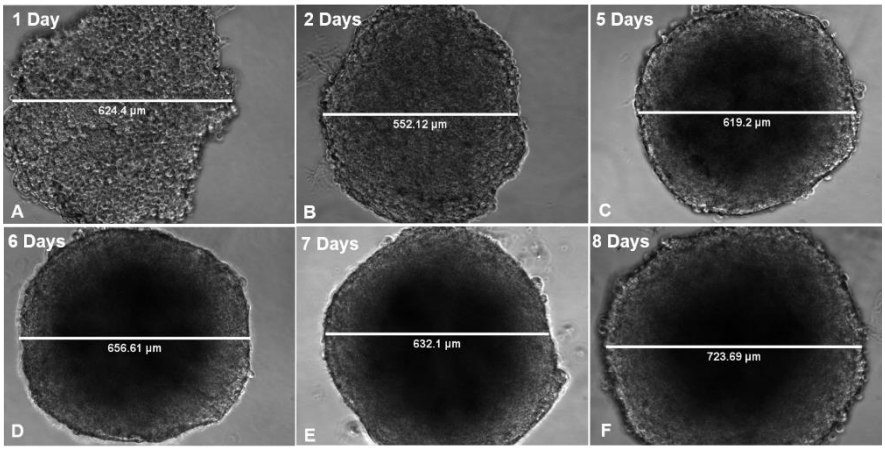

Figure 3.16 Microscopy images of HCT116 spheroid with (A) 1 day and 624.4 µm of diameter (B) 2 days and 552.12 µm of diameter (C) 5 days and 619.2 µm of diameter (D) 6 days and 656.61 µm of diameter (E) 7 days and 632.1 µm of diameter (F) 8 days and 723.69 µm of diameter. The lines in white represents the line used for measuring the diameter. The presented imagens were treated using ImageJ software.

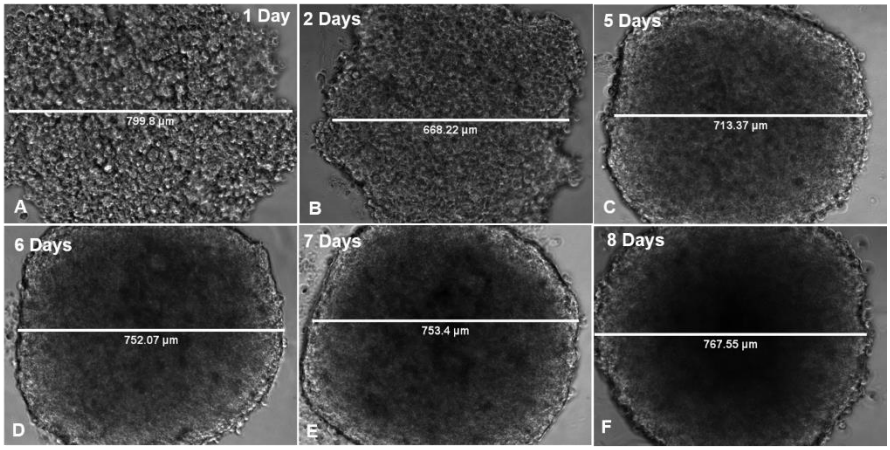

Figure 3.17 Microscopy images of HCT116 DoxR spheroid with (A) 1 day and 799.8 µm of diameter (B) 2 days and 668.22 µm of diameter (C) 5 days and 713.37 µm of diameter (D) 6 days and 752.07 µm of diameter (E) 7 days and 753.4 µm of diameter (F) 8 days and 767.55 µm of diameter. The lines in white represents the line used for measuring the diameter. The presented imagens were treated using ImageJ software.

Once the spheroids have more than 200 µM, it is expected that the three cell layers are formed (29,35), that can be confirmed using hypoxia and/or cell death markers. Considering this, we studied cell viability/death using CellTox Green™ dye in HCT116 3D model. The results show that, over time, there is an increase of cell death in the spheroid core observed by the impairment of cellular membrane via fluorescence microscopy with CellTox Green™ dye (figure 3.18). Green dots in the central region of spheroid are unfocused, this could indicate that dead cells lies inside the spheroid and, consequently, may indicate that this region is the necrotic core (figure 3.18). The necrotic core results from the impairment of nutrients and oxygen supply which is an important characteristic in tumour microenvironment that influences the tumour growth, invasion and therapeutic efficiency (26). These results corroborate that, in HCT116 tumour spheroids, the necrotic core was formed (29).

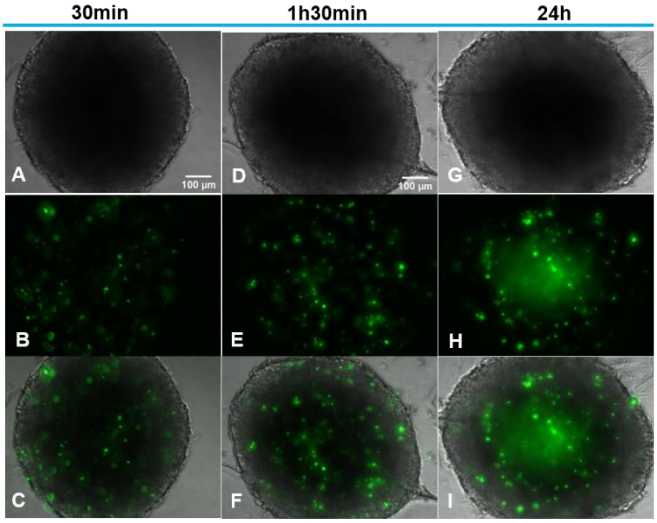

Figure 3.18 Fluorescence microscopy images of HCT116 spheroid with 8 days of growth and incubated with CellTox™ Green dye 1x during 30 min, 1h30min and 24h (A) Bright Field image of spheroids after 30 min of incubation (B) Composite of images acquired with blue excitation after 30 min of incubation. (C) Composite of images A and B. (D) Bright Field image of spheroids after 1h30 min of incubation (E) Composite of images acquired with blue excitation after 1h30 min of incubation. (F) Composite of images D and E. (G) Bright Field image of spheroids after 24h of incubation (H) Composite of images acquired with blue excitation after 24h of incubation. (I) Composite of images G and H. The presented imagens were treated using ImageJ software.

Gold nanoparticles have several characteristics that make them interesting for cancer treatment, diagnosis and theranostic (5). Considering this, next step was to focus on the possible use of AuNPs as drug permeabilization agent (61,62,63) and/or photothermal agent (2,42,56) in 3D models.

As a first approach, HCT116 3D spheroids (after 7 days of growth) were treated with AuNP@PEG for 24h and after this period, incubated with CellTox™ Green dye (figure 3.19). Differently from the untreated spheroids (figure 3.18), the spheroids incubated with AuNP@PEG shows a peripheral circle of green fluorescence associated with membrane compromised cells (figure 3.19). Interestingly, this peripherical circle width increases over time and the bright field images show spheroid disintegration over time (figure 3.19). These results indicate that AuNP@PEG are able to enter the 3D model inducing cell death.

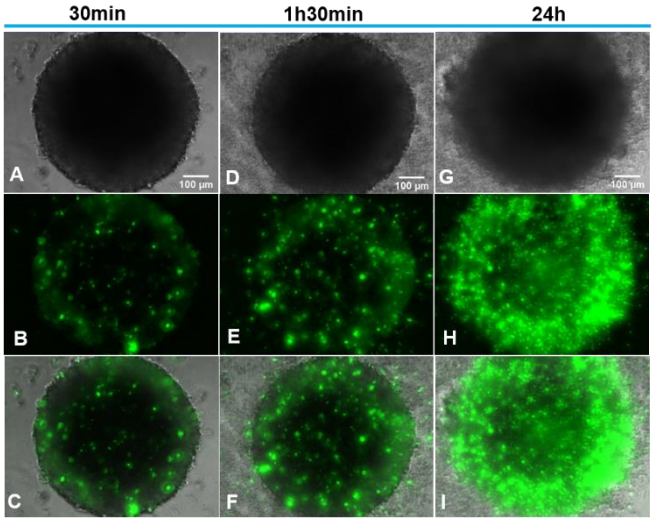

Figure 3.19 Fluorescence microscopy images of HCT116 spheroid with 8 days of growth and incubated with 8 nM of AuNP-PEG (100%) during 24h and, after with CellTox™ Green dye 1x during 30 min, 1h30min and 24h. (A) Bright Field image of spheroids after 30 min of incubation (B) Composite of images acquired with blue excitation after 30 min of incubation. (C) Composite of images A and B. (D) Bright Field image of spheroids after 1h30 min of incubation (E) Composite of images acquired with blue excitation after 1h30 min of incubation. (F) Composite of images D and E. (G) Bright Field image of spheroids after 24h of incubation (H) Composite of images acquired with blue excitation after 24h of incubation. (I) Composite of images G and H. The presented imagens were treated using ImageJ software.

Subsequently, we studied the effect of irradiating the spheroids in the visible. As observed in figure 3.20 the irradiation of HCT116 spheroids induced an increase in cell death/loss of membrane integrity when compared with non-irradiated spheroids (figure 3.18). Interestingly, the fluorescence signal of CellTox™ green dye increases over time, with a strong emission in the central area of the 3D spheroid. This increase fluorescence might be a consequence from the absorption of light by cytochromes, which are capable to convert light in heat, although they have low absorption efficiency (56) and/or due to the fact that cells in the center are under more stress due to lack of oxygen and nutrients (28).

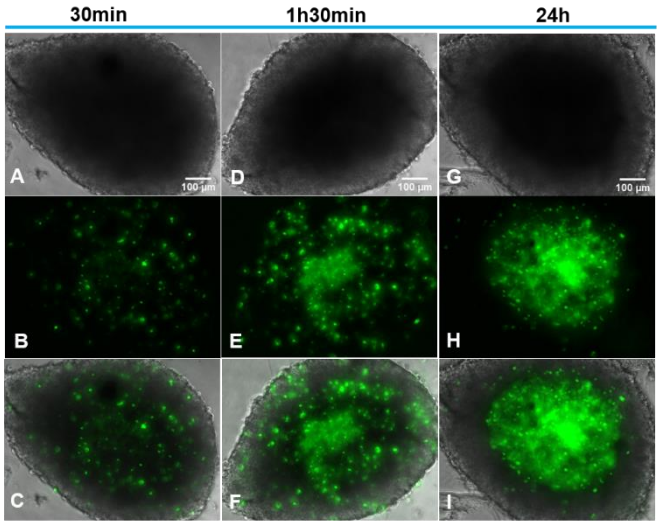

Figure 3.20 Fluorescence microscopy images of HCT116 spheroid with 8 days of growth and irradiated at 532 nm during 1 min and, after irradiation, was incubated with CellTox™ Green dye 1x during 30 min, 1h30min and 24h. (A) Bright Field image of spheroids after 30 min of incubation (B) Composite of images acquired with blue excitation after 30 min of incubation. (C) Composite of images A and B. (D) Bright Field image of spheroids after 1h30 min of incubation (E) Composite of images acquired with blue excitation after 1h30 min of incubation. (F) Composite of images D and E. (G) Bright Field image of spheroids after 24h of incubation (H) Composite of images acquired with blue excitation after 24h of incubation. (I) Composite of images G and H. The presented imagens were treated using ImageJ software.

We next combined the effect of AuNP@PEG with irradiation in order to see if we could potentiate each individual effect. The images of spheroids irradiated after AuNP@PEG treatment (figure 3.21) allows the observation of two circles with high green fluorescence, one at the periphery of the spheroid and the other in the central part of the spheroid. This effect was observed 30mins after irradiation and increased over time (figure 3.21) which indicates that the nanoparticles were able to induce hyperthermia leading to an increase of cell death. Bright field images show a slight disintegration of the spheroid (figure 3.21).

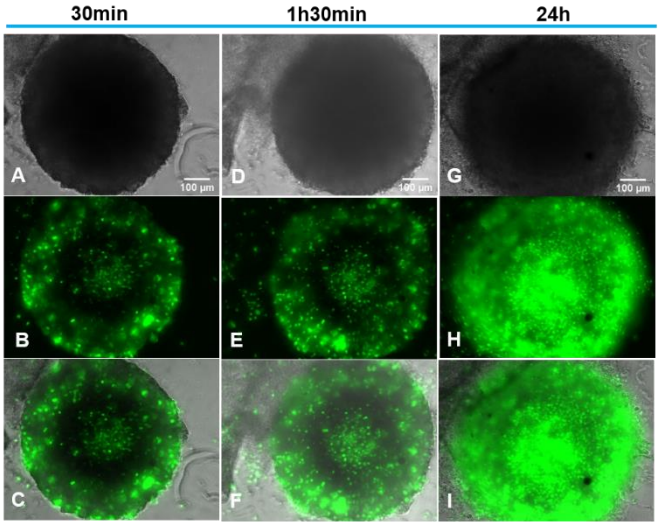

Figure 3.21 Fluorescence microscopy images of HCT116 spheroid with 8 days of growth and incubated with 8 nM of AuNP-PEG (100%) during 24h and, after irradiated at 532 nm for 1 min and, incubated with CellTox™ Green dye 1x during 30 min, 1h30min and 24h. (A) Bright Field image of spheroids after 30 min of incubation (B) Composite of images acquired with blue excitation after 30 min of incubation. (C) Composite of images A and B. (D) Bright Field image of spheroids after 1h30 min of incubation (E) Composite of images acquired with blue excitation after 1h30 min of incubation. (F) Composite of images D and E. (G) Bright Field image

of spheroids after 24h of incubation (H) Composite of images acquired with blue excitation after 24h of incubation. (I) Composite of images G and H. The presented imagens were treated using ImageJ software.

Considering these very promising results with the colorectal carcinoma cell line (HCT116), we performed the same type of experiments in the HCT116 DoxR spheroids.

First, we analysed the pattern of cell death in the 3D model after 8 days of growth by incubating the spheroids with CellTox™ Green for 30 min, 1h30min and 24h (figure 3.22). Compared to HCT116 spheroids (figure 3.18) there seems to be an increased cell death with time, in HCT116 DoxR spheroids (figure 3.22). The CellTox™ Green signal comes up more localized in the internal (unfocused green dots) and external (focused green dots) central region. The spheroid core appears to be most necrotic zone (figure 3.22).

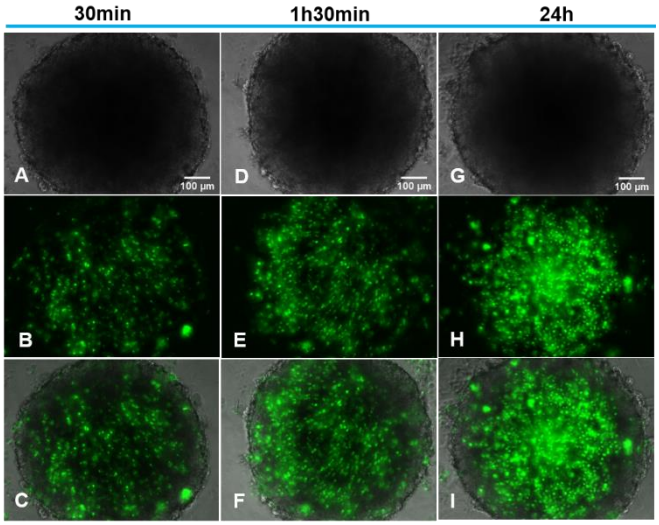

Figure 3.22 Fluorescence microscopy images of Dox resistant HCT116 spheroid with 8 days of growth and incubated with CellTox™ Green dye 1x during 30 min, 1h30min and 24h (A) Bright Field image of spheroids after 30 min of incubation (B) Composite of images acquired with blue excitation after 30 min of incubation. (C) Composite of images A and B. (D) Bright Field image of spheroids after 1h30 min of incubation (E) Composite of images acquired with blue excitation after 1h30 min of incubation. (F) Composite of images D and E. (G) Bright Field image of spheroids after 24h of incubation (H) Composite of images acquired with blue excitation after 24h of incubation. (I) Composite of images G and H. The presented imagens were treated using ImageJ software.

When HCT116 DoxR spheroids were incubated with AuNP@PEG we can observed an increase in the fluorescence particularly close to the center of the spheroid (figure 3.23). At 24h it is possible to observe two concentric regions with increase fluorescence (figure 3.23). The bright field image show, over time, spheroid disintegration. These results are identical to those observed in HCT116 spheroids (figure 3.19), however, the fluorescent level seems to be slightly lower for the HCT116 DoxR spheroids (figure 3.23).

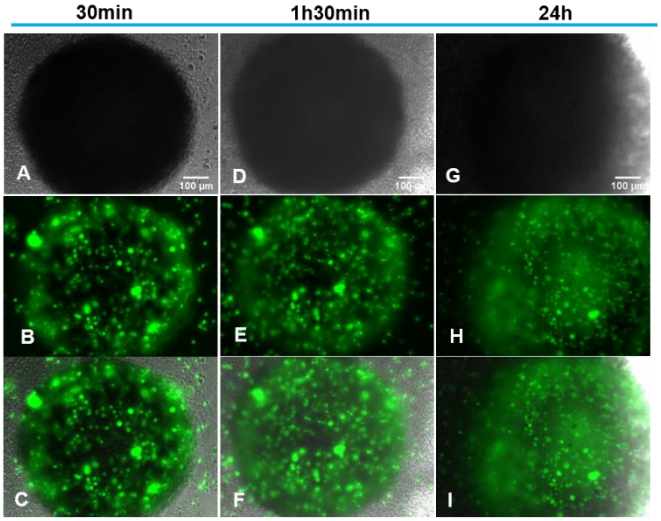

Figure 3.23 Fluorescence microscopy images of Dox resistant HCT116 spheroid with 8 days of growth and incubated with 8 nM of AuNP-PEG (100%) during 24h and, incubated with CellTox™ Green dye 1x during 30 min, 1h30min and 24h. (A) Bright Field image of spheroids after 30 min of incubation (B) Composite of images acquired with blue excitation after 30 min of incubation. (C) Composite of images A and B. (D) Bright Field image of spheroids after 1h30 min of incubation (E) Composite of images acquired with blue excitation after 1h30 min of incubation. (F) Composite of images D and E. (G) Bright Field image of spheroids after 24h of incubation (H) Composite of images acquired with blue excitation after 24h of incubation. (I) Composite of images G and H. The presented imagens were treated using ImageJ software.

Irradiation of HCT116 DoxR spheroids shows an increase of cell death/loss membrane integrity over time particularly at the central area of the 3D model, as also observed for HCT116 spheroids (figures 3.20 and 3.24).

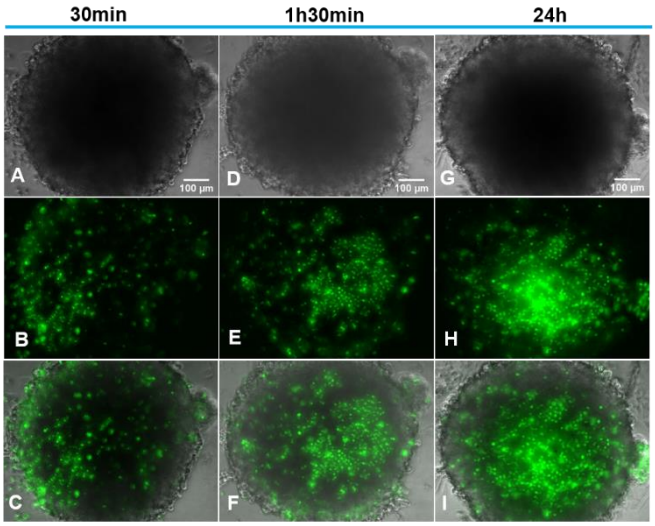

Figure 3.24 Fluorescence microscopy images of Dox resistant HCT116 spheroid with 8 days of growth and irradiated at 532 nm during 1 min and, after incubated with CellTox™ Green dye 1x during 30 min, 1h30min and 24h. (A) Bright Field image of spheroids after 30 min of incubation (B) Composite of images acquired with blue excitation after 30 min of incubation. (C) Composite of images A and B. (D) Bright Field image of spheroids after 1h30 min of incubation (E) Composite of images acquired with blue excitation after 1h30 min of incubation. (F) Composite of images D and E. (G) Bright Field image of spheroids after 24h of incubation (H) Composite of images acquired with blue excitation after 24h of incubation. (I) Composite of images G and H. The presented imagens were treated using ImageJ software.

Combination of AuNP@PEG and irradiation in HCT116 DoxR spheroids leads to an increase of fluorescence (cell death) over time when compared to the untreated spheroids (figures 3.22 and 3.25). These results also show that, after 24h of CellTox™ Green dye incubation, the signal

is no longer located on the periphery and is scattered throughout the spheroid. The bright field image show spheroid disintegration over time.

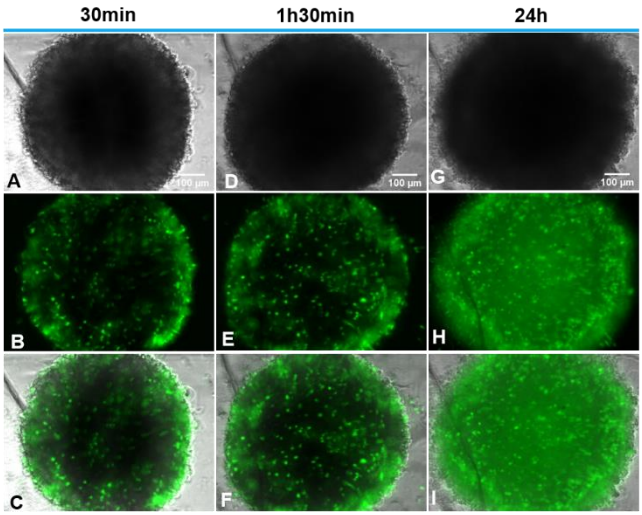

Figure 3.25 Fluorescence microscopy images of Dox resistant HCT116 spheroid with 8 days of growth and incubated with 8 nM of AuNP-PEG (100%) during 24h and, after irradiated at 532 nm during 1 min and, incubated with CellTox™ Green dye 1x during 30 min, 1h30min and 24h. (A) Bright Field image of spheroids after 30 min of incubation (B) Composite of images acquired with blue excitation after 30 min of incubation. (C) Composite of images A and B. (D) Bright Field image of spheroids after 1h30 min of incubation (E) Composite of images acquired with blue excitation after 1h30 min of incubation. (F) Composite of images D and E. (G) Bright Field image of spheroids after 24h of incubation (H) Composite of images acquired with blue excitation after 24h of incubation. (I) Composite of images G and H. The presented imagens were treated using ImageJ software.

The use of AuNP@PEG seems to influence the cell viability/membrane integrity in both HCT116 and HCT116 DoxR spheroids (figures 3.19 and 3.23) and, in combination with irradiation, the effect is more evident (figures 3.21 and 3.25). AuNP@PEG also influences the structure of spheroids once the HCT116 spheroids and HCT116 DoxR spheroids present spheroid disintegration. Irradiation of HCT116 spheroids without any previous treatment (figure 3.20) shows considerable different results compared to control HCT116 spheroids (figure 3.18) and this result is important in the therapeutic area because it results from the cells' natural response to irradiation (figure 3.20). HCT116 DoxR spheroids seems to be more resistant to AuNP@PEG treatment that the HCT116 spheroids (figures 3.19 versus 3.23 and figures 3.21 versus 3.25).

The CellTox™ Green dye allows the identification of cells with impairment of cellular membrane. The loss of membrane integrity is a feature of later stages of apoptosis and particularly necrosis cell death (58). Studies with gold nanoparticles show that these nanoparticles can be responsible, after laser irradiation, for an increase of local temperature (2,42,56) and cell permeabilization (61,62,63). The results of this work show an increase of impairment of cell membrane after AuNP@PEG treatment with and without irradiation with a higher increase in the presence of irradiation.

3.3. Doxorubicin Diffusion

Gold nanoparticles have been associated with cell permeabilization after irradiation (61,62,63) and it is known that doxorubicin (Dox) is one of the most common chemotherapeutic agent and absorbs in the green region (appendix A) (64). Considering these facts, the previous results lead to the study of gold nanoparticles combined with Dox and submitted and not submitted to irradiation. So, in the present work, it will be analysed the influence of Dox diffusion when: 1) spheroids are treated with AuNP@PEG before Dox incubation; 2) spheroids are irradiated before Dox incubation; 3) AuNP@PEG and irradiation are applied before Dox incubation; 4) spheroids are irradiated after Dox incubation; 5) spheroids are irradiated after AuNP@PEG and Dox incubation.

Naturally, in HCT116 spheroids Dox diffuses over time and accumulates specifically in the periphery but is also present throughout the spheroid in small quantities (figure 3.26). This result indicates that Dox does not diffuse easily throughout the spheroid presenting a lower red staining in the spheroid core.

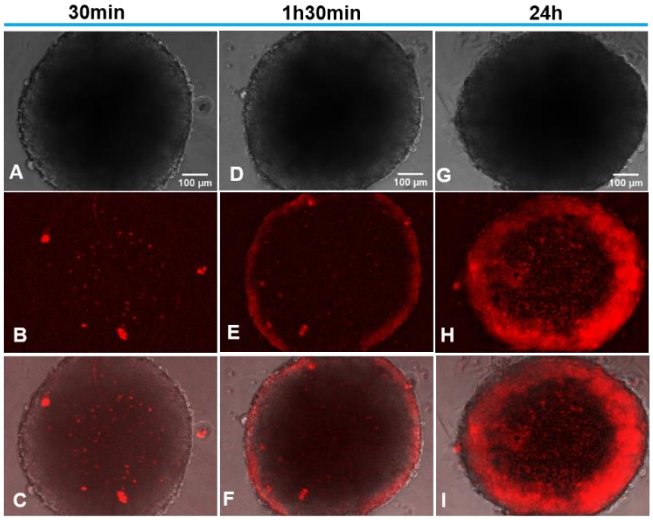

Figure 3.26 Fluorescence microscopy images of a HCT116 spheroid with 8 days of growth and incubated with Dox 8 µM during 30 min, 1h30min or 24h (A) Bright Field image of spheroids after 30 min of incubation (B) Composite of images acquired with green excitation after 30 min of incubation. (C) Composite of images A and B (D) Bright Field image of spheroids after 1h30 min of incubation (E) Composite of images acquired with green excitation after 1h30 min of incubation. (F) Composite of images D and E (G) Bright Field image of spheroids after 24h of incubation (H) Composite of images acquired with green excitation after 24h of incubation. (I) Composite of images G and H The presented imagens were treated using ImageJ software.

The cell viability assay in AuNP@PEG treated HCT116 spheroids (figure 3.19) showed results that raises the possibility that AuNP@PEG may facilitated the diffusion of Dox. To conclude about this possibility HCT116 spheroids were treat with AuNP@PEG before Dox incubation. The results show that Dox diffuse more easily after AuNP@PEG treatment (figure 3.27) compared to the spheroids without the gold nanoparticles treatment (figure 3.26) which confirms the aforementioned possibility. It is showed that AuNP@PEG, allowed a better diffusion of Dox once the accumulation of Dox is more internalized, although it is still observed a small

accumulation in the spheroid periphery (figure 3.27). Bright field images show (figure 3.27), over time, spheroid disintegration that is also visible in the incubation of CellTox Green™ dye after AuNP@PEG treatment (figure 3.19).

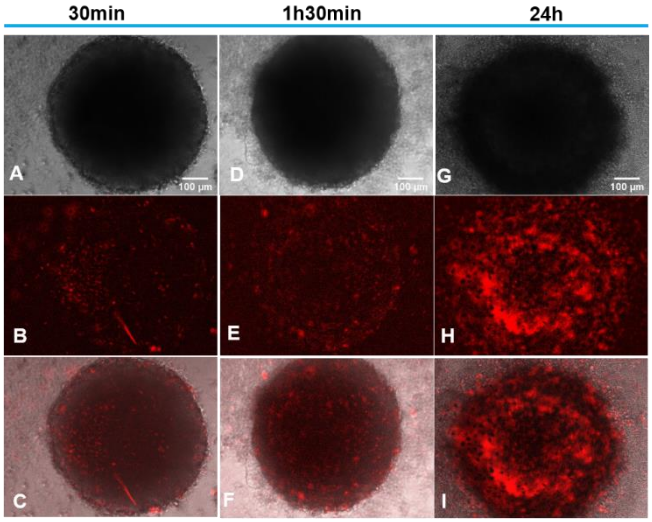

Figure 3.27 Fluorescence microscopy images HCT116 spheroid with 8 days of growth and incubated with 8 nM of AuNP-PEG (100%) during 24h and, after with Dox 8 µM during 30 min, 1h30min or 24h. (A) Bright Field image of spheroids after 30 min of incubation (B) Composite of images acquired with green excitation after 30 min of incubation. (C) Composite of images A and B (D) Bright Field image of spheroids after 1h30 min of incubation (E) Composite of images acquired with green excitation after 1h30 min of incubation. (F) Composite of images D and E (G) Bright Field image of spheroids after 24h of incubation (H) Composite of images acquired with green excitation after 24h of incubation. (I) Composite of images G and H The presented imagens were treated using ImageJ software.

Next, the effect of irradiating the spheroids in the visible before Dox incubation was studied. The results (figure 3.28) do not show significative visual alterations in comparison with the study of Dox diffusion without previous treatment (figure 3.26). Dox diffuses over time and accumulates, after 24h of incubation and irradiation, in the periphery (figure 3.28).

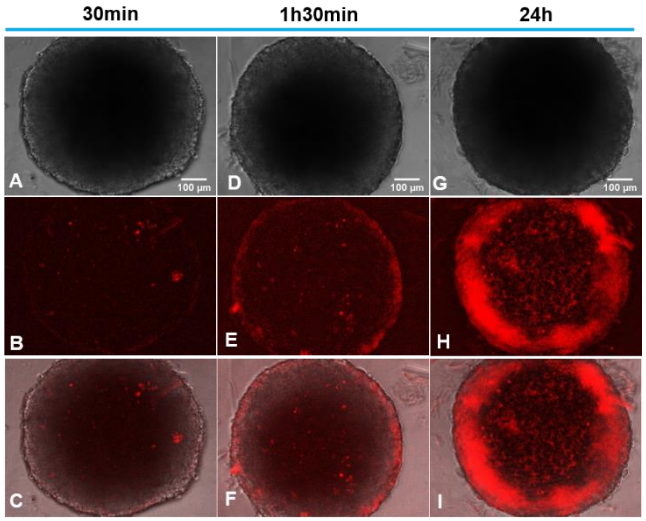

Figure 3.28 Fluorescence microscopy images of HCT116 spheroid with 8 days of growth and irradiated at 532 nm during 1 min and incubated with Dox 8 µM during 30 min, 1h30 min and 24h of incubation. (A) Bright Field image of spheroids after 30 min of incubation (B) Composite of images acquired with green excitation after 30 min of incubation. (C) Composite of images A and B (D) Bright Field image of spheroids after 1h30 min of incubation (E) Composite of images acquired with green excitation after 1h30 min of incubation. (F) Composite of images D and E (G) Bright Field image of spheroids after 24h of incubation (H) Composite of

images acquired with green excitation after 24h of incubation. (I) Composite of images G and H The presented imagens were treated using ImageJ software.

Subsequently, the effect of irradiation in visible combined with AuNP@PEG treatment in Dox diffusion was tested. The spheroids irradiated after AuNP@PEG treatment and before Dox incubation (figure 3.29) shows the same pattern than the spheroids incubated with Dox after AuNP@PEG treatment (figure 3.27), this is Dox accumulates in an intermediate area but is more widespread. Such as in AuNP@PEG-treated spheroids (figure 3.27), morphological chances are visible in the results of this study and spheroids show disintegration (figure 3.29).

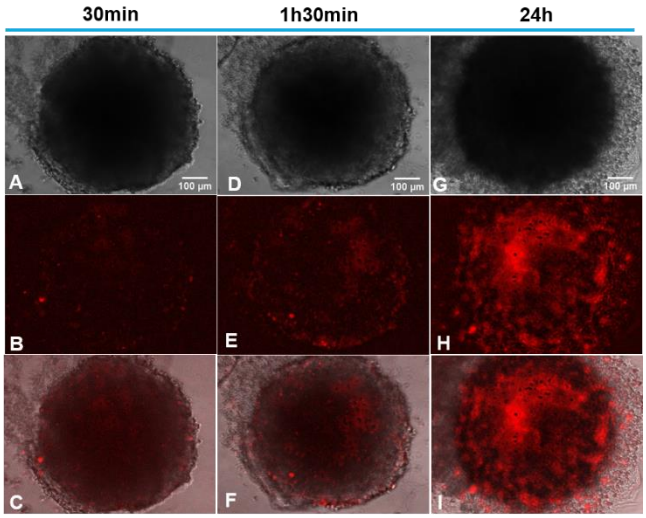

Figure 3.29 Fluorescence microscopy images of HCT116 spheroid with 8 days of growth and incubated with 8 nM of AuNP-PEG (100%) during 24h and, after irradiated at 532 nm for 1 min and incubated with Dox 8 µM during 30 min, 1h30 min and 24h of incubation after irradiation. The spheroid was visualized after 30 min, 1h30 min and 24H of incubation. (A) Bright Field image of spheroids after 30 min of incubation (B) Composite of images acquired with green excitation after 30 min of incubation. (C) Composite of images A and B (D) Bright Field image of spheroids after 1h30 min of incubation (E) Composite of images acquired with green excitation after 1h30 min of incubation. (F) Composite of images D and E (G) Bright Field image of spheroids after 24h of incubation (H) Composite of images acquired with green excitation after 24h of incubation. (I) Composite of images G and H The presented imagens were treated using ImageJ software.

Following, to analyse the influences of irradiation in the diffusion of Dox already present in the spheroid, spheroids were irritated after Dox treatment. The results (figure 3.30) show an initial phase similar to the last phase of spheroids incubated with Dox without other treatment (figure 3.26). Dox, initially, accumulates in the periphery and gradually diffuses and spreads throughout the spheroid reaching the entire structure (figure 3.30).

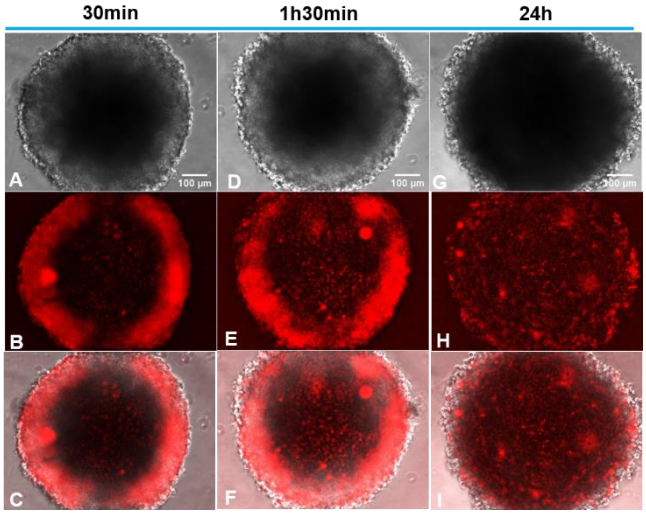

Figure 3.30 Fluorescence microscopy images of HCT116 spheroid with 8 days of growth and irradiated at 532 nm for 1 min after incubation Dox 8 µM for 6h. The spheroid was visualized after 30 min, 1h30 min and 24h of incubation. (A) Bright Field image of spheroids after 30 min of incubation (B) Composite of images acquired with green excitation after 30 min of incubation. (C) Composite of images A and B (D) Bright Field image of spheroids after 1h30 min of incubation (E) Composite of images acquired with green excitation after 1h30 min of incubation. (F) Composite of images D and E (G) Bright Field image of spheroids after 24h of incubation (H) Composite of images acquired with green excitation after 24h of incubation. (I) Composite of images G and H The presented imagens were treated using ImageJ software.

Finally, the influence of irradiation in the visible when the spheroids were previously treated with AuNP@PEG and Dox was also studied and the results (figure 3.31) show an increase of Dox diffusion compared to spheroids not treated with AuNP@PEG (figure 3.26) and diffuses throughout the spheroid. This diffusion is visible since the first time point and Dox seems to reach the core of the spheroid (figure 3.31).

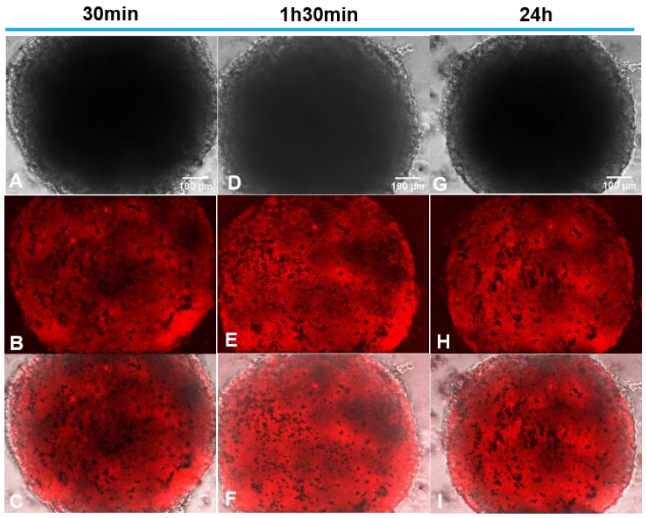

Figure 3.31 Fluorescence microscopy images of HCT116 spheroid with 8 days of growth and irradiated at 532 nm for 1 min after incubation with 8 nM of AuNP-PEG (100%) during 24h and with Dox 8 µM for 6h. The spheroid was visualized after 30 min, 1h30 min and 24h of incubation. (A) Bright Field image of spheroids after 30 min of incubation (B) Composite of images acquired with green excitation after 30 min of incubation. (C) Composite of images A and B (D) Bright Field image of spheroids after 1h30 min of incubation (E) Composite of images acquired with green excitation after 1h30 min of incubation. (F) Composite of images D and E (G) Bright Field image of spheroids after 24h of incubation (H) Composite of images acquired with green excitation after 24h of incubation. (I) Composite of images G and H The presented imagens were treated using ImageJ software.

These results suggest that gold nanoparticles, with and without irradiation (figures 3.26, 3.27, 3.29 and 3.31), influence the diffusion of doxorubicin even in the absence of irradiation. Irradiation with and without previous AuNP@PEG treatment does not lead to alterations in Dox diffusion (figures 3.26, 3.28 and 3.29). On the other hand, irradiation with previous Dox treatment with and without a priori AuNP@PEG treatment (figures 3.30 and 3.31) makes a real difference in Dox diffusion. The treatment with AuNP@PEG and Dox before irradiation is the most promising strategy for the combination of therapies (figure 3.31).

Doxorubicin is an ionizable drug and its distribution and accumulation in the tumour is influenced by the acidic and hypoxic environment of the tumours. This also occurs in spheroids (65). The results of Dox diffusion in HCT116 spheroids corroborates the expected and described in the literature, Dox accumulates in the outer layers of the spheroid and do not reach the middle zone or the core (figure 3.26) (65).

Acquisition of Dox resistance is a recurring problem (35), which makes interesting study the behaviour of HCT116 DoxR spheroids when subjected to the same strategies as HCT116 spheroids. Then, HCT116 DoxR spheroids were subjected to the different treatments and incubated with two different Dox concentrations, 6 µM and 120 µM. The HCT116 DoxR spheroids incubated with 6 µM of Dox (figure 3.32) present an increase of Dox diffusion over time without visible local accumulation. In the HCT116 DoxR spheroids incubated with 120 µM of Dox (figure 3.33) the diffusion of Dox, in the first time points, is similar to the Dox diffusion in spheroids incubated with 6 µM (figure 3.32). However, after 24h of incubation with 120 µM of Dox, Dox accumulates in the intermediate and peripheral zones (figure 3.33).

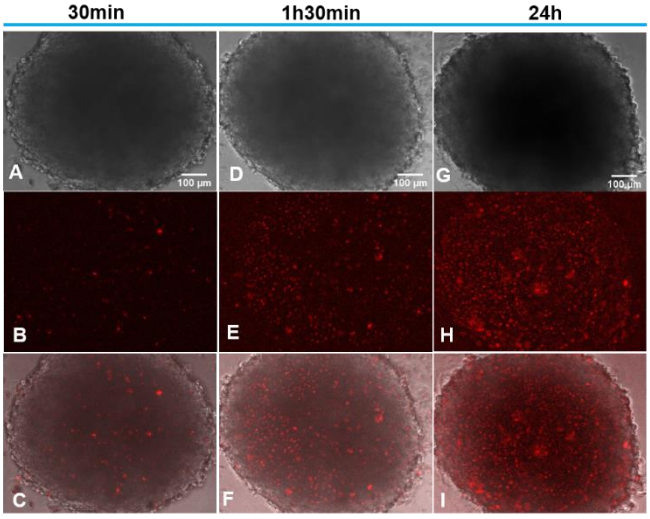

Figure 3.32 Fluorescence microscopy images of Dox resistant HCT116 spheroid with 8 days of and incubated with Dox 6 µM during 30 min, 1h30min or 24h (A) Bright Field image of spheroids after 30 min of incubation (B) Composite of images acquired with green excitation after 30 min of incubation. (C) Composite of images A and B (D) Bright Field image of spheroids after 1h30 min of incubation (E) Composite of images acquired with green excitation after 1h30 min of incubation. (F) Composite of images D and E (G) Bright Field image of spheroids after 24h of incubation (H) Composite of images acquired with green excitation after 24h of incubation. (I) Composite of images G and H The presented imagens were treated using ImageJ software.

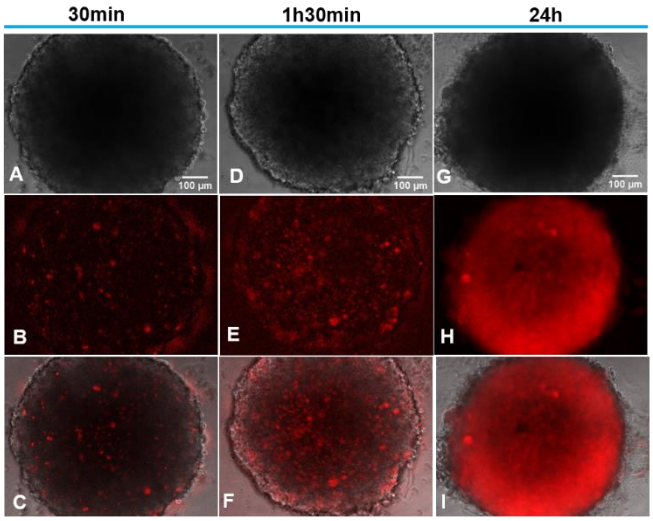

Figure 3.33 Fluorescence microscopy images of Dox resistant HCT116 spheroid with 8 days of growth and incubated with Dox 120 µM during 30 min, 1h30min or 24h (A) Bright Field image of spheroids after 30 min of incubation (B) Composite of images acquired with green excitation after 30 min of incubation. (C) Composite of images A and B (D) Bright Field image of spheroids after 1h30 min of incubation (E) Composite of images acquired with green excitation after 1h30 min of incubation. (F) Composite of images D and E (G) Bright Field image of spheroids after 24h of incubation (H) Composite of images acquired with green excitation after 24h of incubation. (I) Composite of images G and H The presented imagens were treated using Imagej software.

Similar to the first approach with AuNP@PEG, HCT116 DoxR spheroids were treated with AuNP@PEG for 24h and after this period of time, incubated with Dox. The results of HCT116 DoxR spheroids incubated with 6 µM of Dox (figure 3.34) reveal an increase of Dox diffusion over time and an aggregation of Dox. The same pattern occurs in the incubation of 120 µM of Dox with more Dox internalized in the spheroid (figure 3.35). In both cases, bright images in figure show spheroids disintegration (figures 3.34 and 3.35).

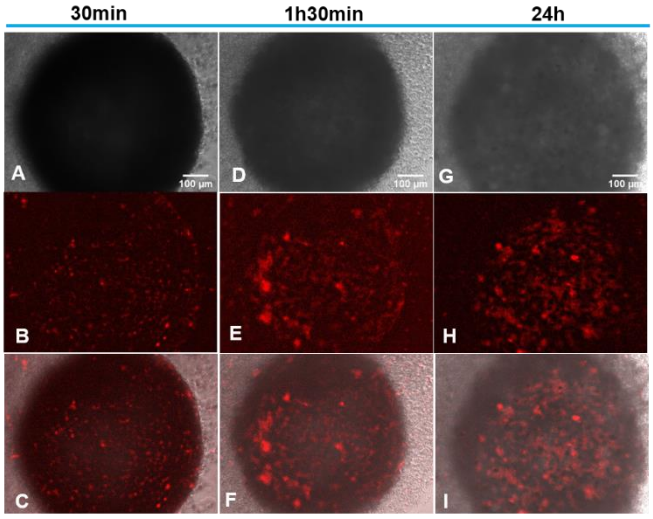

Figure 3.34 Fluorescence microscopy images of Dox resistant HCT116 spheroid with 8 days of growth and incubated with 8 nM of AuNP-PEG (100%) during 24h and, after s incubated with Dox 6 µM during 30 min, 1h30min or 24h. (A) Bright Field image of spheroids after 30 min of incubation (B) Composite of images acquired with green excitation after 30 min of incubation. (C) Composite of images A and B (D) Bright Field image of spheroids after 1h30 min of incubation (E) Composite of images acquired with green excitation after 1h30 min of incubation. (F) Composite of images D and E (G) Bright Field image of spheroids after 24h of incubation (H) Composite of images acquired with green excitation after 24h of incubation. (I) Composite of images G and H The presented imagens were treated using ImageJ software.

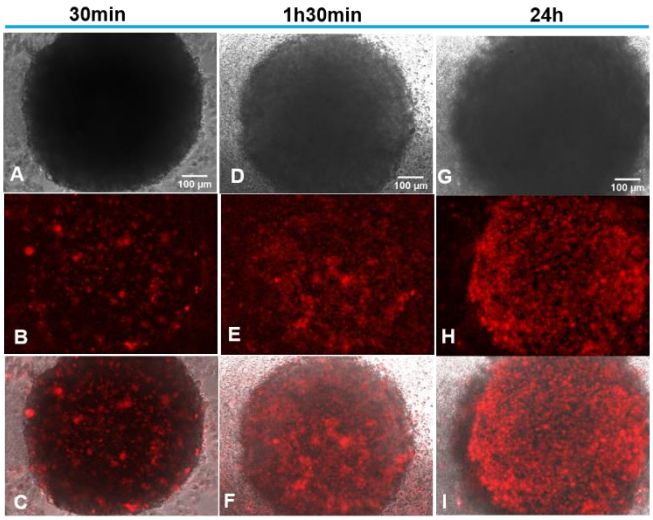

Figure 3.35 Fluorescence microscopy images of Dox resistant HCT116 spheroid with 8 days of growth and incubated with 8 nM of AuNP-PEG (100%) during 24h and, after incubated with Dox 120 µM during 30 min, 1h30min or 24h. (A) Bright Field image of spheroids after 30 min of incubation (B) Composite of images acquired with green excitation after 30 min of incubation. (C) Composite of images A and B (D) Bright Field image of spheroids after 1h30 min of incubation (E) Composite of images acquired with green excitation after 1h30 min of incubation. (F) Composite of images D and E (G) Bright Field image of spheroids after 24h of incubation (H) Composite of images acquired with green excitation after 24h of incubation. (I) Composite of images G and H The presented imagens were treated using ImageJ software.

Irradiation of HCT116 DoxR spheroids in the visible was studied in order to evaluate its influence in Dox diffusion, for that two different concentrations of Dox were used. The irradiation of HCT116 DoxR spheroids followed by incubation with 6 µM of Dox (figure 3.36) do not show alterations in Dox diffusion compared with HCT116 DoxR spheroids having the same incubation parameters but without irradiation (figure 3.32). Diffusion occurs over time and without accumulation or aggregation of Dox (figure 3.36). HCT116 DoxR spheroids irradiated before incubation with 120 µM of Dox (figure 3.37) follows the same pattern of exposure to the same Dox concentration without irradiation (figure 3.33), but with a more prominent accumulation.

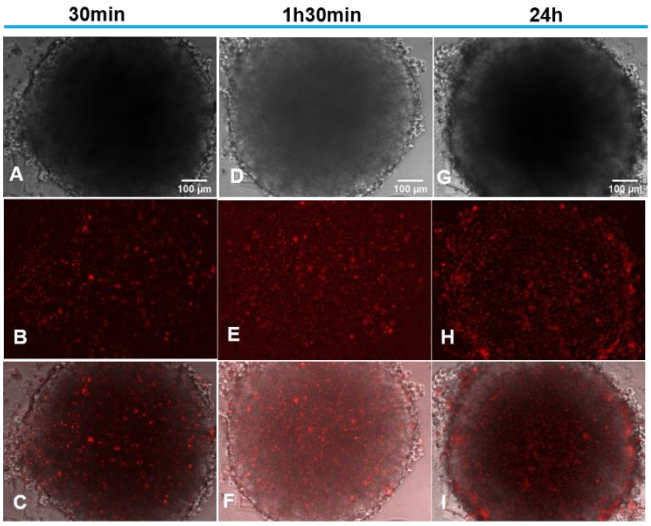

Figure 3.36 Fluorescence microscopy images of Dox resistant HCT116 spheroid with 8 days of growth and irradiated at 532 nm for 1 min and incubated with Dox 6 µM during 30 min, 1h30 min and 24h of incubation. (A) Bright Field image of spheroids after 30 min of incubation (B) Composite of images acquired with green excitation after 30 min of incubation. (C) Composite of images A and B (D) Bright Field image of spheroids

after 1h30 min of incubation (E) Composite of images acquired with green excitation after 1h30 min of incubation. (F) Composite of images D and E (G) Bright Field image of spheroids after 24h of incubation (H) Composite of images acquired with green excitation after 24h of incubation. (I) Composite of images G and H The presented imagens were treated using ImageJ software.

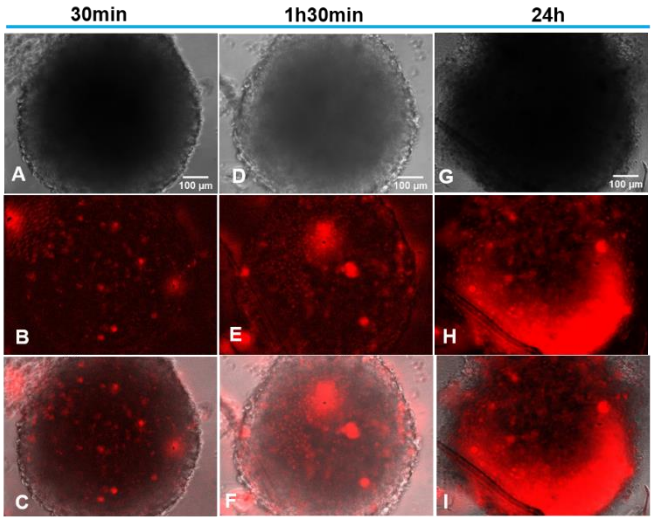

Figure 3.37 Fluorescence microscopy images of Dox resistant HCT116 spheroid with 8 days of growth and was irradiated at 532 nm for 1 min and incubated with Dox 120 µM during 30 min, 1h30 min and 24h of incubation. (A) Bright Field image of spheroids after 30 min of incubation (B) Composite of images acquired with green excitation after 30 min of incubation. (C) Composite of images A and B (D) Bright Field image of spheroids after 1h30 min of incubation (E) Composite of images acquired with green excitation after 1h30 min of incubation. (F) Composite of images D and E (G) Bright Field image of spheroids after 24h of incubation (H) Composite of images acquired with green excitation after 24h of incubation. (I) Composite of images G and H The presented imagens were treated using ImageJ software.

When cells were irradiated after incubation in the presence of 6 µM Dox we can observe a diffusion in all HCT116 DoxR spheroid (figure 3.38). After 24h of incubation Dox is not present in the spheroid. The same treatment but with 120 µM of Dox (figure 3.39) allows the visualization of Dox diffusion inwards over the first time points and outwards after 24h. These results can be explained by the fact that those cells are resistant to doxorubicin and, since, Dox is not present in the medium, the cells expel the Dox that is unable to enter, once there is not enough in the medium.

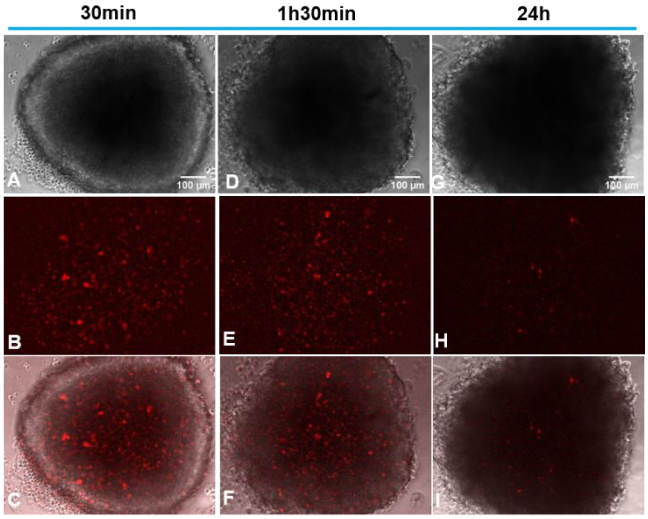

Figure 3.38 Fluorescence microscopy images of Dox resistant HCT116 spheroid with 8 days of growth and irradiated at 532 nm for 1 min after incubation with Dox 6 µM during 6h. The spheroid was visualized after 30 min, 1h30 min and 24h of incubation. (A) Bright Field image of spheroids after 30 min of incubation (B) Composite of images acquired with green excitation after 30 min of incubation. (C) Composite of images A and B (D) Bright Field image of spheroids after 1h30 min of incubation (E) Composite of images acquired with green excitation after 1h30 min of incubation. (F) Composite of images D and E (G) Bright Field image of spheroids after 24h of incubation (H) Composite of images acquired with green excitation after 24h of incubation. (I) Composite of images G and H The presented imagens were treated using ImageJ software.

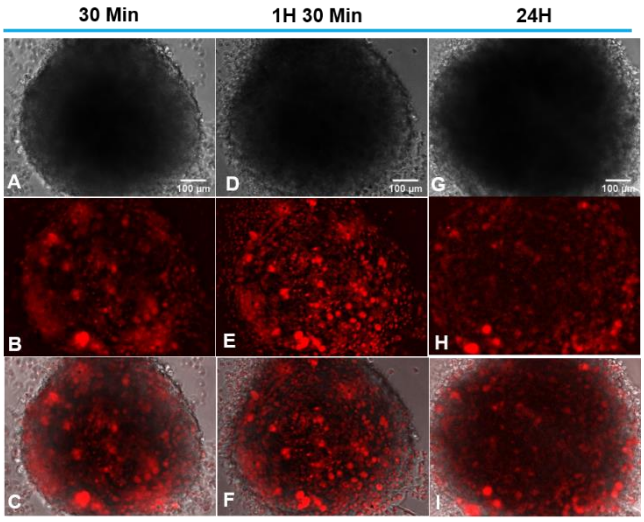

Figure 3.39 Fluorescence microscopy images of Dox resistant HCT116 spheroid with 8 days of growth and irradiated at 532 nm for 1 min after incubation with Dox 120 µM during 6h. The spheroid was visualized after 30 min, 1h30 min and 24h of incubation. (A) Bright Field image of spheroids after 30 min of incubation (B) Composite of images acquired with green excitation after 30 min of incubation. (C) Composite of images A and B (D) Bright Field image of spheroids after 1h30 min of incubation (E) Composite of images acquired with green excitation after 1h30 min of incubation. (F) Composite of images D and E (G) Bright Field image of spheroids after 24h of incubation (H) Composite of images acquired with green excitation after 24h of incubation. (I) Composite of images G and H The presented imagens were treated using ImageJ software.

The influence of AuNP@PEG in Dox diffusion in HCT116 DoxR spheroids was studied by treating spheroids with AuNP@PEG, followed by irradiation and incubation with two different concentration of Dox (6 and 120 µM). After incubation with 6 µM of Dox no changes were detected compared to the previously results (figure 3.40). On the other hand, incubation with 120 µM of Dox an accumulation and aggregation of Dox and a better penetration in the spheroids was

observed (figure 3.41). In both cases the bright field images present spheroid disintegration (figures 3.40 and 3.41).

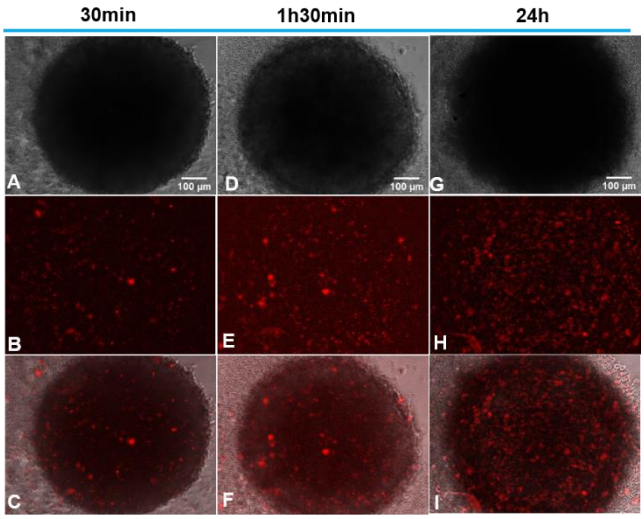

Figure 3.40 Fluorescence microscopy images of resistant HCT116 spheroid with 8 days of growth and incubated with 8 nM of AuNP-PEG (100%) during 24h and, after irradiated at 532 nm for1 min and incubated with Dox 6 µM during 30 min, 1h30 min and 24h. (A) Bright Field image of spheroids after 30 min of incubation (B) Composite of images acquired with green excitation after 30 min of incubation. (C) Composite of images A and B (D) Bright Field image of spheroids after 1h30 min of incubation (E) Composite of images acquired with green excitation after 1h30 min of incubation. (F) Composite of images D and E (G) Bright Field image of spheroids after 24h of incubation (H) Composite of images acquired with green excitation after 24h of incubation. (I) Composite of images G and H The presented imagens were treated using ImageJ software.

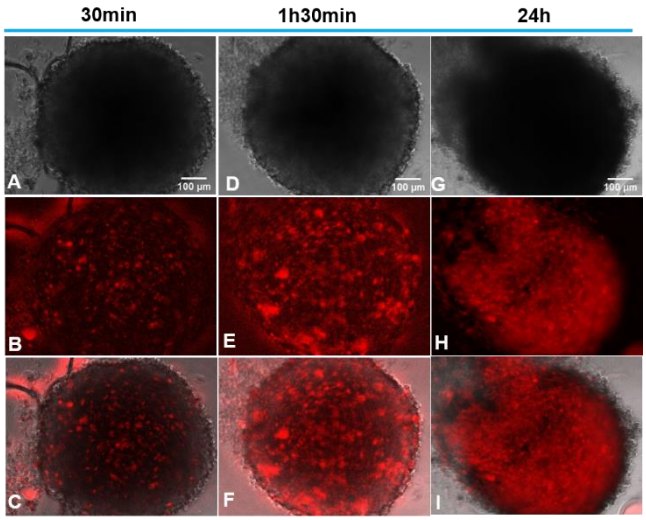

Figure 3.41 Fluorescence microscopy images of Dox resistant HCT116 spheroid with 8 days of growth and incubated with 8 nM of AuNP-PEG (100%) during 24h and, after irradiated at 532 nm for 1 min and incubated with Dox 120 µM during 30 min, 1h30 min and 24h. (A) Bright Field image of spheroids after 30 min of incubation (B) Composite of images acquired with green excitation after 30 min of incubation. (C) Composite of images A and B (D) Bright Field image of spheroids after 1h30 min of incubation (E) Composite of images acquired with green excitation after 1h30 min of incubation. (F) Composite of images D and E (G) Bright Field image of spheroids after 24h of incubation (H) Composite of images acquired with green excitation after 24h of incubation. (I) Composite of images G and H The presented imagens were treated using ImageJ software.

Interestingly, when irradiation was also combined and HCT116 DoxR spheroids were irradiated after treatment with AuNP@PEG and Dox (6 and 120 µM) strong Dox diffusion

throughout the spheroid was observed (figures 3.42 and 3.43). The bright field image of spheroids incubated with 120 µM shows morphological changes with spheroid disintegration (figure 3.43).

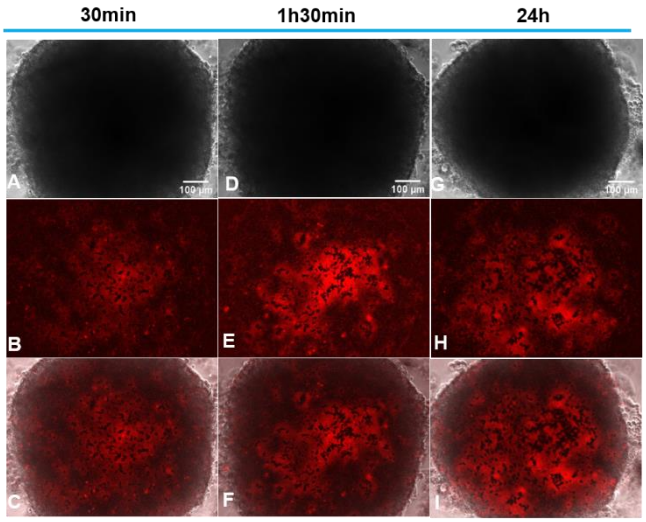

Figure 3.42 Fluorescence microscopy images of Dox resistant HCT116 spheroid with 8 days of growth and irradiated at 532 nm for 1 min after incubation with 8 nM of AuNP-PEG (100%) during 24h and with Dox 6 µM during 6h. The spheroid was visualized after 30 min, 1h30 min and 24h of incubation. (A) Bright Field image of spheroids after 30 min of incubation (B) Composite of images acquired with green excitation after 30 min of incubation. (C) Composite of images A and B (D) Bright Field image of spheroids after 1h30 min of incubation (E) Composite of images acquired with green excitation after 1h30 min of incubation. (F) Composite of images D and E (G) Bright Field image of spheroids after 24h of incubation (H) Composite of images acquired with green excitation after 24h of incubation. (I) Composite of images G and H The presented imagens were treated using ImageJ software.

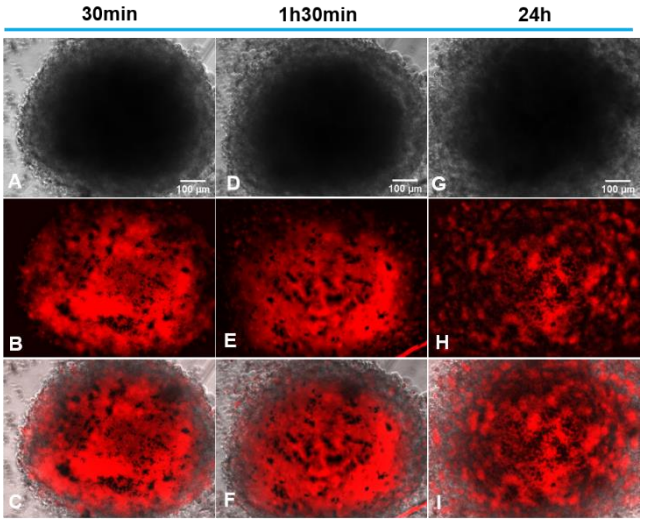

Figure 3.43 Fluorescence microscopy images of Dox resistant HCT116 spheroid with 8 days of growth and irradiated at 532 nm for 1 min after incubation with 8 nM of AuNP-PEG (100%) during 24h and with Dox 120 µM during 6h. The spheroid was visualized after 30 min, 1h30 min and 24h of incubation. (A) Bright Field image of spheroids after 30 min of incubation (B) Composite of images acquired with green excitation after 30 min of incubation. (C) Composite of images A and B (D) Bright Field image of spheroids after 1h30 min of incubation (E) Composite of images acquired with green excitation after 1h30 min of incubation. (F) Composite of images D and E (G) Bright Field image of spheroids after 24h of incubation (H) Composite of images acquired with green excitation after 24h of incubation. (I) Composite of images G and H The presented imagens were treated using ImageJ software.

In conclusion, the use of AuNP@PEG and Dox before irradiation allows the preservation of Dox in the HCT116 DoxR spheroids (figures 3.42 and 3.43). In a general way, the presence of

AuNP@PEG allows the aggregation of Dox in the spheroid core. Nevertheless, Dox diffusion in HCT116 DoxR spheroids was lower compared to dox diffusion in HCT116 spheroids (figures 3.26 and 3.32). These results are expected since the spheroids are constituted by cells resistant to the chemotherapeutic agent used.

Results presented allows to draw conclusions regarding the penetration/diffusion of the Dox in both types of spheroids in the absence or presence of AuNP and irradiation. In order to assess the best therapeutic strategy viability of cells inside the spheroids must be analysed.

3.4. Spheroids: Doxorubicin Diffusion and Cell Viability

In order to infer cell death effect during the different treatment strategies Dox and CellTox™ Green dye were added simultaneously.

Since Dox was diluted in DMSO, it was important to analyse if this solvent affected cell viability within the spheroids. Spheroids were incubated with the same percentage of DMSO as used with Dox. HCT116 spheroids incubated with DMSO do not present any morphological changes (figures 3.44). The CellTox™ Green staining in spheroids treated with DMSO (figure 3.45) indicated that DMSO does not cause more cell permeabilization compared to untreated spheroids (figure 3.18). Importantly, these results also show that CellTox™ Green dye emits in the red region (red images, figure 3.45) since the signal does not result from DMSO, as shown in the figure 3.44. This result indicate that we have to be careful when looking to Dox emission in the presence of CellTox™ dye.

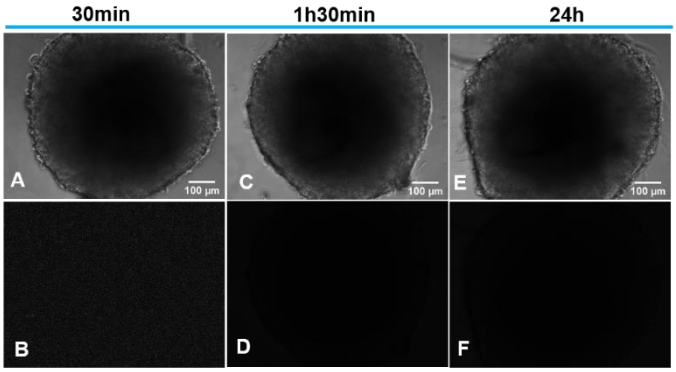

Figure 3.44 Fluorescence microscopy images of HCT116 spheroid with 8 days of growth and incubated with DMSO 0.1% during 30 min, 1h30min or 24h (A) Bright Field image of spheroids after 30 min of incubation (B) Composite of images acquired with green excitation after 30 min of incubation. (C) Bright Field image of spheroids after 1h30 min of incubation (D) Composite of images acquired with green excitation after 1h30 min of incubation. (E) Bright Field image of spheroids after 24h of incubation (F) Composite of images acquired with green excitation after 24h of incubation. The presented imagens were treated using ImageJ software.

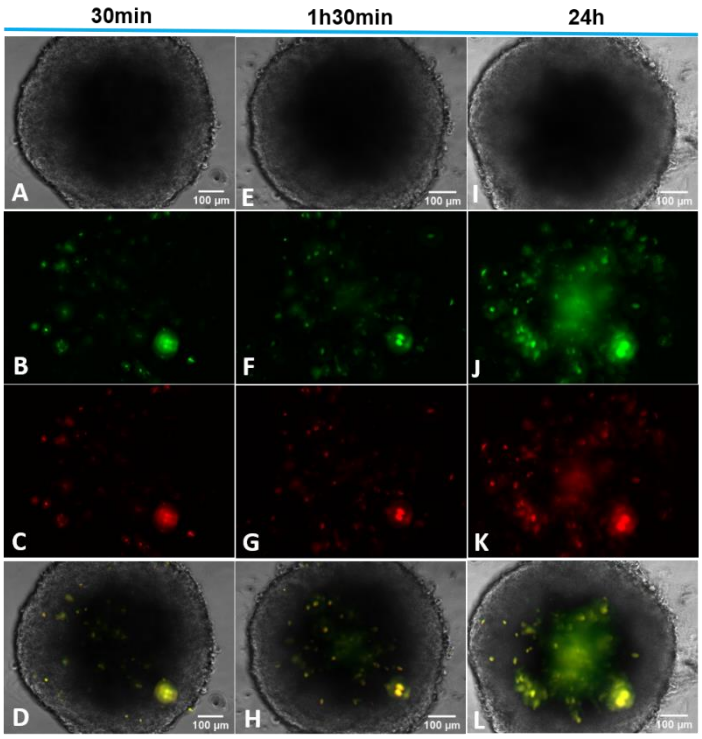

Figure 3.45 Fluorescence microscopy images of HCT116 spheroid with 8 days of growth and incubated with DMSO 0.1% and CellTox™ Green dye 1x during 30 min, 1h30min or 24h (A) Bright Field image of spheroids after 30 min of incubation (B) Composite of images acquired with blue excitation after 30 min of incubation. (C) Composite of images acquired with green excitation after 30 min of incubation. (D) Composite of images A, B and C (E) Bright Field image of spheroids after 1h30 min of incubation (F) Composite of images acquired with blue excitation after 1h30 min of incubation. (G) Composite of images acquired with green excitation after 1h30 min of incubation. (H) Composite of images E, F and G (I) Bright Field image of spheroids after 24h of incubation (J) Composite of images acquired with blue excitation after 24h of incubation. (K) Composite of images acquired with green excitation after 24h of incubation (L) Composite of images I, J and K. The presented imagens were treated using ImageJ software.

Subsequently, we analyse if Dox affect the cell viability or cellular membrane permeabilization using CellTox™ Green dye. Dox diffusion and cell death/ membrane permeabilization increase in HCT116 spheroids treated with Dox and incubated with CellTox™ Green dye (figure 3.46) with more pronounce staining at 24h (figure 3.46). These results show a lower Dox diffusion and cell death/ membrane permeabilization after 24h of incubation when compared with the previous results (HCT116 spheroids incubated separately with Dox (figure 3.26) and dye (figure 3.18)).

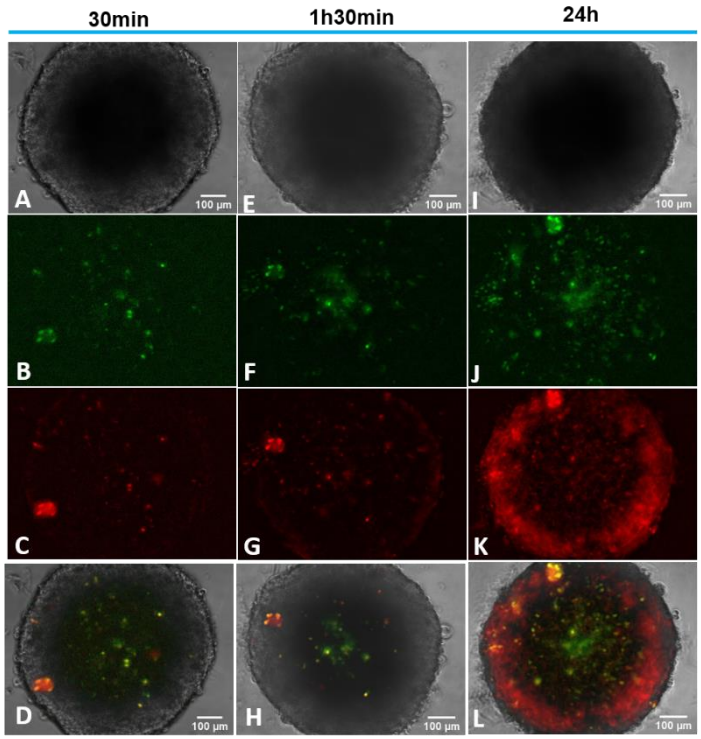

Figure 3.46 Fluorescence microscopy images of HCT116 spheroid with 8 days of growth and incubated with Dox 8 µM and CellTox™ Green dye 1x during 30 min,1h30min or 24h (A) Bright Field image of spheroids after 30 min of incubation (B) Composite of images acquired with blue excitation after 30 min of incubation. (C) Composite of images acquired with green excitation after 30 min of incubation. (D) Composite of images A, B and C (E) Bright Field image of spheroids after 1h30 min of incubation (F) Composite of images acquired with blue excitation after 1h30 min of incubation. (G) Composite of images acquired with green excitation after 1h30 min of incubation (H) Composite of images E, F and G (I) Bright Field image of spheroids after 24h of incubation (J) Composite of images acquired with blue excitation after 24h of incubation. (K) Composite of images acquired with green excitation after 24h of incubation (L) Composite of images I, J and K. The presented imagens were treated using ImageJ software.

The effect of Dox treatment on cell viability after AuNP@PEG incubation was also studied. HCT116 spheroids incubated with AuNP@PEG before Dox and CellTox™ Green dye incubation (figure 3.47) do not show an accumulation of Dox at the same region compared to spheroids that were treated with Dox only (figure 3.27) and presented lower cell death/membrane permeabilization compared to spheroids treated with AuNP@PEG only (figure 3.19). Red and green staining present overlap in some localizations.

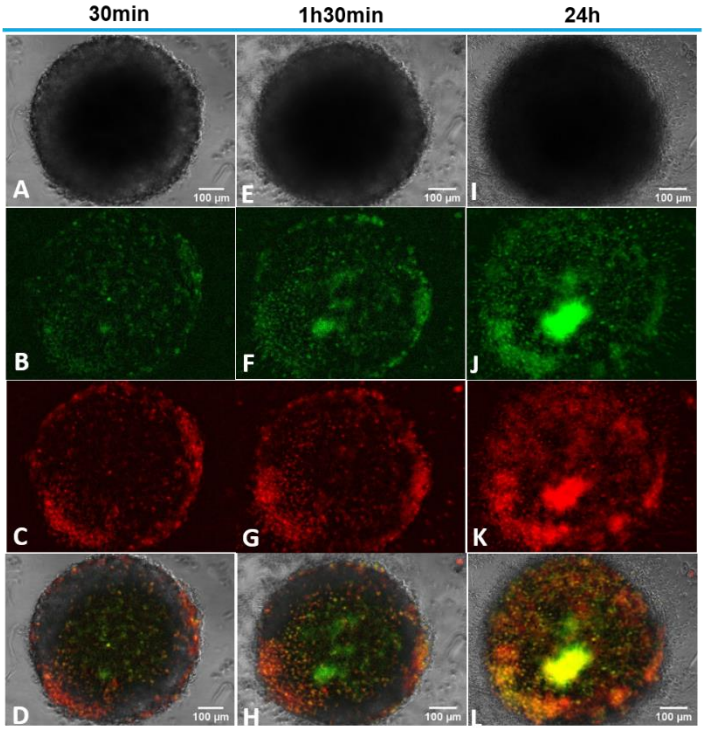

Figure 3.47 Fluorescence microscopy images of HCT116 spheroid with 8 days of growth and incubated with AuNP@PEG 8nM during 24H and after incubated with Dox 8 µM and CellTox™ Green dye 1x during 30 min,1h30min or 24h (A) Bright Field image of spheroids after 30 min of incubation (B) Composite of images acquired with blue excitation after 30 min of incubation. (C) Composite of images acquired with green excitation after 30 min of incubation. (D) Composite of images A, B and C (E) Bright Field image of spheroids after 1h30 min of incubation (F) Composite of images acquired with blue excitation after 1h30 min of incubation. (G) Composite of images acquired with green excitation after 1h30 min of incubation (H) Composite of images E, F and G (I) Bright Field image of spheroids after 24h min of incubation (J) Composite of images acquired with blue excitation after 24h of incubation. (K) Composite of images acquired with green excitation after 24h of incubation (L) Composite of images I, J and K. The presented imagens were treated using ImageJ software.

Irradiation in the visible of HCT116 spheroids before incubations (figure 3.48) leads to Dox accumulation over time in the periphery, and the same was observed in HCT116 spheroids irradiated before Dox incubation (figure 3.28). Figure 3.48 also indicate that cell death/loss of membrane integrity increases over time but appears to be less than in HCT116 spheroids irradiated only (figure 3.20).

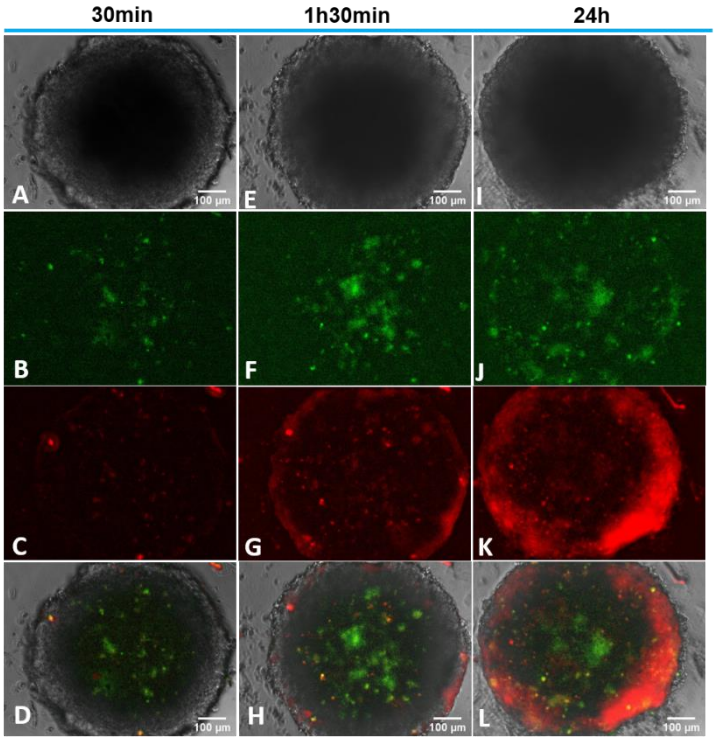

Figure 3.48 Fluorescence microscopy images of HCT116 spheroid with 8 days of growth and irradiated at 532 nm for 1 min and, after irradiation, was incubated with 8 µM of Doxorubicin (red) and CellTox™ Green dye during 30 min,1h30min or 24h. (A) Bright Field image of spheroid acquired after 30 min of incubation (B) Composite of images acquired with blue excitation after 30 min of incubation (C) Composite of images acquired with green excitation after 30 min of incubation. (D) Composite of images A, B and C (E) Bright Field image of spheroid acquired after 1h30 min of incubation (F) Composite of images acquired with blue excitation after 1h30 min of incubation (G) Composite of images acquired with green excitation after 1h30 min of incubation. (H) Composite of images E, F and G (I) Bright Field image of spheroid acquired after 24h of incubation (J) Composite of images acquired with blue excitation after 24h of incubation (K) Composite of images acquired with green excitation after 24h of incubation (L) Composite of images I, J and K. The presented imagens were treated using ImageJ software.

When HCT116 spheroids were irradiated in the visible with previously AuNP@PEG treatment and subsequent Dox and dye incubation (figure 3.49) an increase of cell death/membrane permeabilization over time was observe, however lower compared to HCT116 spheroids treated with AuNP@PEG before irradiation (figure 3.21). Figure 3.49 also indicates that Dox diffuses and accumulates over time. Red and green staining present overlap.

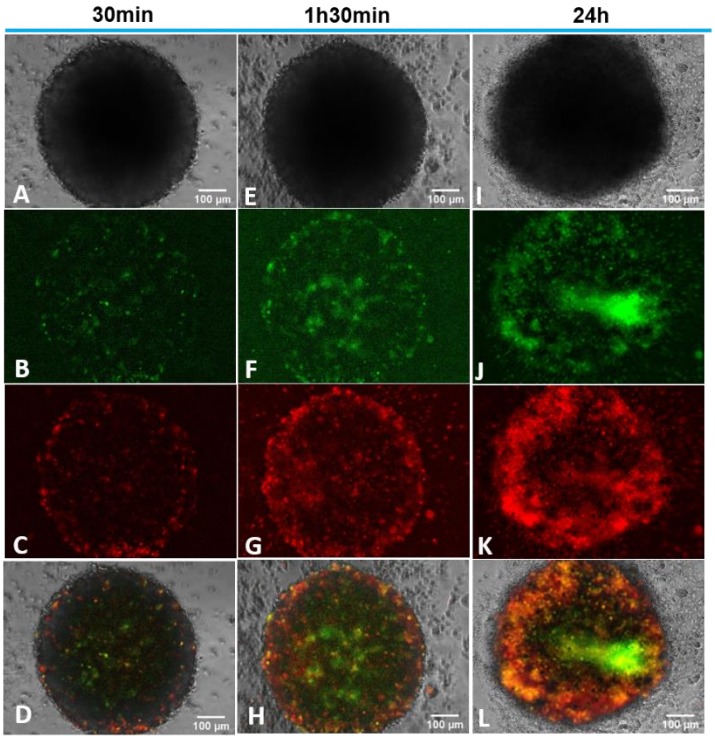

Figure 3.49 Fluorescence microscopy images of HCT116 spheroid with 8 days of growth and incubated with 8 nM of AuNP@PEG (100%) during 24h and, after irradiated at 532 nmfor 1 min andincubated with 8 µM of Doxorubicin (red) and CellTox™ Green dye 1x during 30 min, 1h30min or 24h. (A) Bright Field image of spheroid acquired after 30 min of incubation (B) Composite of images acquired with blue excitation after 30 min of incubation (C) Composite of images acquired with green excitation after 30 min of incubation. (D) Composite of images A, B and C (E) Bright Field image of spheroid acquired after 1h30 min of incubation (F) Composite of images acquired with blue excitation after 1h30 min of incubation (G) Composite of images acquired with green excitation after 1h30 min of incubation. (H) Composite of images E, F and G (I) Bright Field image of spheroid acquired after 24h of incubation (J) Composite of images acquired with blue excitation after 24h of incubation (K) Composite of images acquired with green excitation after 24h of incubation (L) Composite of images I, J and K. The presented imagens were treated using ImageJ software.

As before, HCT116 DoxR spheroids were submitted to the same treatments that HCT116 spheroids. The incubation with DMSO (figures 3.50 and 3.51) does not present morphological changes and, in comparison with untreated HCT116 DoxR spheroids (figure 3.22), the treated spheroids do not show increase of cell death/membrane permeabilization (figure 3.52). The results of DMSO incubation with the dye in HCT116 DoxR spheroids indicates that the dye emits in the red region (red images, figures 3.45 and 3.52) and, as observed in figures 3.50 and 3.51, the red signal (figure 3.52) does not result from DMSO.

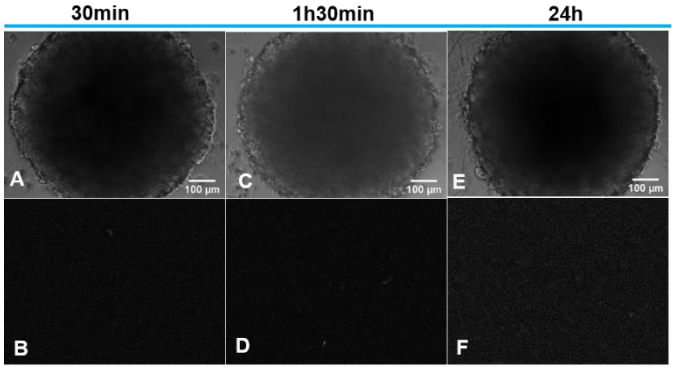

Figure 3.50 Fluorescence microscopy images of HCT116 DoxR spheroid with 8 days of growth and incubated with DMSO 0.1% during 30 min, 1h30min or 24h (A) Bright Field image of spheroids after 30 min of incubation (B) Composite of images acquired with green excitation after 30 min of incubation. (C) Bright Field image of spheroids after 1h30 min of incubation (D) Composite of images acquired with green excitation after 1h30 min of incubation. (E) Bright Field image of spheroids after 24h of incubation (F) Composite of images acquired with green excitation after 24h of incubation. The presented imagens were treated using ImageJ software.

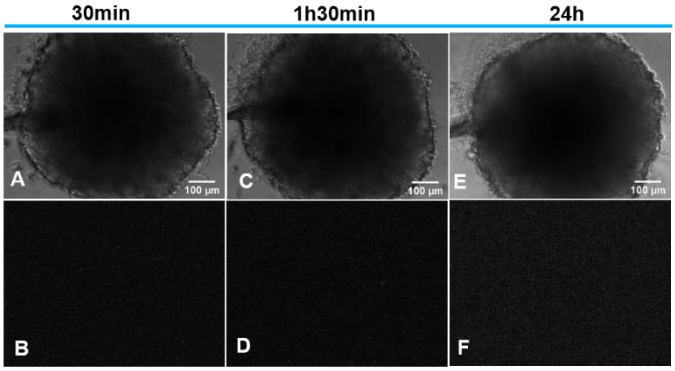

Figure 3.51 Fluorescence microscopy images of HCT116 DoxR spheroid with 8 days of growth and incubated with DMSO 0.8% during 30 min, 1h30min or 24h (A) Bright Field image of spheroids after 30 min of incubation (B) Composite of images acquired with green excitation after 30 min of incubation. (C) Bright Field image of spheroids after 1h30 min of incubation (D) Composite of images acquired with green excitation after 1h30 min of incubation. (E) Bright Field image of spheroids after 24h of incubation (F) Composite of images acquired with green excitation after 24h of incubation. The presented imagens were treated using ImageJ software.

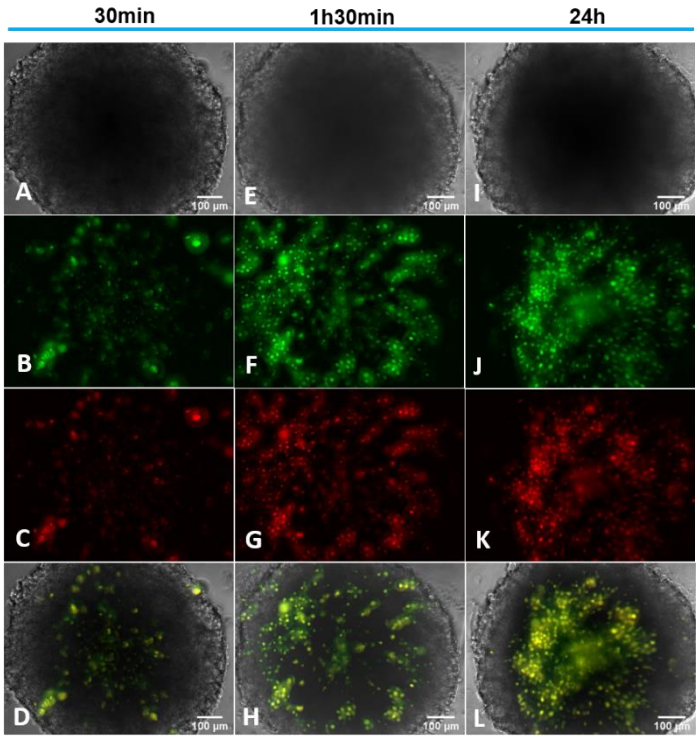

Figure 3.52 Fluorescence microscopy images of HCT116 DoxR spheroid with 8 days of growth and incubated with DMSO 0.1% and CellTox™ Green dye 1x during 30 min, 1h30min or 24h (A) Bright Field image of spheroids after 30 min of incubation (B) Composite of images acquired with blue excitation after 30 min of incubation. (C) Composite of images acquired with green excitation after 30 min of incubation. (D) Composite of images A, B and C (E) Bright Field image of spheroids after 1h30 min of incubation (F) Composite of images acquired with blue excitation after 1h30 min of incubation. (G) Composite of images acquired with green excitation after 1h30 min of incubation. (H) Composite of images E, F and G (I) Bright Field image of spheroids after 24h of incubation (J) Composite of images acquired with blue excitation after 24h of incubation. (K) Composite of images acquired with green excitation after 24h of incubation (L) Composite of images I, J and K. The presented imagens were treated using ImageJ software.

When we studied Dox diffusion and cell viability simultaneously in HCT116 DoxR spheroids incubated with 6 µM Dox (figure 3.53), a decrease of cell death/membrane permeabilization was observed compared to the untreated HCT116 DoxR spheroids (figure 3.22). In the case of incubation with 120 µM of Dox (figure 3.54) the therapeutic agent diffuses over time and, after 24h, was localized mostly in the central region. Cell death/membrane permeabilization increases over time and, after 24h, was localized in the central region, but presenting a lower green staining compared to spheroids not incubated with Dox (figure 3.22).

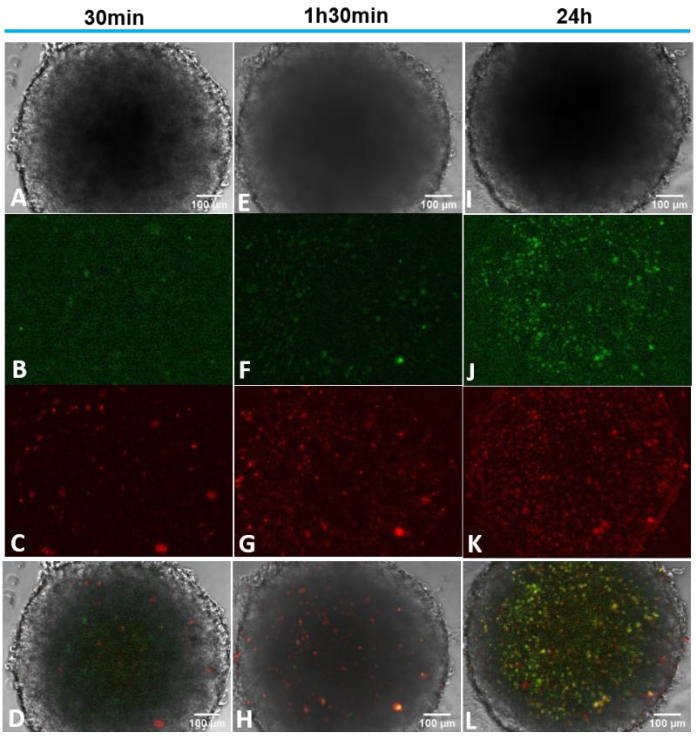

Figure 3.53 Fluorescence microscopy images HCT116 DoxR spheroid with 8 days of growth and incubated with Dox 6 µM and CellTox™ Green dye 1x during 30 min,1h30min or 24h (A) Bright Field image of spheroids after 30 min of incubation (B) Composite of images acquired with blue excitation after 30 min of incubation. (C) Composite of images acquired with green excitation after 30 min of incubation. (D) Composite of images A, B and C (E) Bright Field image of spheroids after 1h30 min of incubation (F) Composite of images acquired with blue excitation after 1h30 min of incubation. (G) Composite of images acquired with green excitation after 1h30 min of incubation (H) Composite of images E, F and G (I) Bright Field image of spheroids after 24h of incubation (J) Composite of images acquired with blue excitation after 24h of incubation. (K) Composite of images acquired with green excitation after 24h of incubation (L) Composite of images I, J and K. The presented imagens were treated using ImageJ software.

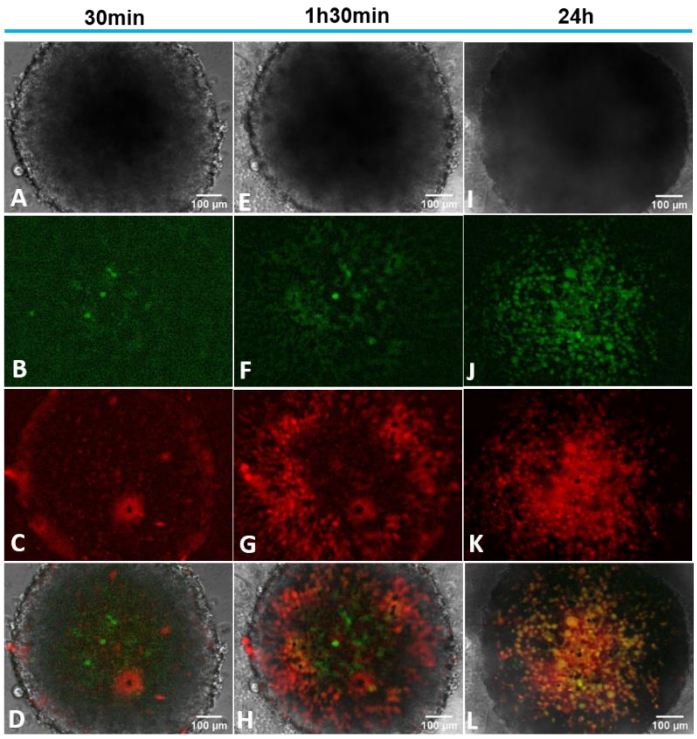

Figure 3.54 Fluorescence microscopy images of HCT116 DoxR spheroid with 8 days of growth and incubated with Dox 120 µM and CellTox™ Green dye 1x during 30 min,1h30min or 24h (A) Bright Field image of spheroids after 30 min of incubation (B) Composite of images acquired with blue excitation after 30 min of incubation. (C) Composite of images acquired with green excitation after 30 min of incubation. (D) Composite of images A, B and C (E) Bright Field image of spheroids after 1h30 min of incubation (F) Composite of images acquired with blue excitation after 1h30 min of incubation. (G) Composite of images acquired with green excitation after 1h30 min of incubation. (H) Composite of images E, F and G (I) Bright Field image of spheroids after 24h of incubation (J) Composite of images acquired with blue excitation after 24h of incubation. (K) Composite of images acquired with green excitation after 24h of incubation (L) Composite of images I, J and K. The presented imagens were treated using ImageJ software.

When cells were treated with AuNP@PEG 24h before incubation with 6 µM of Dox and the dye (figure 3.55) the cell death/membrane permeabilization increases over time and at 24h a circle of green staining in the middle region of the spheroids was observed. We can also observe Dox diffusion over time and, after 24h, the accumulation in a peripheral circle. HCT116 DoxR spheroids, incubated with 120 µM of Dox (figure 3.56), present lower diffusion of Dox compared with spheroids treated with AuNP@PEG before Dox treatment (figure 3.35) and the cell death/loss of membrane integrity increased over time (figure 3.56).

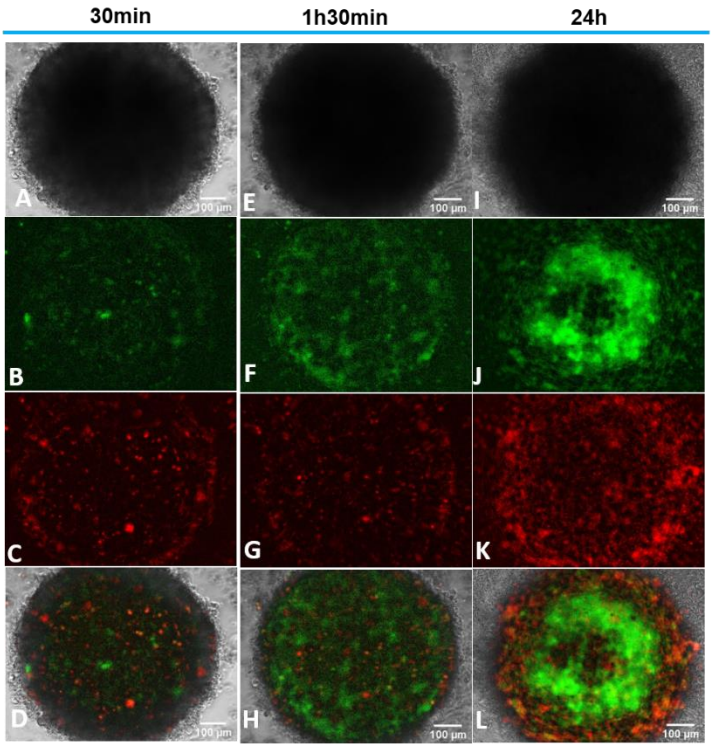

Figure 3.55 Fluorescence microscopy images of HCT116 DoxR spheroid with 8 days of growth and incubated with AuNP@PEG 8nM during 24h and after incubated with Dox 6 µM during 30 min,1h30min or 24h (A) Bright Field image of spheroids after 30 min of incubation (B) Composite of images acquired with blue excitation after 30 min of incubation. (C) Composite of images acquired with green excitation after 30 min of incubation. (D) Composite of images A, B and C (E) Bright Field image of spheroids after 1h30 min of incubation (F) Composite of images acquired with blue excitation after 1h30 min of incubation. (G) Composite of images acquired with green excitation after 1h30 min of incubation (H) Composite of images E, F and G (I) Bright Field image of spheroids after 24h min of incubation (J) Composite of images acquired with blue excitation after 24h of incubation. (K) Composite of images acquired with green excitation after 24h of incubation (L) Composite of images I, J and K. The presented imagens were treated using ImageJ software.

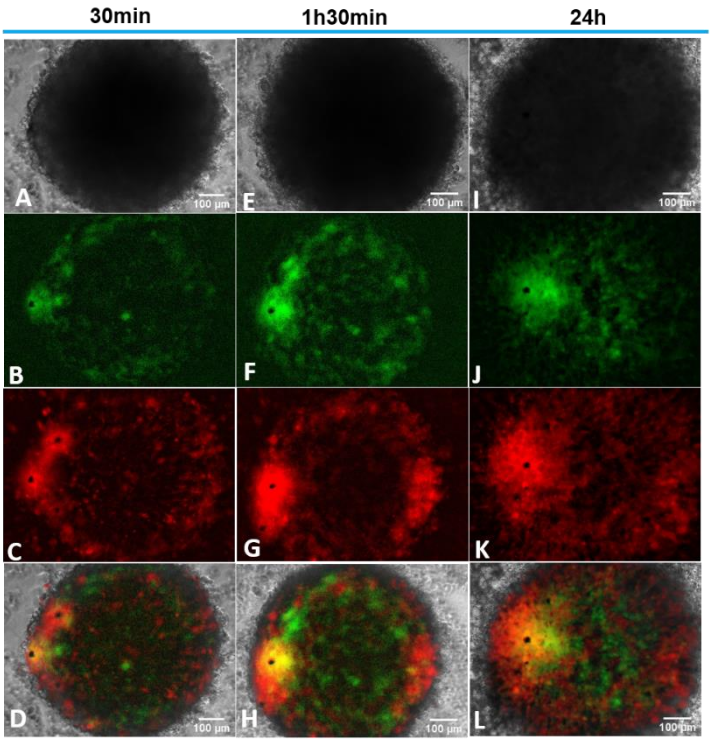

Figure 3.56 Fluorescence microscopy images of HCT116 DoxR spheroid with 8 days of growth and incubated with AuNP@PEG 8nM during 24h and after incubated with Dox 120 µM during 30 min,1h30min or 24h (A) Bright Field image of spheroids after 30 min of incubation (B) Composite of images acquired with blue excitation after 30 min of incubation. (C) Composite of images acquired with green excitation after 30 min of incubation. (D) Composite of images A, B and C (E) Bright Field image of spheroids after 1h30 min of incubation (F) Composite of images acquired with blue excitation after 1h30 min of incubation. (G) Composite of images acquired with green excitation after 1h30 min of incubation (H) Composite of images E, F and G (I) Bright Field image of spheroids after 24h of incubation (J) Composite of images acquired with blue excitation after 24h of incubation. (K) Composite of images acquired with green excitation after 24h of incubation (L) Composite of images I, J and K. The presented imagens were treated using ImageJ software.

Irradiation in the visible and treatment subsequently with 6 µM of Dox shows a decrease of death/loss of membrane integrity (figure 3.57) compared to the HCT116 DoxR spheroids without Dox treatment (figure 2.24). Also, Dox is able to diffuse (figure 3.57) but less compared to Dox-treated spheroids after irradiation (figure 3.36). When HCT116 DoxR spheroids were treated with 120 µM of Dox, it was able to spread to an inner/central region with an increase cell death/loss of membrane integrity over time (figure 3.58) but with a lower green staining compared to irradiated HCT116 DoxR spheroids (figure 2.24).

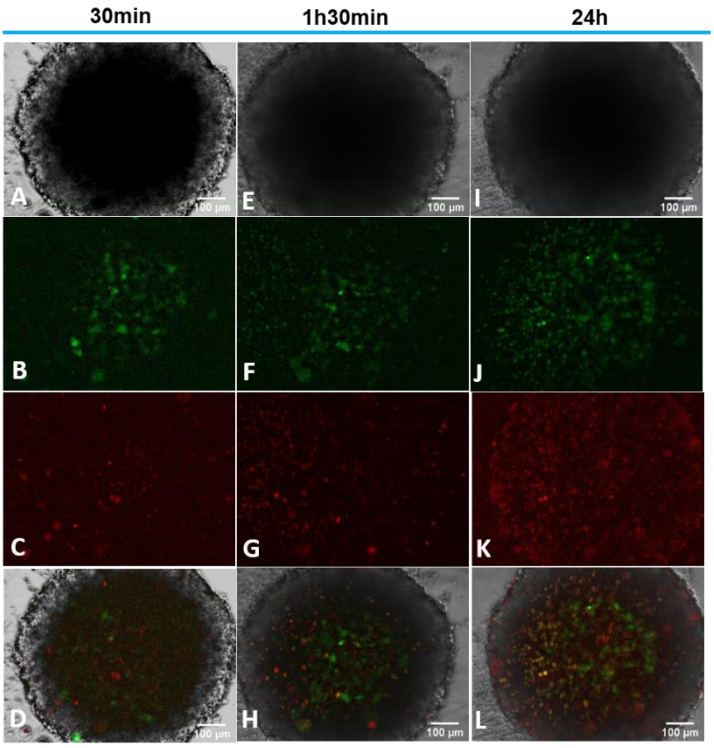

Figure 3.57 Fluorescence microscopy images of HCT116 DoxR spheroid with 8 days of growth and irradiated at 532 nm for 1 min, and after irradiation, was incubated with 6 µM of Doxorubicin (red) and and CellTox^{TM} Green dye 1x during 30 min,1h30min or 24h. (A) Bright Field image of spheroid acquired after 30 min of incubation (B) Composite of images acquired with blue excitation after 30 min of incubation (C) Composite of images acquired with green excitation after 30 min of incubation. (D) Composite of images A, B and C (E) Bright Field image of spheroid acquired after 1h30 min of incubation (F) Composite of images acquired with blue excitation after 1h30 min of incubation (G) Composite of images acquired with green excitation after 1h30 min of incubation (H) Composite of images E, F and G (I) Bright Field image of spheroid acquired after 24h of incubation (J) Composite of images acquired with blue excitation after 24h of incubation (K) Composite of images acquired with green excitation after 24h of incubation (L) Composite of images I, J and K. The presented imagens were treated using ImageJ software.

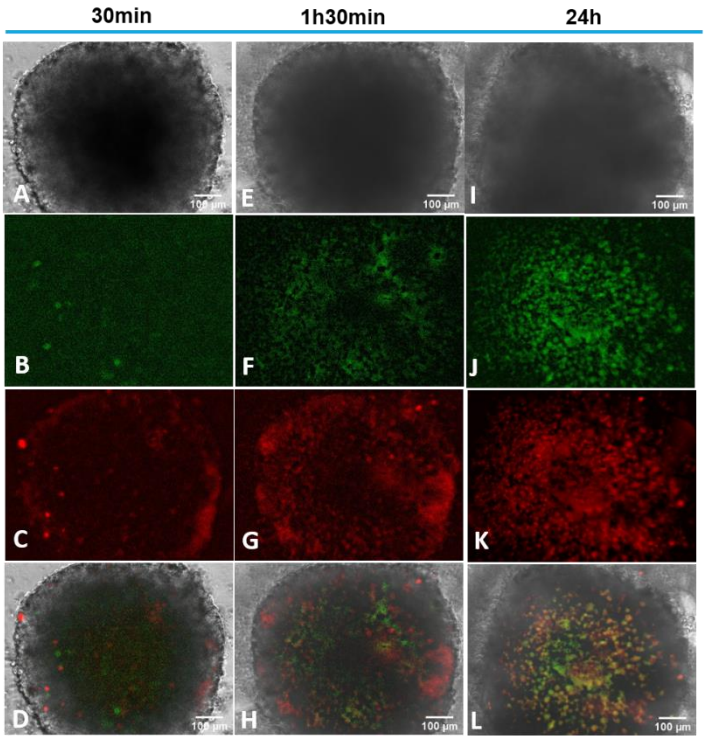

Figure 3.58 Fluorescence microscopy images of HCT116 DoxR spheroid with 8 days of growth and irradiated at 532 nm for 1 min and after irradiation was incubated with 120 µM of Doxorubicin (red) and CellTox™ Green dye 1x during 30 min,1h30min or 24h. (A) Bright Field image of spheroid acquired after 30 min of incubation (B) Composite of images acquired with blue excitation after 30 min of incubation (C) Composite of images acquired with green excitation after 30 min of incubation. (D) Composite of images A, B and C (E) Bright Field image of spheroid acquired after 1h30 min of incubation (F) Composite of images acquired with blue excitation after 1h30 min of incubation (G) Composite of images acquired with green excitation after 1h30 min of incubation (H) Composite of images E, F and G (I) Bright Field image of spheroid acquired after 24h of incubation (J) Composite of images acquired with blue excitation after 24h of incubation (K) Composite of images acquired with green excitation after 24h of incubation (L) Composite of images I, J and K. The presented imagens were treated using ImageJ software.

Combining AuNP@PEG and irradiation in HCT116 DoxR spheroids before 6 µM Dox and CellTox™ Green incubation (figure 3.59), allowed to observe Dox diffusion and an increase of cell death/loss of membrane integrity over time. These results differ from the experiences in which Dox (figure 3.40) and CellTox™ Green dye (figure 3.25) were used separately. When the concentration of Dox was 120 µM (figure 3.60) Dox accumulates in the spheroid periphery and we can observe a localized cell death/membrane permeabilization. These results presenting a lower Dox diffusion and cell death/membrane permeabilization compared to the results of HCT116 DoxR spheroids treated with Dox (figure 3.41) and the dye (figure 3.25) separately.

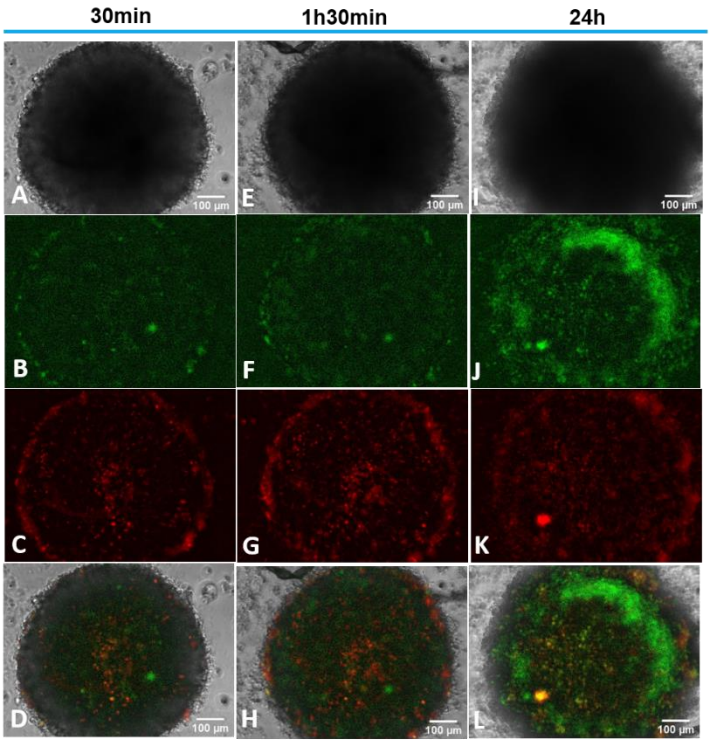

Figure 3.59 Fluorescence microscopy images of HCT116 DoxR spheroid with 8 days of growth and incubated with 8 nM of AuNP@PEG (100%) during 24h and, after irradiated at 532 nm for 1 min and incubated with 6 µM of Doxorubicin (red) and CellTox™ Green dye 1x during 30 min, 1h30min or 24h. (A) Bright Field image of spheroid acquired after 30 min of incubation (B) Composite of images acquired with blue excitation after 30 min of incubation (C) Composite of images acquired with green excitation after 30 min of incubation. (D) Composite of images A, B and C (E) Bright Field image of spheroid acquired after 1h30 min of incubation (F) Composite of images acquired with blue excitation after 1h30 min of incubation (G) Composite of images acquired with green excitation after 1h30 min of incubation (H) Composite of images E, F and G (I) Bright Field image of spheroid acquired after 24h of incubation (J) Composite of images acquired with blue excitation after 24h of incubation (K) Composite of images acquired with green excitation after 24h of incubation (L) Composite of images I, J and K. The presented imagens were treated using ImageJ software.

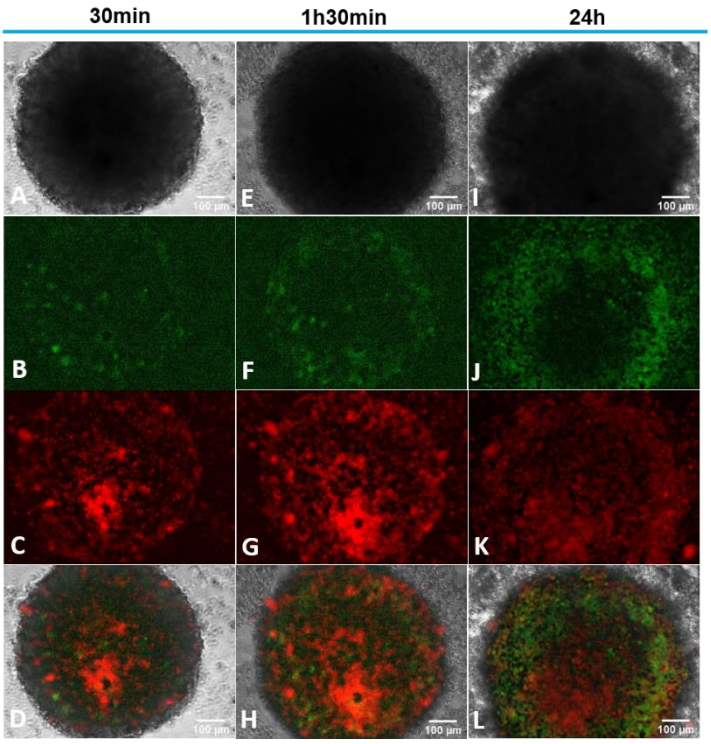

Figure 3.60 Fluorescence microscopy images of HCT116 DoxR spheroid with 8 days of growth and incubated with 8 nM of AuNP@PEG (100%) during 24h and, after irradiated at 532 nm for 1 min and incubated with 120 µM of Doxorubicin (red) and CellTox™ Green dye 1x during 30 min, 1h30min or 24h. (A) Bright Field image of spheroid acquired after 30 min of incubation (B) Composite of images acquired with blue excitation after 30 min of incubation (C) Composite of images acquired with green excitation after 30 min of incubation. (D) Composite of images A, B and C (E) Bright Field image of spheroid acquired after 1h30 min of incubation (F) Composite of images acquired with blue excitation after 1h30 min of incubation (G) Composite of images acquired with green excitation after 1h30 min of incubation (H) Composite of images E, F and G (I) Bright Field image of spheroid acquired after 24h of incubation (J) Composite of images acquired with blue excitation after 24h of incubation (K) Composite of images acquired with green excitation after 24h of incubation (L) Composite of images I, J and K. The presented imagens were treated using ImageJ software.

Results of simultaneous incubation of CellTox™ Green dye and Dox present some inconsistencies with the previous results of the same agents but in separate. This can be explained by the fact that both agents target DNA (36) and presented an overlap of absorption and emission spectra (see appendices A and B). Therefore, the signals of the dye and Dox together may not represent the real effect and might lead to a bias interpretation. In the future, is will be necessary to perform the same experiences with a different cell death probe.

3.5. TNF-α expression

The tumour necrosis factor alpha (TNF-α) is a cytokine involved in several processes, including homeostasis (66,67), inflammation (66,67,68), immunity (67,68), apoptosis, cell survival (68) and tumour progression (67). Several evidences point to a close relationship between inflammation and cancer (26,66). TNF-α has an important role in the association between inflammation and cancer and participates in tumorigenesis process, including cell transformation, proliferation, invasion and migration (67).

Necrotic cell death occurs in the tumour and play an important role in the promotion of inflammation through the release of pro-inflammatory mediators (26,27). The results presented in this work, raised the question an inflammatory response could be trigger after the application of those treatment strategies. Considering this, we decided to study the release of pro-inflammatory mediators after the application of each treatment strategy and if this release could be even increased in the presence of cells of the immune system (Thp-1). Thp-1 cells are monocytes that can be differentiated into macrophages which, in turn, express large amounts of TNF-α (26). Once that the TNF-α is a pro-inflammatory cytokine (26) that, in the tumour microenvironment, functions as a tumour promoting factor (66,67) its relative expression ($2^{-\Delta\Delta Ct}$) was analysed in HCT116 and HCT116 DoxR spheroids and Thp-1 cells alone or in co-culture.

We can observe in table 3.1 that the expression of TNF-α decreases or remains constant when compared with the respective controls after the application of the different treatment strategies, which indicates that inflammation and tumoral progression mediated by TNF-α might be restrained due to the application of treatments, in particular, when combining AuNP and irradiation. However, these are preliminary data that needs to be further addressed by testing other pro-inflammatory (IL-6) and anti-inflammatory (IL-10) mediators associated with tumour development and progression.

Table 3.1 Relative expression of TNF-α according to the $2^{-\Delta\Delta}_{CT}$ method by different tested cells treated with AuNP@PEG, irradiated or irradiated after AuNP@PEG treatment. Expression level in tested cells compared with comparative cells. $2^{-\Delta\Delta}_{CT}$ was calculated through the results present in the appendices C and D.

Tested Cells	Cells present in the well	Spheroids Treatment	Comparative Cells	$2^{-\Delta\Delta Ct}$	Expression level
HCT116 spheroid	Thp-1	AuNP@PEG	HCT116 spheroid untreated	5,59E-07	Decrease
Thp-1	HCT116 spheroid		Thp1 untreated	1	Without Changes
HCT116 DoxR spheroid	Thp-1	AuNP@PEG	HCT116 DoxR spheroid untreated	1	Without Changes
Thp-1	HCT116 DoxR spheroid		Thp1 untreated	1	Without Changes
HCT116 spheroid	Thp-1	Irradiation	HCT116 spheroid untreated	1,51E-06	Decrease
Thp-1	HCT116 spheroid		Thp1 untreated	1	Without Changes
HCT116 spheroid	Thp-1	AuNP@PEG Irradiation	HCT116 spheroid treated with AuNP@PEG	1	Without Changes
Thp-1	HCT116 spheroid		Thp1 treated with AuNP@PEG	1,43E-04	Decrease
HCT116 DoxR spheroid	Thp-1	Irradiation	HCT116 DoxR spheroid untreated	1,32E-03	Decrease
Thp-1	HCT116 DoxR spheroid		Thp1 untreated	8,67E-03	Decrease
HCT116 DoxR spheroid	Thp-1	AuNP@PEG Irradiation	HCT116 DoxR spheroid treated with AuNP@PEG	1,19E-03	Decrease
Thp-1	HCT116 DoxR spheroid		Thp1 treated with AuNP@PEG	1	Without Changes

4. Conclusion

Cancer is responsible for millions of deaths annually and the current therapy can be ineffective and, in some cases, responsible for serious side effects. The tumour microenvironment is implicated in several steps of tumorigenesis and in the response to therapy. The present work allowed to study the internalization of Dox in 2D co-cultures of cancer cells (HCT116 cells and HCT116 DoxR cells) and fibroblasts vs 2D monocultures of the same cells and the diffusion of the same drug in 3D cultures, more specifically spheroids. To combat the inefficiency of current therapies, approaches with gold nanoparticles were also study.

Co-culture with fibroblasts seems to influence the internalization of Dox by HCT116 cells but not by HCT116 DoxR cells that are resistant to Dox. Results show an increase of Dox internalization by HCT116 cells in co-culture. Results also indicate that cancer cells without resistance (HCT116 cells) presenting more Dox internalization compared to normal cells like fibroblasts. These results point to the fact that is necessary to consider, in *in vitro* studies of new chemotherapeutic agents, the presence of stromal cells and cancer cells.

HCT116 and HCT116 DoxR spheroids mimic the existence of a necrotic core which suggest that there is oxygen and, possibly, nutrient gradients. Gold nanoparticles functionalized with PEG allows an improved diffusion of doxorubicin in the spheroids and may permeabilize the spheroid and/or lead to cell death without triggering inflammation. The treatment with AuNP@PEG with and without irradiation can be applied, in the future, in combination with therapeutic agents, such as Dox, to increase the therapeutic efficacy and decrease the dosage of the agent important for the decrease of side effects. The photothermal therapy with AuNP@PEG and the combination with Dox therapy may be the best approach for improving HCT116 treatment and particularly, in patients with Dox resistance. Nevertheless, more studies are needed to provide a definitive validation of these results.

The inflammatory response in spheroids irradiated after AuNP@PEG treatment must be study with more detail and is a promising therapy, considering the results of TNF-α expression and the evidence that AuNPs as photothermal agent are effective in destroying tumour cells. In addition, the study of these approaches in longer-growing spheroids are helpful to understand if they might work also in larger tumours. Also, would be interesting analyse the diffusion of Dox for longer times or when present in the medium when the spheroid is irradiated. Studies with cell death markers linked to apoptosis and necrosis may indicated the specific cell death and are helpful for understanding these approaches. Techniques like fluorescence spectroscopy, immunohistochemistry or confocal microscopy can be applied in future studies.

Bibliography

1. Stratton MR. Exploring the genomes of cancer cells: Progress and promise. Science. 2011;331:1553–8.
2. Singh P, Pandit S, Mokkapati VRSS, Garg A, Ravikumar V, Mijakovic I. Gold nanoparticles in diagnostics and therapeutics for human cancer. Int J Mol Sci. 2018;19:1979-95.
3. Haume K, Rosa S, Grellet S, Śmiałek MA, Butterworth KT, Solov'yov A V., Prise KM, Golding J., Mason NJ. Gold nanoparticles for cancer radiotherapy: a review. Cancer Nanotechnol. 2016;7:1-20.
4. Ashworth A, Lord CJ, Reis-filho JS. Genetic Interactions in Cancer Progression and Treatment. Cell. 2011;145:30–8.
5. Guo J, Rahme K, He Y, Li LL, Holmes JD, O'Driscoll CM. Gold nanoparticles enlighten the future of cancer theranostics. Int J Nanomedicine. 2017;12:6131–52.
6. Hahn MM, Voer RM De, Hoogerbrugge N, Ligtenberg MJL. The genetic heterogeneity of colorectal cancer predisposition - guidelines for gene discovery. Cell Oncol. 2016;39:491–510.
7. Granados-romero JJ, Valderrama-treviño AI, Contreras-flores EH, Barrera-mera B, Enríquez MH, Uriarte-ruíz K, Ceballos-Villalva JC, Estrada-Mata AG, Rodríguez CA, Arauz-Peña G. Colorectal cancer : a review. 2017;5:4667–76.
8. Roncucci L, Mariani F. Prevention of colorectal cancer : How many tools do we have in our basket ? Eur J Intern Med. 2015;26:752-6
9. Adjei I, Blanka S. Modulation of the Tumor Microenvironment for Cancer Treatment: A Biomaterials Approach. J Funct Biomater. 2015;6:81–103.
10. Siegler EL, Kim YJ, Wang P. Nanomedicine targeting the tumor microenvironment: Therapeutic strategies to inhibit angiogenesis, remodel matrix, and modulate immune responses. J Cell Immunother. 2016;2:69–78.
11. Waseem Asghar, Rami El Assal, Hadi Shafiee, Sharon Pitteri RP and UD. Engineering cancer microenvironments for in vitro 3-D tumor models. Mater Today. 2015;18:539–53.
12. Yuan Y, Jiang YC, Sun CK, Chen QM. Role of the tumor microenvironment in tumor progression and the clinical applications (Review). Oncol Rep. 2016;35:2499–515.
13. Bussard KM, Mutkus L, Stumpf K, Gomez-Manzano C, Marini FC. Tumor-associated stromal cells as key contributors to the tumor microenvironment. Breast Cancer Res. 2016;18:1–11.
14. Bruno A, Ferlazzo G, Albini A, Noonan DM. A Think Tank of TINK / TANKs : Tumor-Infiltrating / Tumor-Associated Natural Killer Cells in Tumor Progression and Angiogenesis. J Natl Cancer Inst. 2014;106:1-13.
15. Bruno A, Focaccetti C, Pagani A, Imperatori AS, Spagnoletti M, Rotolo N, Cantelmo AR, Franzi F, Capella C, Ferlazzo G, Mortara L, Albini A, Noonan DM. The Proangiogenic Phenotype of Natural Killer Cells in Patients with Non– Small Cell Lung Cancer. Neoplasia. 2013;15:133–42.
16. Yu J, Du W, Yan F, Wang Y, Li H, Yu W, Shen C, Liu J, Ren X. Myeloid-Derived Suppressor Cells Suppress Antitumor Immune Responses through IDO Expression and Correlate with Lymph Node Metastasis in Patients with Breast Cancer. J Immunol. 2013;190:3783-97
17. Kumar V, Patel S, Tcyganov E, Gabrilovich DI. The nature of myeloid-derived suppressor cells in the tumor microenvironment. Trends Immunol. 2017;37:208–20.
18. Danhier F, Feron O, Préat V. To exploit the tumor microenvironment : Passive and active tumor targeting of nanocarriers for anti-cancer drug delivery. J Control Release. 2010;148:135–46.
19. Alemany-Ribes M, Semino CE. Bioengineering 3D environments for cancer models. Adv Drug Deliv Rev. 2014;79:40–9.
20. Shi H, Wang Z, Huang C, Gu X, Jia T, Zhang A. A Functional CT Contrast Agent for In Vivo Imaging of Tumor Hypoxia. Small. 2016;12:3995-4006.
21. Dachs GU, Tozer GM. Hypoxia modulated gene expression : angiogenesis , metastasis and therapeutic exploitation. Eur J Cancer. 2000;36:1649–60.
22. Shannon AM, Bouchier-hayes DJ, Condron CM, Toomey D. Tumour hypoxia, chemotherapeutic resistance and hypoxia-related therapies. Cancer Treat Rev. 2003;29:297–307.
23. Harris AL. Hypoxia-a key regulatory factor in tumour growth. Nature. 2002;2:38–47.
24. Shwelki D., Itin A., Soffer D., Keshet E. Vascular endothelial growth factor induced by

hypoxia may mediate hypoxia-initiated angiogenesis. Nature. 1992;359:843–5.
25. Yu Z, Tang B, Wang M, Pan W, Wang H. Tumor microenvironment-triggered fabrication of gold nanomachines for tumor-specific photoacoustic imaging and photothermal therapy. Chem Sci. 2017;8:4896–903.
26. Grivennikov SI, Greten FR, Karin M. Immunity, Inflammation, and Cancer. Cell. 2010;140:883–99.
27. Bredholt G, Mannelqvist M, Stefansson IM, Birkeland E, Bø TH, Øyan AM, Trovik J, Kalland KH, Jonassen I, Salvesen HB, Wik E, Akshen LA. Tumor necrosis is an important hallmark of aggressive endometrial cancer and associates with hypoxia , angiogenesis and inflammation responses. Oncotarget. 2015;6:39676–91.
28. Larson B. 3D Cell Culture : A Review of Current Techniques. BioTek. 2015;6:1–10.
29. Costa EC, Moreira AF, de Melo-Diogo D, Gaspar VM, Carvalho MP, Correia IJ. 3D tumor spheroids : an overview on the tools and techniques used for their analysis. Biotechnol Adv. 2016;34:1427–41.
30. Weiswald L, Bellet D, Dangles-marie V. Spherical Cancer Models in Tumor Biology. Neoplasia. 2015;17:1–15.
31. Lee JM, Mhawech-fauceglia P, Lee N, Parsanian LC, Lin YG, Gayther SA, Lawrenson. A three-dimensional microenvironment alters protein expression and chemosensitivity of epithelial ovarian cancer cells in vitro. Nature. 2013;93:528–42.
32. Eglen RM, Randle DH. Drug Discovery Goes Three-Dimensional: Goodbye to Flat High-Throughput Screening? Assay Drug Dev Technol.2015;13:262-5.
33. Fennema E, Rivron N, Rouwkema J, van Blitterswijk C, De Boer J. Spheroid culture as a tool for creating 3D complex tissues. Trends Biotechnol. 2013;3:108–15.
34. Gaspar M, Coutinho P, Costa EC. Optimization of Liquid Overlay Technique to Formulate Heterogenic 3D Co-Cultures Models. Biotechnol Bioeng.2014;111:1672-85
35. Baek NH, Seo OW, Kim MS, Hulme J, An SSA. Monitoring the effects of doxorubicin on 3D-spheroid tumor cells in real-time. Onco Targets Ther. 2016;9:7207–18.
36. Yabbarov NG, Posypanova GA, Vorontsov EA, Popova ON, Severin ES. Targeted Delivery of Doxorubicin : Drug Delivery System Based on PAMAM Dendrimers. Biochemistry (Mosc).2013;78:884–94.
37. Tacar O, Sriamornsak P, Dass CR. Doxorubicin : an update on anticancer molecular action, toxicity and novel drug delivery systems. J Pharm Pharmacol.2013;65:157–70.
38. Shin H, Kwon H, Lee J, Gui X, Achek A, Kim J, Choi S. Doxorubicin-induced necrosis is mediated by poly- (ADP-ribose) polymerase 1 (PARP1) but is independent of p53. Nat Publ Gr. 2015;5:1–17.
39. Chen Yan, Wan Ying, Wang Yi, Zhang Haijun JZ. Anticancer efficacy enhancement and attenuation of side effects of doxorubicin with titanium dioxide nanoparticles. Int J Nanomedicine. 2011;6:2321–6.
40. Bhattacharyya Sanjib, Kudgus Rachel A., Bhattacharya Resham MP. Inorganic Nanoparticles in Cancer Therapy. Pharm Res. 2011;28:237–59.
41. Faraday M. Experimental relations of gold (and other metals) to light. R Soc Publ. 1857;147:145–81.
42. Mendes R, Fernandes AR, Baptista PV. Gold Nanoparticle Approach to the Selective Delivery of Gene Silencing in Cancer — The Case for Combined Delivery ? Genes. 2017;8:94-110.
43. Lim ZJ, Li JJ, Ng C, Yung LL, Bay B. Gold nanoparticles in cancer therapy. Nat Publ Gr. 2011;32:983–90.
44. Dreaden EC, Mackey MA, Huang X, Kangy B, El-sayed MA. Beating cancer in multiple ways using nanogold. Chem Soc Rev. 2011;40:3391–404.
45. D'Acunto M. Detection of intracellular gold nanoparticles: An overview. Materials (Basel). 2018;11:882-96.
46. Danhier F. To exploit the tumor microenvironment: since the EPR effect fails in the clinic, what is the future of nanomedicine? J Control Release. 2016;244:108–21.
47. Roma-rodrigues C, Raposo LR, Cabral R, Paradinha F, Baptista P V, Fernandes AR. Tumor Microenvironment Modulation via Gold Nanoparticles Targeting Malicious Exosomes : Implications for Cancer Diagnostics and Therapy. Int J Mol Sci. 2017;18:162-88.
48. Fernandes AR, Jesus J, Martins P, Figueiredo S, Rosa D, Martins LM, Corvo ML, Carvalheiro MC, Costa PM, Baptista PV. Multifunctional gold-nanoparticles: A nanovectorization tool for the targeted delivery of novel chemotherapeutic agents. J

Control Release. 2017;245:52–61.
49. Pedrosa P, Vinhas R, Fernandes AR, Baptista PV. Gold Nanotheranostics : Proof-of-Concept or Clinical Tool ? Nanomaterials. 2015;5:1853–79.
50. Conde J, Larguinho M, Cordeiro A, Raposo LR, Costa M, Santos S, Diniz M, Fernandes AR, Baptista PV. Gold-Nanobeacons for gene therapy : evaluation of genotoxicity , cell toxicity and proteome profiling analysis Gold-Nanobeacons for gene therapy : evaluation of genotoxicity , cell toxicity and proteome profiling analysis. Nanotoxicology. 2014;8:521–32.
51. Kettiger H, Schipanski A, Wick P. Engineered nanomaterial uptake and tissue distribution: from cell to organism. Int J Nanomedicine. 2013;8:3255–69.
52. Chithrani BD, Chan WCW. Elucidating the Mechanism of Cellular Uptake and Removal of Protein-Coated Gold Nanoparticles of Different Sizes and Shapes. Nano Lett. 2007;7:1542–50.
53. Cho EC, Xie J, Wurm PA, Xia Y. Understanding the Role of Surface Charges in Cellular Adsorption versus Internalization by Selectively Removing Gold Nanoparticles on the Cell Surface with a I 2 / KI Etchant. Nano Lett. 2009;9:1080–4.
54. Saha K, Kim ST, Yan B, Miranda OR, Alfonso FS, Shlosman D, Rotello VM. Surface Functionality of Nanoparticles Determines Cellular Uptake Mechanisms in Mammalian Cells. Small. 2013;9:300-5.
55. Chithrani BD, Ghazani AA, Chan WCW. Determining the Size and Shape Dependence of Gold Nanoparticle Uptake into Mammalian Cells. Nano Lett. 2006;6:662–8.
56. Mendes R, Pedrosa P, Lima JC, Fernandes AR, Baptista P V. Photothermal enhancement of chemotherapy in breast cancer by visible irradiation of Gold Nanoparticles. Nature. 2017;7:10872–81.
57. Pedrosa P, Mendes R, Cabral R, Martins LMDRS, Baptista PV, Fernandes AR. Combination of chemotherapy and Au-nanoparticle photothermy in the visible light to tackle doxorubicin resistance in cancer cells. Nature. 2018;8:11429–37.
58. Green DR, Llambi F. Cell Death Signaling. Cold Spring Harb Perspect Biol. 2015;7:6080–104.
59. Schmittgen TD, Livak KJ. Analyzing real-time PCR data by the comparative C T method. Nat Protoc. 2008;3:1101–8.
60. Zhang X, Chen J, Davis B, Kiechle F. Hoechst 33342 Induces Apoptosis in HL-60 Cells and inhibits topoisomerase I *in vivo*. Arch Pathol Lab Med. 1999;123:921:7.
61. Yao C, Hüttmann G. Important factors for cell-membrane permeabilization by gold nanoparticles activated by nanosecond-laser irradiation. Int J Nanomedicine. 2017;12:5659–72.
62. Heinemann D, Kalies S, Schomaker M, Ertmer W. Delivery of proteins to mammalian cells via gold nanoparticle mediated laser transfection. Nanotechnology. 2014;25:245101-10.
63. Heinemann D, Schomaker M, Kalies S, Schieck M, Carlson R, Escobar M, Ripken T, Meyer H, Heisterkamp A. Gold Nanoparticle Mediated Laser Transfection for Efficient siRNA Mediated Gene Knock Down. PLoS One. 2013;8:58604-13.
64. Shah S, Chandra A, Kaur A, Sabnis N, Lacko A, Fudala R, Gryczynski I. Fluorescence properties of doxorubicin in PBS buffer and PVA films. J Photochem Photobiol. 2017;170:65–9.
65. Mellor HR, Callaghan R. Accumulation and distribution of doxorubicin in tumour spheroids : the influence of acidity and expression of P-glycoprotein. Cancer Chemother Pharmacol. 2011;68:1179–90.
66. Balkwill F. TNF- α in promotion and progression of cancer. Cancer Metastasis Rev. 2006;25:409–16.
67. Wu Y, Zhou BP. TNF- a / NF- k B / Snail pathway in cancer cell migration and invasion. Br J Cancer. 2010;102:639–44.
68. Horssen R Van, Hagen TLM, Eggermont AMM. TNF- α in Cancer Treatment : Molecular Insights , Antitumor Effects , and Clinical Utility. Oncologist. 2006;11:397–408.

Appendixes

Appendix A

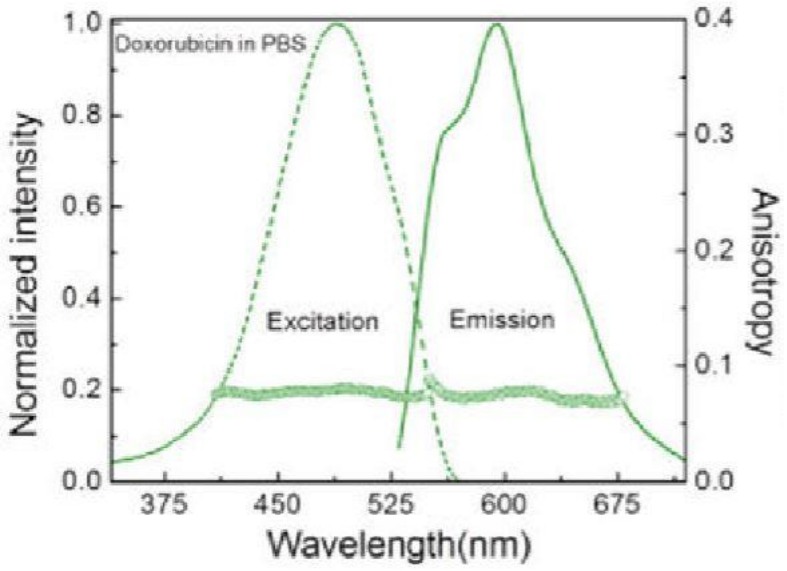

Appendix A Excitation and fluorescence spectra of Doxorubicin in PBS buffer. Also shown are excitation and emission anisotropies. The fluorescence excitation spectra were measured at 600 nm observation and fluorescence emission spectra were excited at 500 nm. Adapted from *Shah et al* (64).

Appendix B

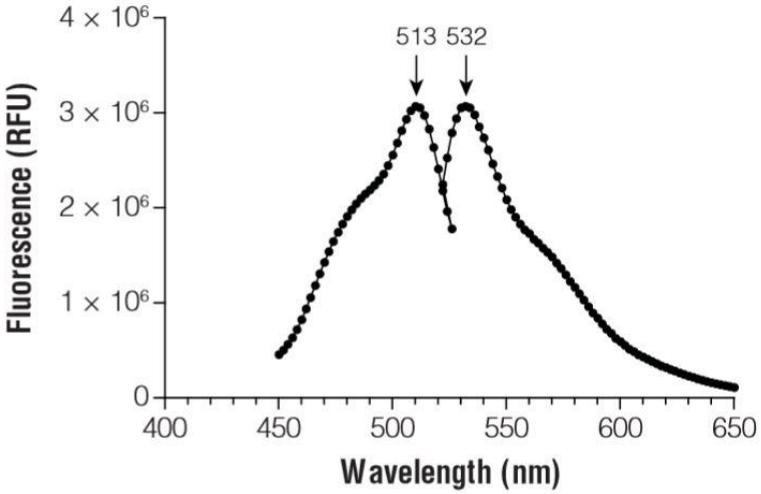

Appendix B Excitation and fluorescence spectra of CellTox™ Green Dye, showing peak excitation and emission. Adapted from CellTox™ Green Cytotoxicity Assay technical manual made available by manufacturing (Promega Corporation, Madison, Wisconsin, USA).

Appendix C

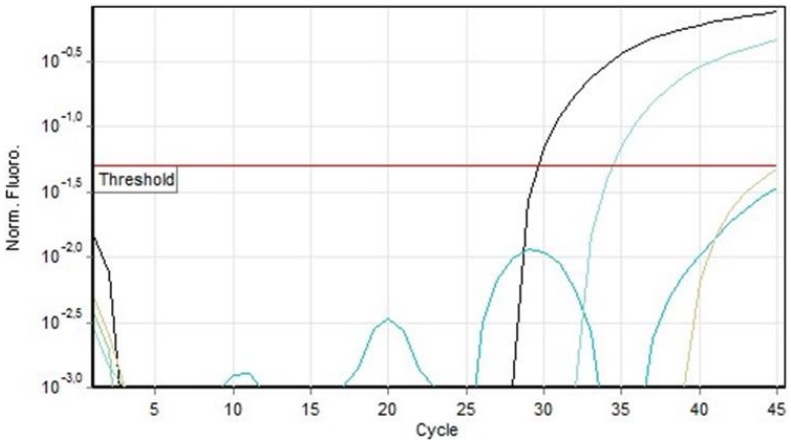

Colour	Name	Type	Ct
	TNFa HCT116 AuNP	Unknown	29,58
	TNFa Thp-1 (HCT116 AuNP)	Unknown	
	TNFa HCT116 DoxR AuNP	Unknown	
	TNFa Thp-1 (HCT116 DoxR AuNP)	Unknown	
	TNFa HCT116 I	Unknown	34,37

Appendix C Quantitation data obtained in the TNF-α expression assay with identified samples and respective C_T values.

Appendix D

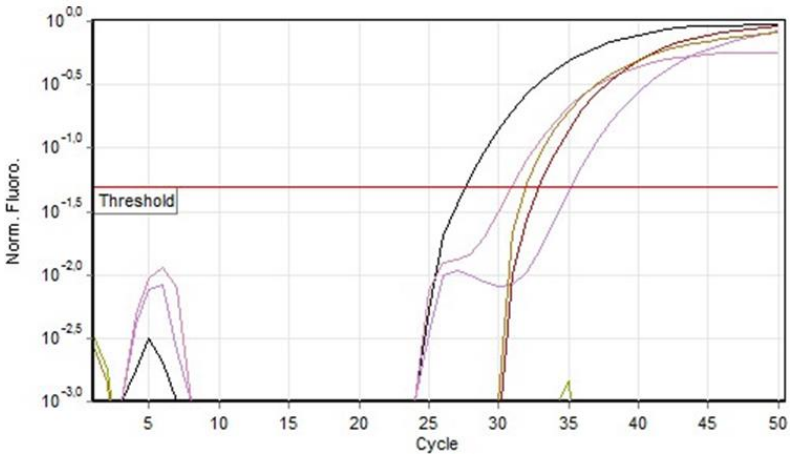

Colour	Name	Type	Ct
	TNFa HCT116 AuNP	Unknown	27,67
	TNFa HCT116 AuNP I	Unknown	
	TNFa Thp1 (HCT116 AuNP I)	Unknown	35,21
	TNFa HCT116 DoxR I	Unknown	30,94
	TNFa Thp1 (HCT116 DoxR I)	Unknown	32,88
	TNFa HCT116 DoxR AuNP I	Unknown	31,93
	TNFa Thp1 (HCT116 DoxR AuNP I)	Unknown	

Appendix D Quantitation data obtained in the TNF-α expression assay with identified samples and respective C_T values.